Predictive Analysis and Deep Learning of Functional MRI in Alzheimer's Disease

by

Michelle A. Karker

A dissertation submitted in partial fulfillment
of the requirements for the degree of
Doctor of Philosophy
(Biomedical Engineering)
in The University of Michigan
2022

Doctoral Committee:

Research Scientist Scott J. Peltier, Co-Chair
Professor Douglas C. Noll, Co-Chair
Professor Benjamin M. Hampstead
Associate Professor Zhongming Liu
Associate Professor Jenna Wiens

Michelle A. Karker

mkarker@umich.edu

ORCID iD: 0000-0001-7100-9385

ACKNOWLEDGEMENTS

I am very grateful for the support and guidance of my co-advisors, Dr. Scott Peltier and Dr. Douglas Noll. I appreciate their time and effort as they have provided many insights and presented many interesting research questions over the years. I especially admire their deep knowledge and intuition of functional MRI from acquisition and reconstruction to methodology and analysis. Thank you for your patience and help over the years.

Thank you to all of my committee members. I appreciate Dr. Benjamin Hampstead's knowledge and many contributions in the clinical aspects of Alzheimer's disease. Dr. Zhongming Liu's intuition in a wide range of topics and encouragement have been so helpful. Dr. Jenna Wiens has been instrumental in considering the broader context of this work.

Thank you to everyone in the fMRI Lab and others who helped out with data, code, and insightful discussions. I'd like to especially thank fellow students and postdocs of the fMRI Lab, both current and former: Shouchang, Tianrui, Melissa, Anish, Jonas, Dinank, Guanhua, Mariama, Amos, Sydney, and Kathleen. Thank you for the many fun moments and support when things weren't working. It has been a pleasure to work with you all.

Other students, Kuan, Jung-Hoon, and Yizhen, helped immensely in showing me how they have worked with variational autoencoder models. I appreciate their friendliness and intuition.

Many colleagues at the fMRI Lab and Michigan Alzheimer's Disease Research

Center made this work possible with their contributions via data acquisition, management and/or preprocessing, including Krisanne Litinas, Dr. Alexandru Iordan, Troy Tyszkowski, Jonathan Reader, and Stephen Schlaefflin.

I would like to thank Dr. Jon-Fredrik Nielsen and Dr. Jeffrey Fessler for helpful discussions and assistance on early work with pulse sequence programming with TOPPE and sparse sampling. I also appreciate Dr. Luis Hernandez-Garcia and Dr. Andy Jahn for providing their insights on preprocessing for arterial spin labeling data.

I greatly appreciate the help of Bennet Fauber with many aspects of the Great Lakes HPC usage that was critical for this work. I am grateful for IT help from Erik Keup and Charles Nicholas on countless occasions. Maria Steele has been so engaged, kind, and responsive in her role as graduate coordinator and I appreciate her support.

Thanks to Barb Hibbard and Theresa Russ, who are always a pleasure to chat with and have helped me with a variety of tasks over the years, from making arrangements for conferences to making sure there is a constant supply of tea in the student office. I am grateful for their kindness and help.

Also thanks to all of my wonderful loved ones, family, friends, and dogs whose support has kept me going these years. I am thankful for my friends, whose camaraderie has transformed my graduate school journey into a much more fun experience. My best friends Tyler and Benny are always there for me and I am so grateful to have them in my life. My parents and brother have been so supportive and they inspire me every day. I am extremely grateful for my family's love and kindness.

TABLE OF CONTENTS

LIST OF FIGURES

Figure

LIST OF TABLES

Table

LIST OF APPENDICES

Appendices

ABSTRACT

Alzheimer's disease (AD) and dementia pose a significant burden to individuals and public health. AD is expected to grow in prevalence in the coming decades due to the aging population. Brain atrophy is a major component of AD pathology and can occur before symptoms of cognitive impairment. However, pathological brain atrophy and symptoms of cognitive impairment may be a result of many years of disease impacts. Evidence supports the need for early detection of impacted neurocircuitry to foresee future progression to advanced stages of AD and develop treatments. This dissertation examines predictive modeling and deep learning methods to identify brain-behavior relationships and learn low-dimensional representations of brain activity from MR imaging data. The dissertation and methods are separated into four parts.

Part one of this work examines multivariate analysis approaches applied to functional connectivity from subjects with an early clinical phenotype of AD, mild cognitive impairment (MCI). A regression framework using partial least squares and feature selection demonstrated significant brain-behavior relationships with measures of cognition and memory. The results also confirm other findings that ecologically relevant task-based connectivity serves as a "stress-test" for memory-related deficits such as those observed in MCI. This approach elucidated brain regions that may be implicated in MCI and warrant future study (superior temporal gyrus, inferior parietal lobule, and superior frontal gyrus). Part two extends the multivariate analyses studied in part one to an additional brain imaging modality, arterial spin labeling (ASL). Cerebral blood flow (CBF) as measured by ASL demonstrated brain-behavior

relationships with composite measures of memory and learning in a cohort along the spectrum of AD, demonstrating that CBF data warrant further investigation as a predictor in this application.

Parts three and four utilize a variational autoencoder (VAE) model, a deep learning approach to encode latent representations that aim to disentangle sources of fMRI signal. A surface-based VAE trained on only healthy controls is shown to be generalizable to patients with MCI or dementia of the Alzheimer's type (DAT). The results maintained individual separation and high input/decoder output spatial reconstruction correlation of r=0.8 across all three groups. Part four extended the surface-based model used in part three to a volumetric fMRI approach. Similarly to the surface-based model, high reconstruction accuracy (NRMSE=0.68) and temporal correlation (r=0.8) between input and decoder output are demonstrated. This approach is more readily applicable to 3D fMRI data as compared to the surface-based model.

In summary, this work has proposed and developed multivariate and deep learning analysis techniques for brain imaging data in the context of AD with the ultimate goal of improving detection and intervention for early pathological changes in the brain.

CHAPTER I

Introduction

1.1 Background

1.1.1 Functional Magnetic Resonance Imaging

Functional magnetic resonance imaging (fMRI), consisting of a series of brain volume MRI acquisitions, has been increasingly studied for insights into brain function. It utilizes the blood-oxygen level dependent (BOLD) signal as an indirect measure of neural activity; this activity impacts local hemodynamics in the brain and thereby influences the MRI signal. There are two main modes of fMRI acquisition: task and resting-state. Task-based fMRI involves the subject completing a specific task while being scanned, whereas resting-state fMRI is collected in the absence of external task stimulus. Task-based fMRI is used to study aspects of the "working" brain. For example, one common task is a motor task, such as finger-tapping, that has been utilized for studying activation of the motor cortex.

Resting-state fMRI provides a measure of intrinsic brain activity, or brain activity when the subject is not performing any specific task. Research has demonstrated that the default-mode network (DMN) is involved in a baseline state of the brain (i.e, it is activated during wakeful rest including self-referential processing and internally directed cognition) [70, 142]. Resting-state acquisitions are beneficial in studies of

groups that may have difficulties completing a task (such as disease states impacting motor control, attention, or cognition).

1.1.2 Connectivity

There are several types of MRI-derived connectivity. The first is structural connectivity, typically referring to diffusion-based measures of physical connections in the brain. Diffusion-tensor imaging (DTI) measures the three-dimensional motion of water molecules [11, 12], which primarily diffuse along white matter tracts, thus providing an estimate for anatomical connections in the brain.

Functional connectivity is a measure of the temporal association between fMRI BOLD signals in different brain regions. This association is often computed using correlation (i.e., Pearson's correlation), and the regions that co-vary are thought to have indirect or direct communication. Biswal and colleagues demonstrated functional connectivity in humans using resting-state fMRI, where the motor cortex regions of interest were significantly more correlated with each other than with other areas of the brain [19]. This was replicated soon after with motor and language areas [73, 178]. Notably, connectivity can be studied with task and/or resting-state fMRI, with each method providing its own benefits.

There are several possible methods for obtaining brain regions among which to assess functional connectivity. Seed-based methods require a choice of seed, meaning a regional timecourse with which to correlate other regional timecourses. Often, this seed is either a particular voxel (seed-based), region-of-interest (ROI) (ROI-based), or parcel from using an predefined template ("parcellation") of segments of the brain. For each of these approaches, preprocessed fMRI timecourses averaged over each seed, ROI, or parcel would be extracted and correlated in a pairwise manner to yield a correlation matrix. There are also decomposition methods (i.e., principle components analysis (PCA)), and data-driven methods such as independent component analysis

(ICA).

Functional connectivity can be computed as a static measure, by using the entire time-series in the correlation, or as a dynamic measure by splitting the time-series into multiple states and deriving connectivity metrics for each state. This enables study of time-varying connectivity across the brain.

Structural and functional connectivity are useful for studies of brain networks. Both provide unique insights, either into the node connections in a network (structural), or the correlated activity between nodes (functional). Finally, a third type of connectivity, effective connectivity, aims to model the cause of activity in brain regions. Effective connectivity is assessed through structural equation modeling or dynamic causal modeling.

Over the years, interest in and publication of fMRI-based functional connectivity analyses has increased. Since fMRI-based functional connectivity is noninvasive and can provide a metric for brain activity that is in a lower dimensional space than volumetric fMRI, yet encodes both whole-brain and temporal information, it is an appealing data type for neurofunctional studies. Often, functional connectivity is analyzed by thresholding connectivity values and mapping them back onto the brain to visualize networks, or by graph theory analysis. More recent analysis approaches involve predictive modeling, which will be introduced in Chapter II.

1.1.3 Alzheimer's Disease: Pathology and Functional Changes

Alzheimer's disease (AD) is a progressive neurodegenerative disease, often leading to dementia that is characterized by loss of cognitive and memory function. Approximately 6 million Americans are afflicted with AD, and this number is projected to rise to 12.7 million by 2050 due to the increasingly aging population [143]. More recently, three distinct stages of Alzheimer's disease have been clinically adopted: a preclinical stage, an intermediate stage of mild cognitive impairment (MCI), and, in

the advanced stages, dementia of the Alzheimer's type (DAT) [89]. MCI diagnosis requires objective evidence of cognitive disturbances, despite relatively preserved everyday functioning. DAT is defined by severe cognitive and functional deficits that must be clinically diagnosed. Patients exhibiting the earliest clinical phenotype of DAT, MCI, have significant risk of progressing to dementia. However, the likelihood and speed of this conversion varies by individual. Furthermore, it is known that preclinical AD begins to effect the brain years before any diagnosis is made. Therefore, there is an increasing need for the study of brain changes in the early stages to aid future research of detection, prediction, and treatment methods.

Dementia is a nonspecific term for symptoms of cognitive and memory-related deficits. There are several diseases or disorders that can cause dementia; Alzheimer's disease is one of the most prevalent causes. Other causes include cerebrovascular disease, Lewy body disease, frontotemporal lobar degeneration, and Parkinson's disease, among others. However, there are often co-morbidities or mixed pathologies between other dementia causes [141], complicating the process of diagnosis, and highlighting the need for adaptable biomarkers that can differentiate or illuminate overlapping pathologies when applied transdiagnostically.

Alzheimer's disease pathology is defined by accumulation of amyloid-β and tau proteins, beginning years to decades before diagnosis (Figure 1.1). Tau presence is linked to cognitive decline. The hippocampus, in the temporal lobe, is one of the earliest brain structures affected in Alzheimer's disease. The Braak staging model outlines the progression of this accumulation from its beginnings in the inferior temporal and medial-frontal lobes until most areas of the brain are effected [21]. This accumulation is followed by nerve cell degeneration, or brain atrophy, that is visually recognized in brain images (such as MRI) by ventricle enlargement, widening of sulci, and thinning of gyri [169]. At this point, cognitive and behavioral changes begin to emerge as the disease progresses into advanced stages.

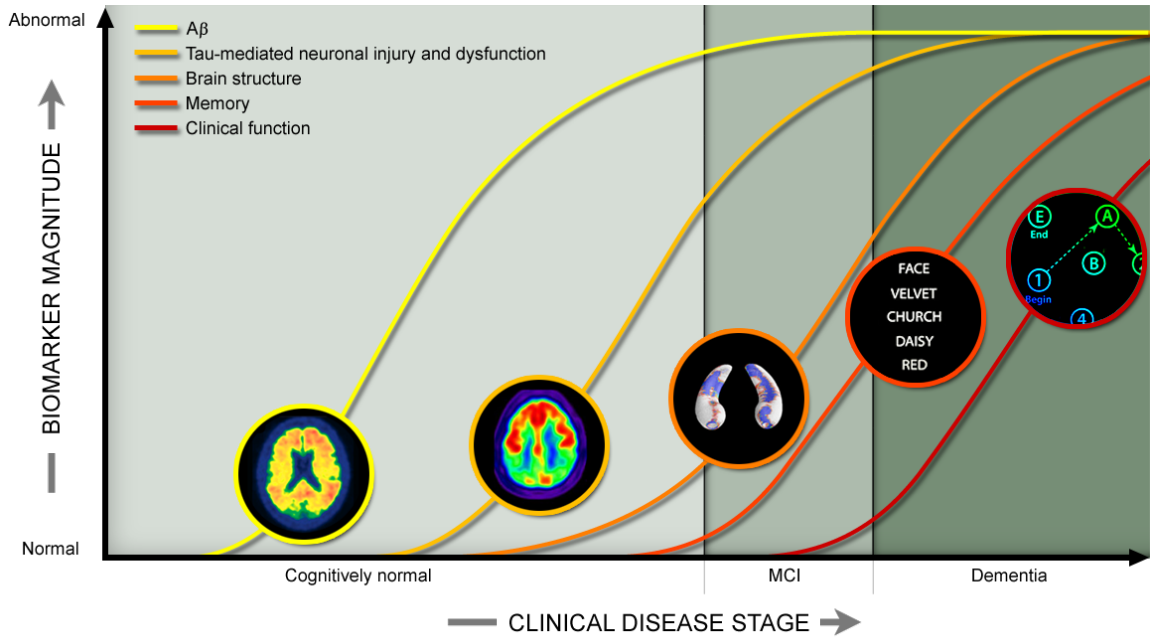

Figure 1.1: Schematic of Alzheimer's disease biomarkers and their progression over time. Figure from the Alzheimer's Disease Neuroimaging Initiative (https://adni.loni.usc.edu/study-design/#background-container).

Cognitive changes are expected to occur with normal, healthy aging, but increased levels of cognitive changes occur with MCI and DAT. Impairments in episodic memory, which entails conscious retrieval of detailed long-term memories of unique past events, is a notorious symptom of dementia, and often reflected in areas of the default-mode network [71]. However, episodic memory performance is also expected to decline with increasing age. Semantic memory, which involves general understanding of the world, is often stable over a lifetime, and may provide useful distinctions between aging and pathological cognitive decline [131]; however, it may not be consistently impaired across subjects along the continuum of Alzheimer's disease [84]. Other cognitive changes that may occur with age and/or dementia include degradation in spatial abilities, reasoning, and processing speed. There is increasing interest in studying the difference between normal aging and pathology because Alzheimer's disease causes changes in the brain many years before symptoms are detectable in the clinic, and

distinguishing early functional brain changes from normal aging can aid detection.

Biomarkers primarily focus on three components of Alzheimer's disease: amyloid-β, tau pathology, and neuronal injury [88, 90]. Biomarkers that are used to observe amyloid and tau in-vivo include measures of cerebrospinal fluid (CSF) and positron emission tomography (PET). The use of PET ligands, such as fluorodeoxyglucose (FDG), has been adopted as an AD biomarker. FDG can assess the metabolism of glucose in the brain, which is commonly abnormal in AD [127]. FDG-PET often demonstrates hypometabolism in areas with brain atrophy [36, 128]. FDG and other PET ligands are also used to investigate tau pathology in living individuals. Neuronal injury is assessed with structural MRI, FDG-PET hypometabolism, or CSF total tau. AD-related brain atrophy has been observed via structural MRI up to a decade before symptoms and diagnosis occur [165]. The presence of Alzheimer's disease is presumed if differential diagnosis of these biomarkers and clinical evaluations of cognition indicate AD pathology. This can be confirmed post-mortem through neuropathology studies using Pittsburgh Compound-B (PiB) that binds to amyloid-β and reveals its deposits in the brain [85]. There is clinical need for new biomarkers to assess different aspects of Alzheimer's disease and detect earlier changes in the brain.

There is also growing knowledge of the genetic component of Alzheimer's disease. The first discovery in this realm was the risk of developing Alzheimer's disease with the presence of the apolipoprotein E (APOE) gene type $\epsilon 4$ allele [135]. Additional studies have found other genetic loci associated with Alzheimer's disease [109, 158], and significant correlations between genetic risk scores and future AD risk as well as progression from MCI to DAT [16].

Growing evidence supports the consensus that interventions are needed at the earliest stages of Alzheimer's disease. This motivates the need for sophisticated data acquisition and analysis techniques that can disentangle early changes in the brain, leading to biomarker discovery and improved detection and prediction of dis-

ease states. Studies can leverage imaging modalities and cognitive assessments and other tools to study structural and functional changes inherent to Alzheimer's disease. Functional MRI is a promising modality due to its noninvasive nature and capacity for multimodal integration (i.e., combination with structural MRI, DTI, etc.).

1.1.4 Functional MRI and Alzheimer's Disease

Functional MRI is increasingly studied as a potential biomarker for Alzheimer's disease, with an emphasis on connectivity and network analysis. Both resting-state and task-based fMRI have been investigated for this purpose, each providing distinct insights into changes in brain activations in Alzheimer's disease. Differences in fMRI activations in this context may be related to altered neural activity that results in AD-related impairments (e.g., deficits in memory) or neurovascular dysfunction causing altered neurovascular coupling or other causes. In addition, compensatory-related increases in fMRI activations during early stages of Alzheimer's disease pathology are widely acknowledged [40, 67].

Decreases in regional coherence in the posterior cingulate cortex/precuneus have been observed in subjects with DAT compared to controls in resting-state fMRI [81]. There is evidence that task-based stimuli perturb network connectivity, resulting in improved detection of disease-relevant changes. Certain types of task-based fMRI, such as memory-related tasks, can serve as stress tests to emphasize brain regions or networks of interest implicated in afflictions of memory. For example, deficits in explicit visual memory are observed in subjects with DAT during viewing of scenes [64]. Face-name association task-based fMRI studies indicate that medial temporal lobe (including hippocampal) activations are diminished in subjects with DAT [161]. The object-location association task was developed for use in testing memory impairment in MCI and illuminated the changes in encoding mechanisms in disease states [75].

1.1.5 Functional Connectivity and Alzheimer's Disease

Resting-state fMRI functional connectivity has been utilized in numerous studies of Alzheimer's disease. The hippocampus is implicated in early stages of Alzheimer's disease, and has been demonstrated to have disrupted resting-state functional connectivity in subjects with amnestic MCI [9].

In resting-state, disrupted functional connectivity in the DMN is another common observation in cohorts along the continuum of Alzheimer's disease. Alterations of default mode network connectivity observed in MCI and DAT patients versus healthy controls [2, 18, 148, 173]. Insufficient memory function is often reflected by impaired default mode network functional connectivity [35, 125] and subjects with DAT demonstrate reduced connectivity in the posterior DMN as compared to healthy older adults [71].

Functional connectivity demonstrates significant between-group differences in MCI compared to healthy controls, signifying that global degradation of brain networks are detectable in early stages (MCI) [120]. In amnestic MCI, initial increases in posterior cingulate cortex (PCC) connectivity have been observed, followed by decreased PCC activity and increased connectivity in the frontal network at a longitudinal follow-up [8]. This may reflect a potentially compensatory-related pattern of initial hyper-connectivity in early disease stages followed by hypo-connectivity as the pathology advances. Furthermore, this progression often follows the trail of pathological changes observed by Braak et al. [21], starting in the medial temporal lobe, spreading through areas of the DMN (including the PCC) and then spreading to frontal regions of the brain in later stages.

Characterization of neural mechanisms involved in early changes in the brain with Alzheimer's disease pathology is crucial for prediction of conversion to advanced disease stages and studies of therapeutic interventions. The evidence that functional connectivity is a sensitive metric for memory and other AD-related changes in the

brain, along with evidence of functional connectivity increases in initial disease states, indicates that it may aid early detection and could provide further utility, such as in studies of prediction.

1.2 Motivation

Neuroimaging has become an important tool in the clinical evaluation of individuals with suspected neurodegenerative disease, such as AD. Brain scans using structural MRI have the power to elucidate the presence and progression of neurodegeneration. Individuals with MCI and DAT often display the AD hallmark progressive atrophy (especially in one of the key AD regions, the medial temporal lobes) [169]. However, once macroscale brain atrophy is observed, the disease has already been affecting the brain for years to decades. Early detection is key. A large area of interest in current research to improve early detection of AD is focused on characterizing the early functional changes in the brain with AD; one approach is with functional MRI, as it provides a proxy for neural activity.

Functional MRI measures are increasingly studied as potential biomarkers for Alzheimer's disease, with an emphasis on connectivity and network analysis. As previously discussed, compensatory-related increases in fMRI activations during early stages of Alzheimer's disease pathology are widely acknowledged. During advanced stages of AD, general reductions in brain activations are often observed. Differences in fMRI activations in this context may be related to altered neural activity that results in AD-related impairments (such as deficits in memory) or neurovascular dysfunction causing altered neurovascular coupling or potentially other causes. The takeaway is that fMRI can provide a indirect measure of neuronal functioning and may be useful in identifying patients at risk of developing AD even before macroscale atrophy develops.

Overall, detection and interventions are needed at the earliest stages of Alzheimer's disease. Functional MRI is a promising modality due to its noninvasive nature and

capacity for multimodal integration. So fMRI may be able to illuminate neural mechanisms involved in early changes, hopefully leading to improved early detection.

This dissertation focuses on evaluating the merits of several neuroimaging data types and analysis approaches for studying early changes in brain networks in AD. The first aim is to evaluate whether task-based functional connectivity focused on memory can "stress" the relevant networks and better capture relationships between functional connections and memory performance compared to resting-state functional connectivity. Next, this work considers the extension of previous predictive modeling frameworks to arterial spin labeling measures of cerebral blood flow. The third aim is to evaluate whether a pre-trained (on healthy subjects) representation learning model is readily generalizable to rs-fMRI data from patients across the spectrum of Alzheimer's disease. Lastly, this work aims to evaluate how the cortical surface-based VAE findings extend to a volumetric version.

1.3 Contributions

The main contributions described in this dissertation are discussed in four chapters that are outlined in this section.

In chapter II, we examined multivariate analysis of mild cognitive impairment. We developed a partial least squares (PLS) regression and feature selection pipeline for functional connectivity. Our results demonstrated improved brain-behavior prediction with task-based data.

In chapter III, we designed and implemented a novel application of brain-behavior prediction to arterial spin labeling (ASL) data. Our results included significant relationships between ASL measures and both learning and memory metrics.

In chapter IV, we implemented a novel extension of a cortical surface-based representation learning model to rsfMRI in the aging population (typical, MCI, DAT). The surface-based model trained on healthy controls maintained individual separa-

tion and high reconstruction performance when applied to subjects with MCI and DAT.

In chapter V, we developed a volumetric representation learning model to study rsfMRI. We demonstrated that spatial and temporal patterns of rsfMRI were successfully encoded and decoded and that the resulting generative model aligned well with known resting-state networks.

Chapter VI summarizes the work described in earlier chapters and discusses its possible future extensions.

Besides these chapters, Appendix A includes additional figures from the CPM methodology in Chapter II and Appendix B provides a how-to guide for those getting started with high performance computing as it pertains to fMRI data preprocessing.

CHAPTER II

Multivariate Analysis of Mild Cognitive Impairment Using Connectome Predictive Modeling and Partial Least Squares Regression

2.1 Introduction

Patterns of functional connectivity from functional magnetic resonance imaging (fMRI) indicate temporally correlated brain activations [19]. These patterns can also reflect physiological changes in the brain [134]. Recent studies have focused on identifying neurological and psychiatric diseases using predictive models based on an individual's functional connectivity footprint [108, 151]. There is also evidence that functional connectivity measured during a task that is relevant to a neuropsychological state can provide additional and/or complementary information; such findings have been reported for studies of attention, intelligence, language and working memory [68, 93, 180].

An individual's connectivity footprint holds promise as a potential biomarker for dementia of the Alzheimer's type (DAT). However, Alzheimer's disease often effects the brain many years before symptoms are clinically diagnosed, beginning with the accumulation of amyloid and tau proteins followed by brain atrophy. After this stage, patients develop memory deficits and enter the continuum of the mild cognitive im-

pairment (MCI) clinical phenotype. This makes early detection of any brain changes paramount for patient diagnosis and therapeutic intervention. MCI is typified by the presence of both subjective and objective cognitive (herein to focus on memory) deficits but relatively preserved everyday functioning [3]. MCI due to Alzheimer's disease indicates significant risk of progressing to dementia, a condition that is expected to significantly increase in prevalence in the next few decades. As such, the diagnostic category of MCI provides a clinically relevant testbed for predictive modeling since this phenotype encompasses those who range from nearly cognitively intact to those nearly indistinguishable from dementia. Thus, focusing on only those with MCI may ultimately help identify those most likely to convert to dementia in the near future, thereby enabling earlier identification and intervention. To the authors' knowledge, there are no studies examining predictive modeling in a cohort with MCI using pathology-relevant functional connectivity footprints.

Connectome predictive modeling (CPM) is one approach to relate functional brain network strength to a specific metric of behavior or trait. The protocol for CPM includes feature selection of functional connectivity data and linear regression [47, 159], Elastic Net regression [41], or another approach to predict the response of interest. CPM has been applied in several studies of connectivity data and successfully predicted attention performance [151], individual identification and fluid intelligence [47, 68]. Other work has utilized CPM to predict working memory performance from various age groups [183]. Additionally, functional connectivity from resting-state fMRI was found to successfully predict measures of overall cognitive impairment using functional connectivity from subjects spanning the AD spectrum [119]. An extension of CPM also determined that combining predictor information from two or more task functional connectivity measurements provides complementary information about individual differences [54].

Another existing multivariate analysis technique, partial least squares (PLS) re-

gression, maximizes covariance between data and labels in its modeling approach and is currently used in various aspects of neuroimaging [107]. Since PLS regression utilizes both data and labels to estimate the model, it is an attractive approach for representing the interplay between cognitive deficits and functional connectivity across the continuum of MCI. PLS regression has shown promise in similar milieu for investigating the brain-behavior relationship. For example, PLS regression has been successfully used to predict reading comprehension, episodic memory, and attention from functional connectivity [93, 124, 180]. PLS regression has been applied to a cohort with MCI using resting-state functional connectivity [124]. However, to the authors' knowledge, it has not yet been applied to a cohort with MCI using MCI-relevant fMRI task data. There are many underlying factors contributing to a diagnosis of MCI and a case-control study is likely to overlook the heterogeneity of relationships in this population by enlarging the study scope to multiple entire phenotypes. Thus, it is important to examine the relationship between ecologically-relevant neuroimaging-derived measures and cognitive performance within the MCI group.

Other analytical methods suited to brain-behavior relationship modeling include principal components regression (PCR), brain basis set (BBS) [162, 163], and other combinations of principal components analysis and regression [53], among others. However, neither of them provides the implicit modeling of response variables as in PLS regression. Therefore, this study focuses on an in-depth comparison of CPM and PLS regression.

As evidenced through CPM and PLS regression, multiple analytical methods have been applied to patterns of functional connectivity and their relationships with cognitive performance. However, there are few studies comparing their performance against one another. Different methodologies have the potential to provide complementary information or better pinpoint relationships of interest. In this work, we aim to fit CPM and modified PLS regression (termed PLS-BETA) models to the

brain-behavior relationship in subjects with MCI and investigate the merit of these different modeling approaches. We demonstrate that PLS-BETA is a viable technique for modeling the brain-behavior relationship and offers an improvement over other techniques in predicting individual differences, perhaps due to its maximizing of the covariance of predictor and response variables. As stated above, prior evidence demonstrates that task-based functional connectivity relevant to a condition can emphasize brain-behavior relationships [68, 93, 180]. Therefore, a secondary aim was to evaluate whether task-based functional connectivity focused on memory can "stress" the relevant networks and better capture relationships between functional connections and memory performance compared to resting-state functional connectivity. We also investigated whether a combination of the two task-based connectivity predictors may add complementary information about the effects of memory impairment an individual is experiencing. As an exploratory aim, we evaluated the significant nodes resulting from CPM and PLS-BETA in relation to known evidence of dysfunction in MCI.

2.2 Methods

2.2.1 Data

fMRI data were acquired using a Nova Medical 32-channel head coil on a 3T MR750 GE scanner using multiband EPI (MB factor=3). Task and resting-state fMRI data were acquired during a single scanning session for 84 older adults with MCI (age=73.0±7.1, 47M/37F). All participants provided written informed consent and study activities were approved by VA Ann Arbor. Acquisition parameters for the task-based scans were repetition time (TR) 1200 ms, echo time (TE) 30 ms, 318 timepoints, flip angle 70°, field of view (FOV) 220 mm, 51 axial slices, and 2.5 mm isotropic voxels. Resting-state scans used the following parameters: TR: 900 ms, TE:

30 ms, 506 timepoints, and 3.25 x 3.25 x 3 mm voxels. Resting-state scans were completed eyes-open with a fixation cross. SPGR parameters were as follows: TR: 12.3 ms, TE: 5.2 ms, flip angle 15°, FOV 25.6 cm, 1 mm^3 voxels, reconstruction matrix 256 x 256, and 156 slices. Each session included two runs of each type of fMRI scan. Initially, the first runs of these scans were analyzed, and later, the second runs were analyzed to replicate the same original methods.

The face-name and object-location association fMRI tasks were performed as published [74–76]. Face-name and object-location association tasks used a mixed event-related block design consisting of six active blocks and seven rest blocks. Active blocks contained three novel and three repeated stimuli, where participants were instructed to push a button when a new stimulus occurred. After the scan, participants completed a memory test using the same stimuli. For face-name runs, participants were shown faces and asked to recall the name in the cued recall phase, and then asked to select the correct name from three options in the recognition phase. For object-location runs, participants were shown an object followed by a blank screen and were instructed to touch the location of the object on a touch screen monitor in the free recall phase, and then shown the object and then its corresponding room without the object and were instructed to touch the correct position on the touch screen in the cued recall phase. Lastly, there was a recognition phase where participants were instructed to select the location of the object from three location choices [74]. An example of this paradigm is shown in Figure 2.1. For the purposes of this study, we focus on the encoding-related BOLD fMRI data; the face-name and object-location memory test performances will be reported separately.

2.2.2 Neuropsychological Measures

We selected measures of cognitive functioning to evaluate the true predictive ability of PLS-BETA and CPM. These measures included the total score on the

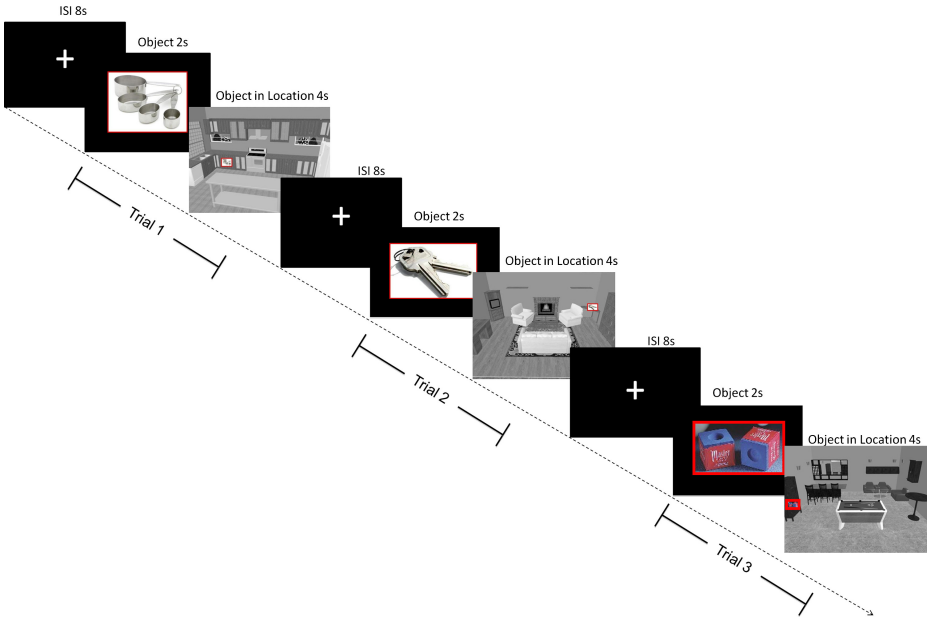

Figure 2.1: The object location association paradigm, reprinted from [75] by permission from Elsevier: Neuropsychologia, "Where did I put that? Patients with amnestic mild cognitive impairment demonstrate widespread reductions in activity during the encoding of ecologically relevant object-location associations," Benjamin M. Hampstead, et al. © 2011.

Montreal Cognitive Assessment (MoCA) [130] and both the Delayed Memory Index ($\text{RBANS}_{\text{delayed}}$) and Total Score ($\text{RBANS}_{\text{total}}$) on the Repeatable Battery for the Assessment of Neuropsychological Status (RBANS) [145]. RBANS, particularly the delayed memory index, has been shown to be associated with AD pathology [164]. The RBANS metrics used in this work were summed raw index scores since age was corrected in the analytic model. Subject demographics and neuropsychological cognitive measure means and standard deviations are reported in Table 2.1. Note that raw scores are used for the RBANS and MoCA to avoid redundant correction since age was included in the primary analytic model.

2.2.3 Preprocessing

The following preprocessing steps were applied to the imaging data: cardiac and respiratory noise correction using RETROICOR [63], slice timing correction using

Table 2.1: Demographic and performance means (standard deviation) for subjects.

	aMCI (n=84, 47M/37F)
Age	73.0 (7.1)
RBANS$_{\text{delayed}}$	28.0 (9.9)
RBANS$_{\text{total}}$	165.6 (22.0)
MoCA	21.5 (3.2)

Statistical Parametric Mapping software version 12 (SPM12; Wellcome Department of Human Neuroimaging, London, England), combined distortion correction (using a field map generated in FSL MCFLIRT [91], motion registration in SPM12), normalization into MNI space (sampled at 3 mm resolution) (Computational Anatomy Toolbox for SPM, CAT12; http://www.neuro.uni-jena.de/cat/), and smoothing at 5 mm FWHM. The CONN toolbox then applied detrending (quadratic), despiking (loess regression smoothing, piecewise cubic interpolation), nuisance regression (motion parameters and first derivative and quadratic, CSF and white components (top 5 components identified by PCA in CSF/white matter masks)), and bandpass filtering: 0.01-0.1 Hz.

Functional data were parcellated into 264 regions of interest (ROIs) using the Power atlas [137], with 8 additional ROIs (Table 2.2): two in the left and right amygdala and six from the left and right hippocampus for a total of 272 ROIs. Average time courses in all ROIs were correlated with all other ROI timecourses (Pearson product-moment correlation). Z-scores were computed from these correlation matrices via Fisher transformation.

2.2.4 Modeling

PLS-BETA and CPM modeling were applied to the first runs of two task-based (face-name and object-location association) and resting-state connectivity data and used to predict each cognitive measure: MoCA score, RBANS$_{\text{delayed}}$ and RBANS$_{\text{total}}$.

Table 2.2: MNI coordinates and labels for pathology-specific ROIs used in addition to the Power atlas.

ROI	MNI (x, y, z)	Label
1	(-24, -4, -20)	Left Amygdala
2	(24, -2, -20)	Right Amygdala
3	(28, -12, -20)	Right Hippocampus
4	(30, -24, -12)	Right Hippocampus
5	(30, -39, -3)	Right Hippocampus
6	(-29, -12, -22)	Left Hippocampus
7	(-30, -24, -12)	Left Hippocampus
8	(-29, -38, -4)	Left Hippocampus

PLS-BETA was implemented with the MATLAB 2020b function plsregress, which implements the SIMPLS algorithm, using leave-one-out cross validation. PLS regression has many options for feature selection; here, the highest magnitude PLS regression coefficients are used to limit overfitting [123]. For each subset of leave-one-out training data, age was regressed from both functional connectivity and cognitive measures. The resulting predictors and responses were used to obtain PLS regression weights and the top 300 in magnitude were used as a feature mask to form a new PLS model on the training data (Figure 2.2). This feature mask was also used to test the model on the left-out subject. To evaluate significance, permutation testing was performed with 1000 iterations. Each iteration, randomly shuffled labels were inputted to the entire cross-validated modeling process to generate a null distribution of R values against which to compare the actual R value.

CPM was implemented using the protocol in [159], shown in Figure 2.3, with a threshold of 0.01 for feature selection of significantly correlated edges. Significant edges were summed into the overall "brain score." This process was done for positive and negative correlations separately. Then, a linear model was fit under the assumption of a linear relationship between brain score and behavioral score. A leave-one-out framework was used, with the "left-out" subject used to test the fit linear model. Age was regressed within the cross-validation scheme from both connectivity and measures

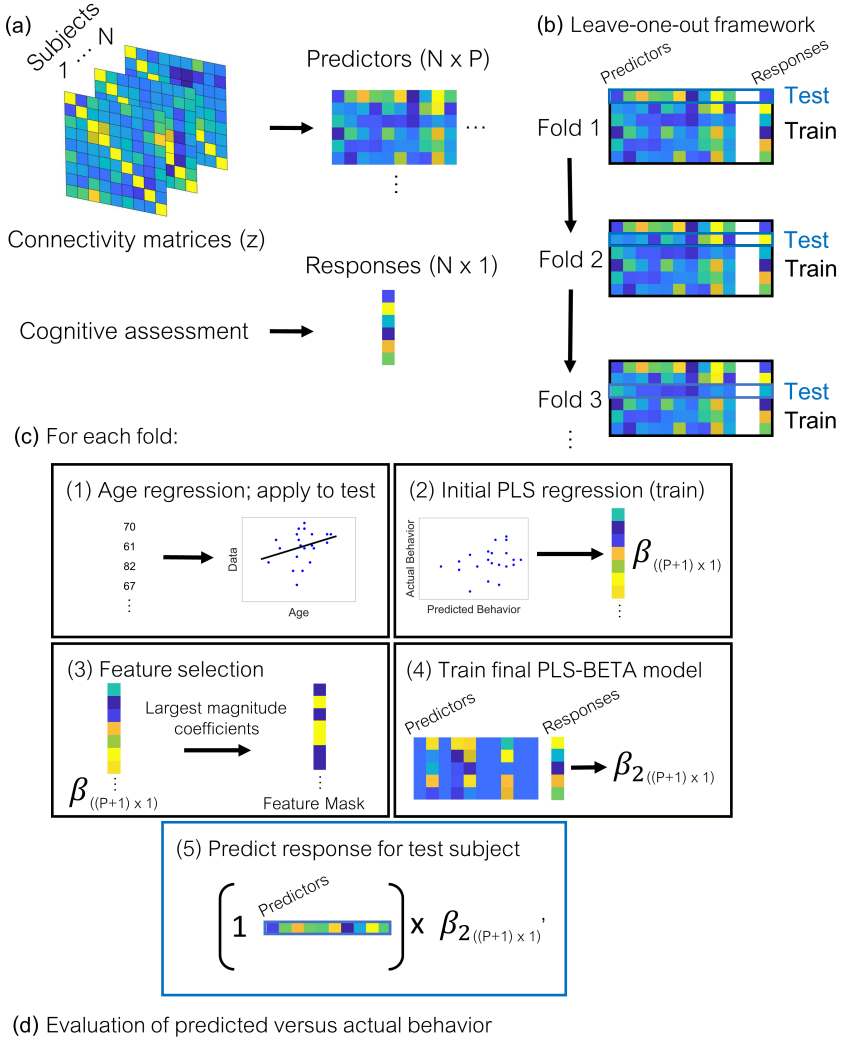

Figure 2.2: Schematic of PLS-BETA modeling approach. (a) First, connectivity matrices are reshaped into an N x P predictor matrix, where P is the total number of connectivity edges in the upper triangular region of connectivity matrices for each subject. (b) The predictor matrix and cognitive measure response variables are split into train and test groups following a leave-one-out cross-validation framework. (c) For each fold, the following procedure is followed: (1) Age is regressed from both predictors and responses in the train group and the resulting age regression coefficients are applied to the left-out test subject. (2) An initial PLS regression is performed with the training group only. (3) From the initial PLS regression, the beta coefficients are used as feature selection criterion by selecting the top 300 magnitude beta coefficients. (4-5) This feature selection is used to form a final PLS-BETA model on the train group and the resultant model is applied to the test subject. (d) After all folds have been completed, the predicted behavior is evaluated.

as for PLS-BETA. Permutation testing was performed with 1000 iterations to evaluate significance.

We also evaluated combinations of task and rest connectivity data by concatenating the types of connectivity data into the predictor variable feature space with the same response variables.

2.2.5 Visualization

Significant model connections were visualized with the Yale BioImage Suite Connectivity Viewer (bioimagesuiteweb.github.io/webapp/), to evaluate lobule connections across hemispheres, and to display important nodes defined by degree, the number of edges attached to a particular node [152]. For demonstration purposes, nodes with the top 5 highest degrees were selected to visualize significant connections for each model. The MNI coordinates for the top five highest degree nodes were used to obtain labels in WFU PickAtlas [122] from the Talairach Daemon [110] and the automated anatomical labeling (AAL) atlas [167].

2.3 Results

Both PLS-BETA and CPM yielded significant brain-behavior relationships using task data for the measures $\text{RBANS}_{\text{total}}$ and $\text{RBANS}_{\text{delayed}}$ (summarized in Table 2.3). PLS-BETA predicted cognitive performance for both task fMRI datasets (Figures 2.4-2.6). Figures 2.4-2.6 show line plots of actual versus predicted scores, circle plots of node connectedness, and glass brain plots to visualize high degree node locations. For object-location task data, a significant relationship was identified for $\text{RBANS}_{\text{total}}$ ($R=0.44$, $p\leq0.001$). For face-name task data, significant relationships were identified for $\text{RBANS}_{\text{total}}$ ($R=0.55$, $p\leq0.001$) and $\text{RBANS}_{\text{delayed}}$ ($R=0.37$, $p\leq0.05$). PLS-BETA also depicted a significant relationship with $\text{RBANS}_{\text{total}}$ ($R=0.43$, $p\leq0.001$) for the combination of face-name and object-location task data (Figure 2.7). CPM resulted in

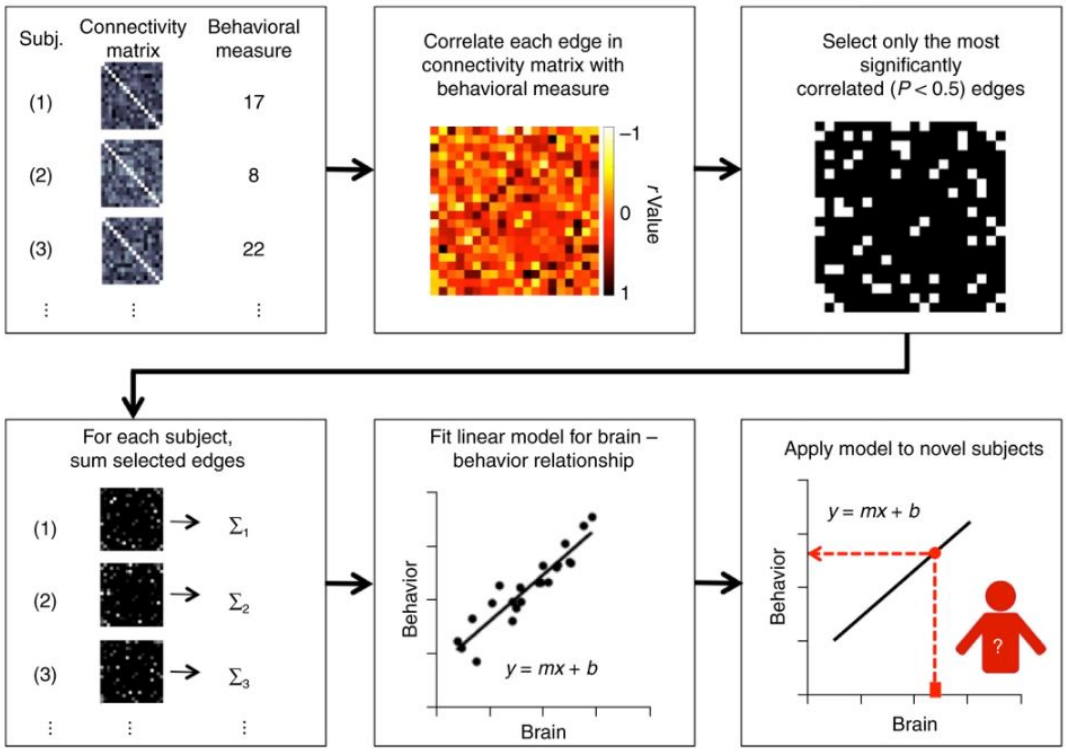

Figure 2.3: Schematic of the CPM method [159], reprinted by permission from Springer Nature: Springer Nature, Nature Protocols, "Using connectome-based predictive modeling to predict individual behavior from brain connectivity," Xilin Shen, et al. © 2017. Following a leave-one-out cross validation framework, connectivity data and behavioral measures are correlated across the training set subjects. The resulting correlations are thresholded at a given level to determine significance ($p<0.01$). Next, the connectivity values at significant edges are summed separately for positive and negative correlations. This generates a brain score that is used to fit a linear model with the behavioral measures. Finally, this model is applied to the held-out subject to predict a behavioral score from their connectivity data. After all folds are complete, the performance is evaluated via correlation of actual and predicted behavioral measures.

Table 2.3: PLS-BETA and CPM Results Comparison.

	CPM					
	Face-name		**Object-location**		**Resting-state**	
Behavioral Data	$\mathbf{R_{pos}}$	$\mathbf{R_{neg}}$	$\mathbf{R_{pos}}$	$\mathbf{R_{neg}}$	$\mathbf{R_{pos}}$	$\mathbf{R_{neg}}$
$\mathbf{RBANS_{delayed}}$	0.18	0.04	-0.08	0.03	0.13	0.10
$\mathbf{RBANS_{total}}$	0.09	**0.46****	**0.33***	**0.28***	0.17	0.04
MoCA	-0.20	-0.18	0.03	-0.24	0.07	-0.22

	PLS-BETA		
	Face-name	**Object-location**	**Resting-state**
Behavioral Data	**R**	**R**	**R**
$\mathbf{RBANS_{delayed}}$	**0.37***	0.11	0.13
$\mathbf{RBANS_{total}}$	**0.55****	**0.44****	0.09
MoCA	0.04	0.22	0.03

* $p \leq 0.05$, ** $p \leq 0.001$, obtained from 1,000 permutations.

significant relationships for $\text{RBANS}_{\text{total}}$ with both types of task fMRI data: face-name data (R=0.46, p≤0.001 for CPM negative edges) and object-location data (R=0.33, p≤0.05 for CPM positive edges; R=0.28, p≤0.05 for CPM negative edges). Resting-state data did not yield significant positive relationships with these cognitive metrics using either PLS-BETA or CPM methods.

High degree nodes and corresponding region labels are summarized in Tables 2.4 and 2.5, for PLS-BETA and CPM, respectively. For PLS-BETA, these nodes occurred in the superior frontal gyrus, superior temporal gyrus, precuneus, and inferior parietal lobule. For CPM, these nodes occurred in the precuneus, middle frontal gyrus, inferior parietal lobule, superior temporal gyrus, and precentral gyrus. Relevance of high degree node locations will be considered in the following section.

These results were replicated with functional connectivity data from the second run of each fMRI scan. The replication results are shown in Table 2.6. PLS-BETA resulted in significant relationships between face-name task fMRI and $\text{RBANS}_{\text{delayed}}$ (R=0.30, p≤0.05) and between object-location task fMRI and $\text{RBANS}_{\text{total}}$ (R=0.30, p≤0.05). For CPM, significant relationships were identified for face-name task fMRI with both $\text{RBANS}_{\text{delayed}}$ (R=0.32, p≤0.05 for CPM positive edges) and $\text{RBANS}_{\text{total}}$

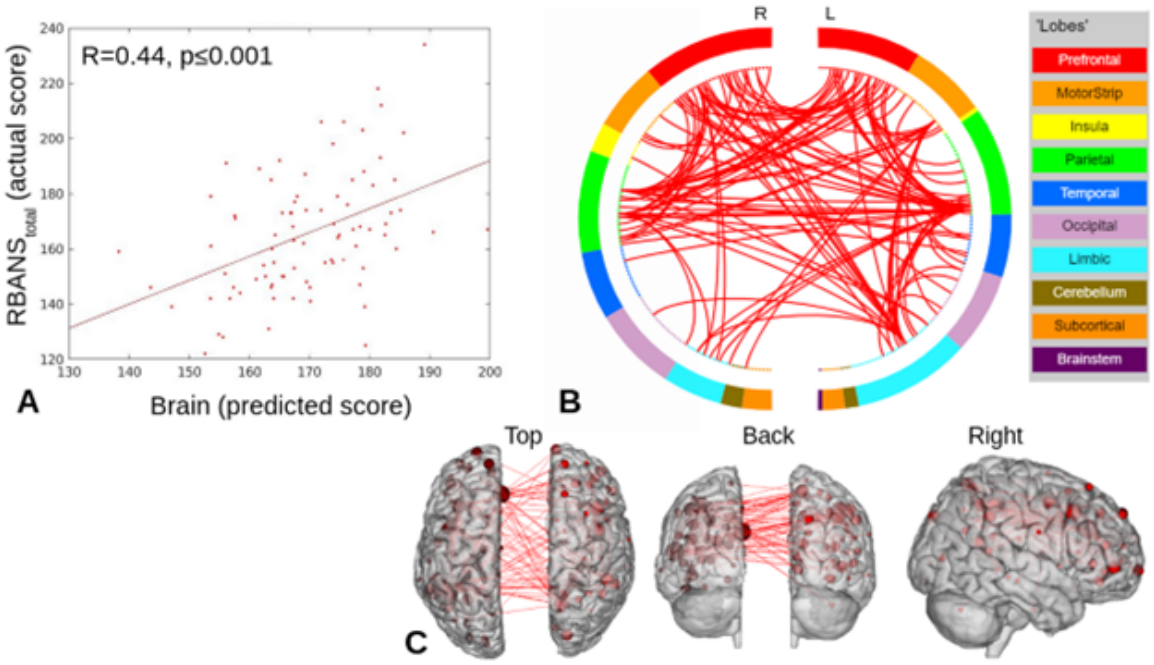

Figure 2.4: RBANS$_{\text{total}}$ PLS-BETA results for object-location task data. A) Plot of predicted versus actual RBANS$_{\text{total}}$ values. B) Circle plot of significant connections between brain areas (using node degree threshold of 14). C) Glass brain plot of significant nodes and connections.

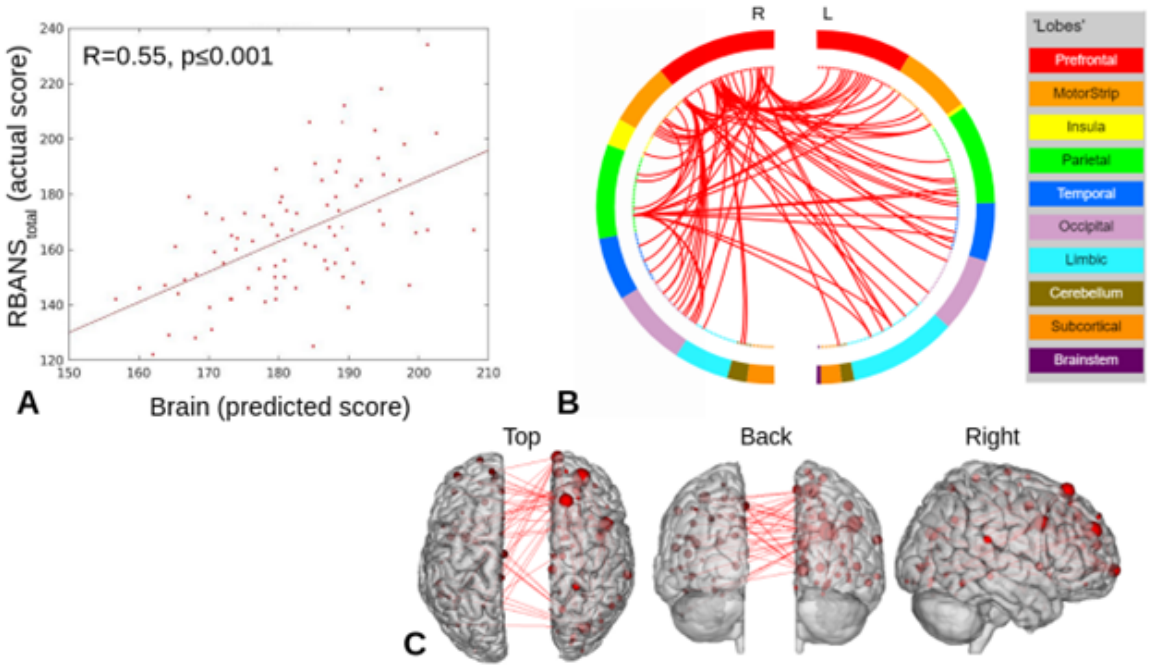

Figure 2.5: RBANS$_{\text{total}}$ PLS-BETA results for face-name task data. A) Plot of predicted versus actual RBANS$_{\text{total}}$ values. B) Circle plot of significant connections between brain areas (using node degree threshold of 15). C) Glass brain plot of significant nodes and connections.

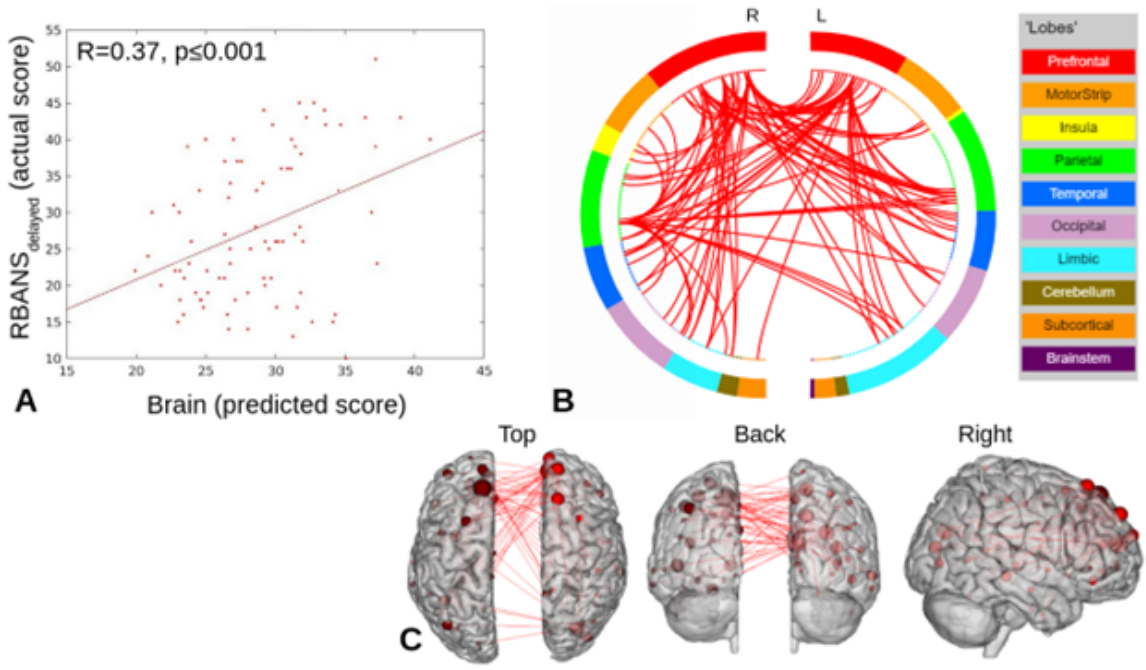

Figure 2.6: $\text{RBANS}_{\text{delayed}}$ PLS-BETA results for face-name task data. A) Plot of predicted versus actual $\text{RBANS}_{\text{delayed}}$ values. B) Circle plot of significant connections between brain areas (using node degree threshold of 18). C) Glass brain plot of significant nodes and connections.

Table 2.4: Top 5 highest degree nodes for PLS-BETA models with each data/measure result, with both Talairach Atlas labels and Automated Anatomical Labeling (AAL) atlas labels.

Node	**Degree**	**MNI (x, y, z)**	**Talairach Label**	**AAL Label**
Object-location, $\text{RBANS}_{\text{total}}$				
215	19	(-56, -50, 10)	Temporal Lobe, Superior Temporal Gyrus	Temporal_Mid_L
194	18	(0, 30, 27)	NA	Cingulum_Ant_L
175	16	(40, 18, 40)	Frontal Lobe, Middle Frontal Gyrus	Precentral_L
169	15	(49, -42, 45)	Parietal Lobe, Inferior Parietal Lobule	Frontal_Inf_Tri_R
222	14	(10, -62, 61)	Parietal Lobe, Precuneus	Angular_L
Face-name, $\text{RBANS}_{\text{total}}$				
198	21	(26, 50, 27)	Frontal Lobe, Superior Frontal Gyrus	Frontal_Mid_L
165	18	(47, 10, 33)	Frontal Lobe, Middle Frontal Gyrus	Precentral_R
108	17	(13, 30, 59)	Frontal Lobe, Superior Frontal Gyrus	Frontal_Sup_Medial_R
140	16	(29, -77, 25)	Occipital Lobe, Sub-Gyral	Occipital_Mid_R
64	15	(6, 67, -4)	NA	Frontal_Med_Orb_R
Face-name, $\text{RBANS}_{\text{delayed}}$				
85	24	(-10, 39, 52)	Frontal Lobe, Superior Frontal Gyrus	Frontal_Sup_Medial_L
92	23	(6, 54, 16)	Frontal Lobe, Medial Frontal Gyrus	Frontal_Sup_Medial_R
140	20	(29, -77, 25)	Occipital Lobe, Sub-Gyral	Occipital_Mid_R
108	18	(13, 30, 59)	Frontal Lobe, Superior Frontal Gyrus	Frontal_Sup_Medial_R
89	18	(13, 55, 38)	Frontal Lobe, Superior Frontal Gyrus	Frontal_Sup_R

Table 2.5: Top 5 highest degree nodes for CPM models with each data/measure result, with both Talairach Atlas labels and Automated Anatomical Labeling (AAL) atlas labels.

Node	**Degree**	**MNI (x, y, z)**	**Talairach Label**	**AAL Label**
Face-name, $RBANS_{total}$, Negative Edges				
145	21	(24, -87, 24)	Occipital Lobe, Cuneus	Occipital_Sup_R
139	20	(15, -87, 37)	Parietal Lobe, Precuneus	Cuneus_R
80	20	(15, -63, 26)	Occipital Lobe, Precuneus	Precuneus_R
159	18	(-47, 11, 23)	Frontal Lobe, Sub-Gyral	Frontal_Inf_Tri_L
140	18	(29, -77, 25)	Occipital Lobe, Sub-Gyral	Occipital_Mid_R
Object-location, $RBANS_{total}$, Positive Edges				
248	15	(34, 38, -12)	Frontal Lobe, Middle Frontal Gyrus	Frontal_Inf_Orb_R
270	13	(-29, -12, -22)	Limbic Lobe, Parahippocampa Gyrus	Hippocampus_L
242	12	(-21, -22, -20)	Limbic Lobe, Parahippocampa Gyrus	ParaHippocampal_L
215	12	(-56, -50, 10)	Temporal Lobe, Superior Temporal Gyrus	Temporal_Mid_L
182	12	(11, -39, 50)	Frontal Lobe, Paracentral Lobule	Cingulum_Mid_R
Object-location, $RBANS_{total}$, Negative Edges				
227	16	(-33, -46, 47)	Parietal Lobe, Sub-Gyral	Parietal_Inf_L
214	14	(54, -43, 22)	Parietal Lobe, Inferior Parietal Lobule	Temporal_Sup_R
183	12	(55, -45, 37)	Parietal Lobe, Supramarginal Gyrus	SupraMarginal_R
33	12	(51, -6, 32)	Frontal Lobe, Precentral Gyrus	Postcentral_R
197	11	(31, 56, 14)	Frontal Lobe, Middle Frontal Gyrus	Frontal_Mid_R

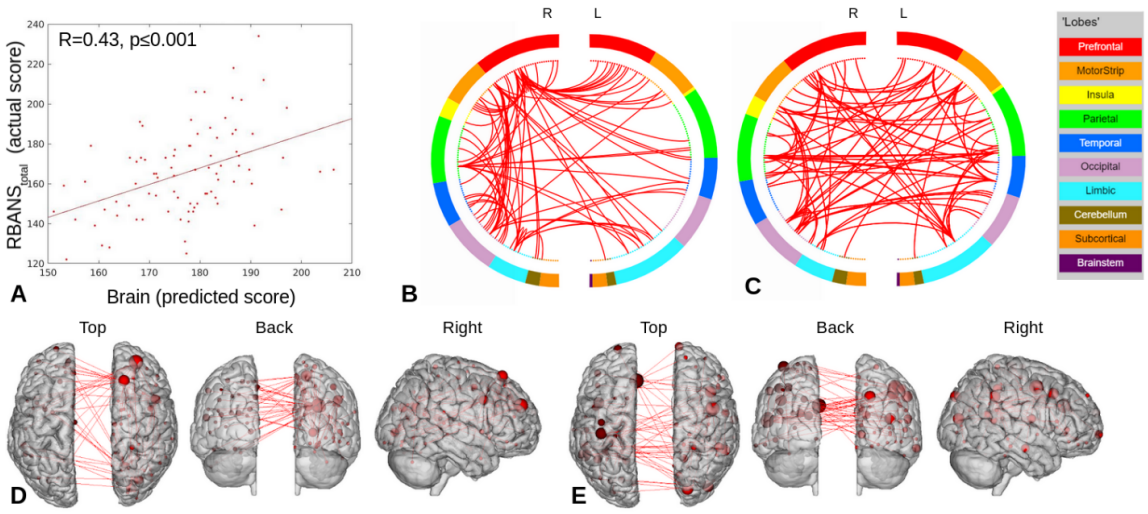

Figure 2.7: $\text{RBANS}_{\text{total}}$ raw score PLS-BETA results for combined face-name and object-location task data. A) Plot of predicted versus actual $\text{RBANS}_{\text{total}}$ raw score values. B) Circle plot of significant connections between brain areas for face-name task data (using node degree threshold of 12). C) Circle plot of significant connections between brain areas for object-location task data (using node degree threshold of 8). D) Glass brain plot of significant nodes and connections for face-name task data. E) Glass brain plot of significant nodes and connections for object-location task data.

($R=0.42$, $p\leq0.05$ for CPM positive edges, $R=0.35$, $p\leq0.05$ for CPM negative edges). CPM also yielded significant relationships between object-location task fMRI and $\text{RBANS}_{\text{delayed}}$ ($R=0.28$, $p\leq0.05$ for CPM positive edges) and $\text{RBANS}_{\text{total}}$ ($R=0.41$, $p\leq0.05$ for CPM positive edges).

2.4 Discussion

PLS-BETA and CPM of task-based fMRI data predicted independent measures of memory and global cognition in those with MCI, supporting other studies finding that these predictive modeling approaches are successful [180]. In the Run 1 results, PLS-BETA was able to identify significant relationships with more measures ($\text{RBANS}_{\text{total}}$ and $\text{RBANS}_{\text{delayed}}$) whereas CPM only identified significant relationships with one measure: $\text{RBANS}_{\text{total}}$. For CPM with $\text{RBANS}_{\text{total}}$, negative edges resulted in the only significant findings for face-name task data, while both positive and negative

Table 2.6: PLS-BETA and CPM Results Comparison, Run 2.

	CPM					
	Face-name		**Object-location**		**Resting-state**	
Behavioral Data	$\mathbf{R_{pos}}$	$\mathbf{R_{neg}}$	$\mathbf{R_{pos}}$	$\mathbf{R_{neg}}$	$\mathbf{R_{pos}}$	$\mathbf{R_{neg}}$
$\mathbf{RBANS_{delayed}}$	**0.32***	0.18	**0.28***	0.15	0.10	0.09
$\mathbf{RBANS_{total}}$	**0.42***	**0.35***	**0.41***	0.15	0.13	0.03
MoCA	-0.24	0.21	0.12	0.22	0.05	-0.16

	PLS-BETA		
	Face-name	**Object-location**	**Resting-state**
Behavioral Data	**R**	**R**	**R**
$\mathbf{RBANS_{delayed}}$	**0.30***	0.25	0.09
$\mathbf{RBANS_{total}}$	0.19	**0.30***	0.07
MoCA	0.03	-0.11	-0.04

* $p \leq 0.05$, ** $p \leq 0.001$, obtained from 1,000 permutations.

edges yielded significant relationships using object-location association task data. In the Run 2 results, PLS-BETA and CPM both identified significant relationships with $\text{RBANS}_{\text{total}}$ and $\text{RBANS}_{\text{delayed}}$. The success of the PLS-BETA model may be attributed to maximizing the covariance between predictor and response data, rather than developing weights based solely on the predictor data. PLS-BETA may also benefit from not separating positive and negative edges as in CPM.

In comparing the Run 1 and Run 2 results, several different significant relationships with both modeling approaches are observed. Of note, the Run 1 relationship identified by PLS-BETA between $\text{RBANS}_{\text{total}}$ and face-name task fMRI does not stay consistent in Run 2. In this study, while neuropsychological assessments are administered once per session, fMRI scans are completed twice (two runs) per session. Therefore, the only difference in model input is from predictors. Changes in results between runs can potentially be attributed to changes in participant engagement, attention, or practice effects with task-based fMRI. Other studies have found that practice improves performance and alters the underlying brain activity in working memory tasks [55, 133]. This indicates the need for further study of the stability of such predictive modeling approaches with task-based fMRI.

However, in both runs, no significant relationships resulted from using resting-state data. These results support other findings that task-based predictors relevant to the response variable add significant benefit, compared to resting-state predictors [68, 93]. The results of this study indicate that the object-location and face-name tasks used here are well-equipped to emphasize brain-behavior relationships in diseases and disorders that affect cognition. Despite these findings favoring task-based fMRI, resting-state fMRI maintains an advantage due to its ease of completion for subjects, especially those with impairments. Functional connectivity from resting-state fMRI has been found to successfully predict the degree of cognitive impairment from subjects along the AD spectrum [119]. This warrants further study about the value of task versus resting-state fMRI data in predictive modeling.

PLS-BETA and CPM both identified clinically relevant areas involved in MCI, such as the superior frontal gyrus, superior temporal gyrus (STG), inferior parietal lobule (IPL), and precuneus. High degree nodes located in the frontal and parietal regions may be indicative of compensatory-related increased activity in these regions in those with MCI [61, 82, 149]. The inferior parietal lobule, involved in the default mode network, tends to exhibit increased functional connectivity in those with amnestic MCI [139]. Memory deficits are linked to temporal lobe atrophy and dysfunction [160, 171]. Several areas were highlighted in both modeling approaches, including the IPL, precuneus, and STG. This indicates that these areas may be generally implicated in MCI and warrant further consideration in future studies.

One limitation of this work is the small sample dataset ($n<100$) that that warrants a leave-one-out cross-validation scheme. A larger dataset could also be tested with k-fold cross-validation to reduce variability, but potentially at the cost of increasing bias. PLS-BETA can also benefit from parameter tuning to ensure the optimal selection of regression coefficient features.

Small effect sizes are common with neuroimaging-based predictive modeling. How-

ever, insights gained from neuroimaging-based models are unlikely to be the sole considerations contributing to a clinical decision. Other indicators would likely be used, either in combination with modeling results, or as additional input to a predictive model. The methods described here serve to introduce new fMRI tasks and analysis approaches, as well as identify brain regions impacted early in disease states that warrant further study of their role in the application of interest.

One impact of multivariate models is that additional predictor data can be easily included in the model, via simple internal concatenation, to increase inclusion of important features in the model and boost prediction performance. External aggregate methods with multiple types of data have also demonstrated increased performance in prediction [146]. In the context of MCI, combining multiple datasets and/or modalities per subject has the potential to enhance predictive capabilities. For example, combining multiple types of task and resting-state fMRI data along with other modalities or contrasts such as arterial spin labeling (ASL) or myelin water imaging can provide complementary information about the participants' neurofunctional states. Additionally, the high likelihood of comorbidities for patients that are presumed to have an Alzheimer's disease etiology warrants further study of predictive models combining multiple comorbidities. One study has demonstrated that predictive modeling can identify commonalities between complex and potentially intertangled disorders such as autism spectrum disorder and attention-deficit/hyperactivity disorder [108]. A similar approach in the context of dementia could likewise elucidate transdiagnostic neurofunctional differences in the many potential causes of dementia, including Alzheimer's disease.

As PLS-BETA is a linear process, future work will examine nonlinear approaches to dimensionality reduction for this context. Variational autoencoders have demonstrated utility in encoding fMRI activity [77, 101], and this latent representation of the data may potentially be useful for predictions. These methods can also be extended

to other datasets such as those of the Alzheimer's Disease Neuroimaging Initiative (ADNI).

In addition, the fMRI data used in this work is based on anatomical alignment of subjects using structural MRI. Current research indicates that hyperalignment, an alternative to anatomical alignment, provides functional connectivity in a common high-dimensional information space across subjects and may therefore preserve unique fine-scale information about subjects [23]. Another area of future investigation can utilize hyperalignment of the fMRI data analyzed in this work in combination with brain-behavior predictive models to provide different aspects of functional connectivity.

In future work, predictive modeling approaches such as PLS-BETA may be able to provide useful insights into the potential targets and/or impacts of therapeutic interventions as well as indications of imminent neurological symptoms.

2.5 Conclusion

This study demonstrated that PLS-BETA is a relevant prediction technique for MCI-related memory and cognition changes. PLS-BETA classified brain-behavior relationships using two types of task-based functional connectivity and outperformed PLS-BETA models developed with resting-state functional connectivity. Overall, task-based functional connectivity predictors that "stress" memory and cognition systems proved to be effective in the estimation of memory and cognition performance with both the PLS-BETA and CPM techniques.

CHAPTER III

Extension of Predictive Modeling Framework for Arterial Spin Labeling Cerebral Blood Flow

3.1 Introduction

Early detection is critical to the intervention of Alzheimer's disease (AD), as AD-related changes in the brain occur many years before symptoms or diagnosis. However, the pathogenesis of AD has numerous contributing factors of uncertain or varying degrees of importance (e.g., proteinopathy, vascular disease, genetic components, etc.) that complicate early detection. Thus, it is important to understand each component individually as well as their combined effects. One common observation in Alzheimer's disease is the vascular effect of cerebral hypoperfusion [38, 105, 147]. Arterial spin labeling (ASL) is a quantitative MRI-based measure of perfusion. ASL data is acquired on standard MRI scanners using specialized pulse sequences to label blood in the neck and observe its perfusion through the brain. This MRI-based modality is noninvasive and eliminates the need for injections of radioactively labeled tracers that are needed to examine perfusion in other imaging modalities, such as positron emission tomography (PET) or single photon emission computed tomography (SPECT). ASL has demonstrated cerebral hypoperfusion in AD that is consistent with other modalities [95]. Furthermore, lower cerebral blood flow (CBF) as measured

by ASL has been directly related to cognitive decline and multi-domain impairments in AD [17, 114].

This work aims to relate ASL CBF data to external measures of cognitive performance in a predictive modeling framework. Ultimately, the brain-behavior relationships illuminated by this analysis are hypothesized to identify scientifically relevant brain regions impacted by AD. Further study of these brain regions may contribute to the understanding of neural and vascular effects in AD.

This work examines composite measures of cognition and their relationship with ASL-measured CBF. Composite scores combining several test scores have been widely used in the context of mild cognitive impairment (MCI) and dementia of the Alzheimer's type (DAT) [60, 80, 94]. Combinations of different neuropsychological or cognitive assessments have demonstrated equal or improved performance as compared to their individual components [31], indicating that these composite scores may be able to better capture the multifaceted and highly variable continuum of AD. For example, a composite score for executive functioning matched or exceeded the performance of its individual components in several tasks, including predicting conversion to dementia, detecting temporal changes, and associations with MRI or cerebrospinal fluid-based measures [60]. Here, composite scores are derived for several AD-related domains, including language, memory, and learning, as response variables to evaluate the predictive performance of ASL-measured CBF.

In this work, the widely used connectome predictive modeling (CPM) machinery [159] is extended to a different input data type: arterial spin labeling (ASL) volumetric CBF maps, as well as composite measures of memory, learning, and language performance. ASL data has been commonly used to predict AD status and risk of conversion from early stages to later stages [24]. To the authors' knowledge, this is the first application of ASL measures in a predictive modeling framework to relate to continuous composite measures of memory and cognition in AD. This "voxel-wise

predictive modeling" (VPM) approach aims to relate volumetric ASL data to predict cognition and memory in subjects with MCI and DAT, along with healthy subjects. We hypothesize that the ASL CBF data provides predictive information in relation to these external measures of cognition in AD.

3.2 Methods

3.2.1 Data

Structural T1w MRI and arterial spin labeling-derived volumetric cerebral blood flow maps were obtained for 90 subjects, including cognitively normal (CN) individuals and those with a diagnosis of MCI or DAT (mean age 79.4, standard deviation 7.2, 48 CN/22 MCI/20 DAT) enrolled at the Michigan Alzheimer's Disease Research Center. T1w images and ASL data were acquired using a Nova Medical 32-channel head coil on a 3T MR750 GE Discovery scanner using GE's 3D pseudo-continuous ASL (pCASL) sequence. T1w scan parameters included an image size of 256x256x208 with 1 mm^3 resolution. Scan parameters included TR/TE of 4.902 s/10.8 ms, post-labelling delay of 2.025 s, image size of 128x128x40, 1.75 x 1.75 mm resolution, 40 slices, 3.5 mm slice thickness, and 3 signal averages.

3.2.2 Neuropsychological Measures

In this work, the response variables consisted of measures of cognitive and memory function that were obtained at the time of scanning. Several composite measures were defined (corresponding components for each composite score are listed below). A fourth neuropsychological measure analyzed in this work is the Montreal Cognitive Assessment (MoCA), that was designed for screening of mild cognitive impairment [130]. MoCA includes tasks focusing on several domains: short-term memory recall, delayed recall, visuospatial abilities, executive function, sustained attention, language,

and orientation to time and place.

- Learning composite score: mean of z-scores for Craft Story Immediate Recall (both verbatim and paraphrase) [30] and Hopkins Verbal Learning Test (HVLT) Immediate Recall [22].

- Memory composite score: mean of z-scores for Craft Story Delayed Recall (both verbatim and paraphrase) [30], Hopkins Verbal Learning Test (HVLT) Delayed Recall [22], and Benson Complex Figure Recall [136].

- Language composite score: mean of z-scores for Controlled Oral Word Association (COWA) Phonemic Fluency test-version CFL [153], Semantic Fluency (both animal and vegetable) [5], and Multilingual Naming Test (MINT) Total Score [87].

- MoCA z-score.

3.2.3 Preprocessing

ASL data were preprocessed using an automated toolbox, ExploreASL [129] version 1.9.0 (10.5281/zenodo.5809216), including Statistical Parametric Mapping (SPM) 12 [6, 48], Computational Anatomy Toolbox (CAT) 12 [56], Lesion Segmentation Toolbox (LST) v2.0.15 [37, 157], and with Matlab 2020a. The standard ExploreASL preprocessing pipeline was selected, with the additional partial volume correction (PVC) option. The standard pipeline includes white matter hyperintensity correction, segmentation, spatial normalization, motion correction, registration, CBF quantification, and PVC. Further details of the standard pipeline are described in [129]. Additionally, normalization to the MNI152 template was performed with SPM12. The resulting CBF maps were used for further analysis, as shown in Figure 3.1. A normalized gray matter tissue segmentation was obtained for each subject using T1w

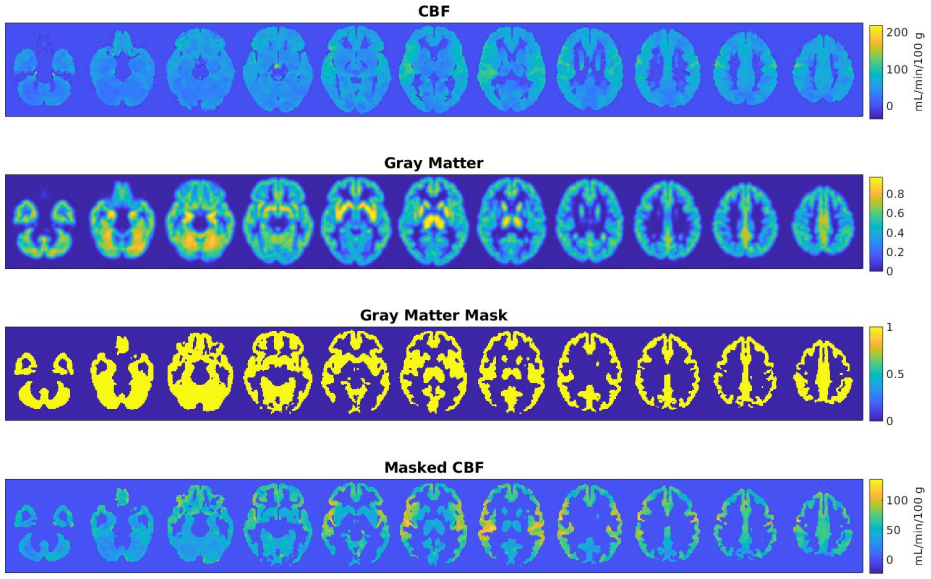

Figure 3.1: ASL CBF data (top), smoothed gray matter segmentation (2nd row), final overlapping gray matter masks (3rd row), and masked CBF (4th row) for a representative subject. The masked CBF data are used as the input to VPM.

images in SPM12 with the default parameters. To best capture continuous gray matter regions (i.e., without gaps), the gray matter tissue segmentation was smoothed with a Gaussian kernel at 6 mm FWHM and then thresholded at 0.3. Then, the overlapping union of gray matter regions across all subjects was used as the final mask for the entire CBF dataset to ensure that each subject had the same number of possible features.

3.2.4 Modeling

The voxel-wise predictive modeling approach is depicted in Figure 3.2. In a cross-validation framework (leave-one-out was used in this work, but k-fold cross-validation can be easily adopted), the CBF maps with or without a gray matter mask were used as voxel-wise predictor input data. Age was regressed from the predictors separately

for train and test partitions. A CPM-like framework was used; however, rather than connectome edges as input for each subject, VPM uses voxels, specifically voxels from volumetric ASL CBF maps. First, each voxel (across subjects) in the CBF maps is correlated with response variable (across subjects). Those voxels exceeding the predetermined threshold of significance ($p<0.01$, based on the original CPM methodology [159]) are used to generate feature masks. Similar to CPM, this is done separately for positive and negative correlations, resulting in two sets of feature masks (positive and negative). Finally, the input training data values within regions of the feature mask are used to fit a linear model with the training responses, and this model is tested on the held-out set to generate a prediction. After all folds are completed, the model performance is evaluated by correlating predicted and actual responses.

Permutation testing was completed via pseudorandom shuffling of the neuropsychological measures to estimate the null distribution. The resultant distribution was used to assess significance of the model fit. The number of voxels in each model was counted and divided by the total number of voxels in the final gray matter mask. Labels for the cluster locations identified by VPM were determined using MNI coordinates in WFU PickAtlas [122] from the Talairach Daemon [110] and the automated anatomical labeling (AAL) atlas [167].

3.3 Results

Figure 3.3 shows the resultant VPM relationships. Relationships were elucidated with positive voxels for several metrics; models using the learning and memory composite scores had the largest effect sizes and resulted in statistical significance ($p<0.05$) using permutation testing. There were no significant results for negative voxel models. For several of the negative voxel models (those using the learning, memory, and MoCA neuropsychological measures), no voxels exceeded the significance threshold after correlation with the measures, resulting in no relationship. The

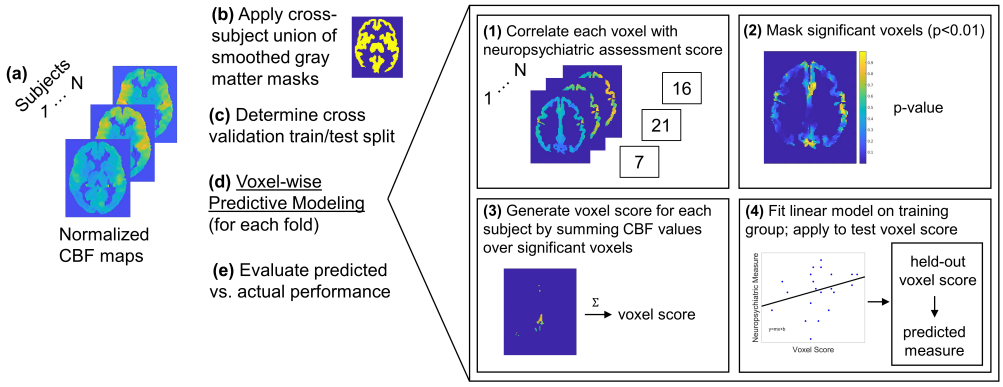

Figure 3.2: Schematic for Voxel-wise Predictive Modeling using ASL-measured CBF data. First, the preprocessed CBF maps are masked to gray-matter regions. Then, the data are partitioned into train/test groups based on a leave-one-out cross validation scheme. Each train set (including both predictors and responses) undergoes age regression and the same regression is applied to the test set. For each fold, each voxel of the masked CBF maps is correlated with neuropsychological measures. The resulting p-values are thresholded for significance at 0.01 to yield a mask of CBF map features. This is done separately for positive and negative correlations. Next, the feature mask is applied to the CBF values and all values are summed to create a voxel score for each subject. The voxel score for each subject is used as a predictor to estimate a linear model with the response neuropsychological measures. This model is applied to the left out subject to generate a behavior prediction. Once all folds have been completed, the model performance is assessed via correlation between actual and predicted behavior.

Table 3.1: ASL VPM Results for each Neuropsychological Measure.

	Learning	**Memory**	**Language**	**MoCA**
$\mathbf{R_{pos}}$	**0.20***	**0.20***	-0.04	0.11
$\mathbf{R_{neg}}$	0	0	0.09	0
Positive Voxels (count)	1624	1556	17	412
Positive Voxels (%)	1.05	1.01	0.011	0.27
Negative Voxels (count)	0	0	256	30
Negative Voxels (%)	0	0	0.17	0.02

* $p \leq 0.05$, ** $p \leq 0.001$, obtained from 1,000 permutations.

remaining negative voxel relationship, language, was not significant.

Figure 3.4 shows the corresponding feature masks resulting from the models for each of the neuropsychological metrics. The model performances and feature mask sizes are detailed in Table 3.1. The cluster locations are described in Table 3.2. For the learning and memory composite metrics, clusters were identified in the inferior parietal lobule, supramarginal gyrus, cingulate gyrus, and cerebellar tonsil.

3.4 Discussion

This work focuses on characterizing the predictive relationship between ASL-measured CBF and learning and memory performance. The results shown here indicate that measures of CBF correspond to external neuropsychological measures of cognition and memory in a predictive modeling framework. This supports other evidence that ASL-based CBF metrics correspond to cognitive performance and impairments [17, 114].

The learning and memory cluster locations and relationships highlight their similarity. The composite scores for learning and memory are both based on the Craft story and HVLT cognitive assessments, and only differ in the duration of recall period (immediate versus delayed) due to the nature of learning and memory. This is because learning can be thought of as "a process for acquiring memory" [132]. Similarities in the findings between the learning and memory composite metrics may

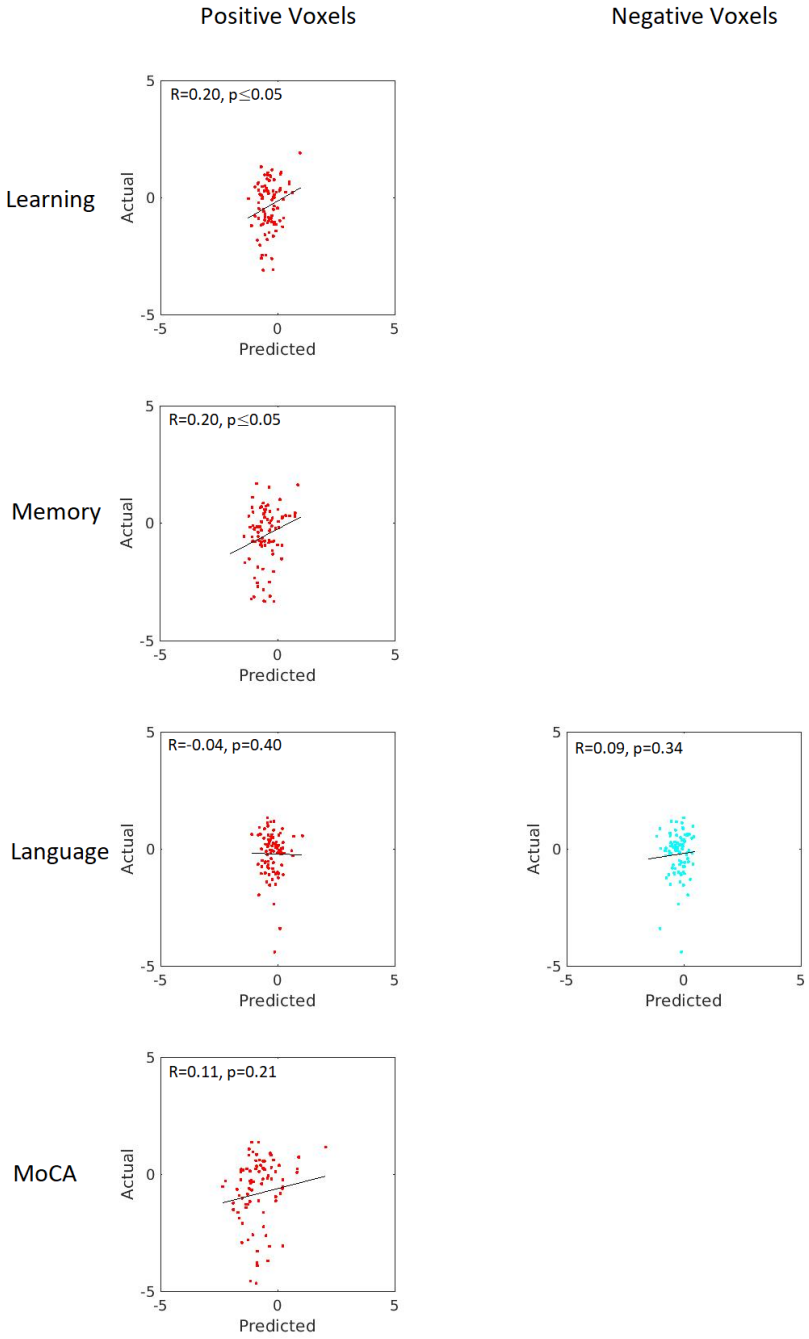

Figure 3.3: VPM plots showing predicted versus actual metrics for the learning, memory, and language composite scores as well as MoCA. The left column contains positive VPM results and the right column contains negative VPM results.

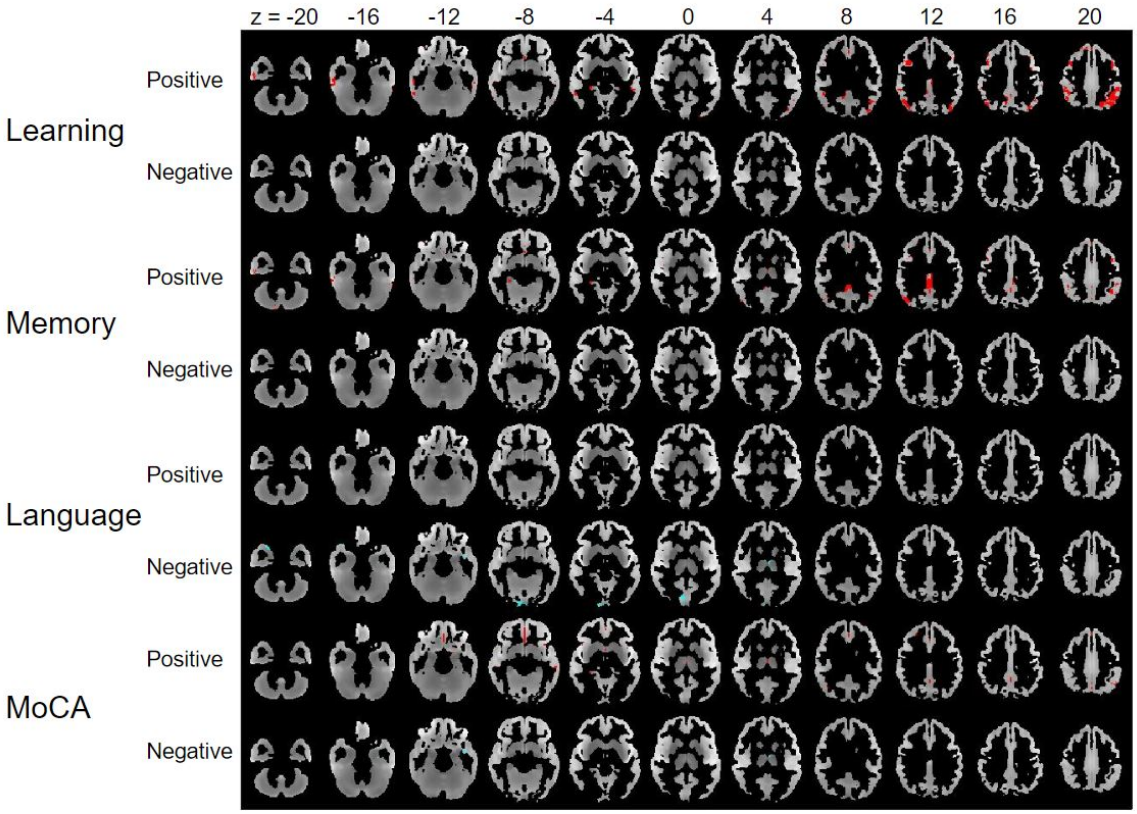

Figure 3.4: VPM feature masks for each neuropsychological measure overlaid on mean gray matter-masked CBF input data. Red depicts positive feature masks and cyan depicts negative feature masks. Images are in radiological orientation.

Table 3.2: Cluster locations for VPM positive or negative results with each neuropsychological measure, with both Talairach Atlas labels and Automated Anatomical Labeling (AAL) atlas labels.

Measure	**MNI (x, y, z)**	**Talairach Label**	**AAL Label**
Learning (positive)	(0, -33, 31)	Limbic Cortex, Cingulate Gyrus	Cingulum_Post_L
Learning (positive)	(47, -42, 30)	Parietal Lobe, Supramarginal Gyrus	Supramarginal_R
Memory (positive)	(36, -56, -51)	Cerebellum Posterior Lobe, Cerebellar Tonsil	Cerebellum_B_R
Memory (positive)	(47, -50, 21)	Parietal Lobe, Inferior Parietal Lobule	Temporal_Sup_R
Language (positive)	(1, 44, -22)	Frontal Lobe, Orbital Gyrus	Rectus_R
Language (negative)	(7, -64, -4)	Occipital Lobe, Lingual Gyrus	Lingual_R
MoCA (positive)	(43, 10, -2)	Sub-lobar, Insula	Insula_R
MoCA (positive)	(43, 33, -13)	Frontal Lobe, Middle Frontal Gyrus	Frontal_Inf_Orb_R

also be expected due to the overlaps in effects of pathology on learning and memory processes. Learning and memory are intertwined in disease states, such as AD, as both are impacted by pathological degradation of forebrain cholinergic systems [42], meaning that brain-behavior prediction may elucidate similar relationships using the two metrics.

Regions of the brain isolated in the VPM feature masks indicate involvement of brain regions that may be impacted in AD. The inferior parietal lobule (IPL), which formed a relationship with the memory composite score, has demonstrated involvement in AD. Disruptions in CBF have been specifically observed in the IPL in subjects with AD [170, 185]. In addition, regions in the cingulate gyrus that formed a relationship with the learning composite score may also be tied to AD. Synaptic loss and cortical thinning associated with AD neuropathology has been shown to occur within the cingulate gyrus [115, 156]. The supramarginal gyrus, which contributed to the relationship with the learning composite score, is also relevant in the context of AD. AD patients with depression have demonstrated increased CBF in the supramarginal gyrus as compared to AD patients without depression [116]. During a working memory task, AD subjects displayed increased fMRI activations in the supramarginal gyrus compared to controls [179]. In addition, the supramarginal gyrus may be involved in cognitive reserve for the normal elderly controls [176]. In the cerebellar tonsil, which contributed to the model with the memory composite score, altered glucose metabolism has been observed to indicate a potential for conversion to cognitive decline [34]. The involvement of these brain regions in the VPM results indicates the need for further analysis of these areas in relation to measures of CBF and behavior in the context of AD.

Optimally, multimodal combinations of data will be used in predictive models. ASL data has been shown to provide complementary information to other metrics, such as hippocampal volume [174]. Hippocampal volume can be examined using

structural T1-weighted MRI scans, as acquired here, and could be added to the VPM procedure as an additional predictor. Additionally, structural T1-weighted images can provide information about neuronal atrophy and have been used in deep learning models for prediction of AD status as well as conversion from MCI to DAT [10]. These acquisitions can be easily combined with ASL acquisitions to provide additional data about a subject. Combinations with other data types is hypothesized to enhance prediction, and should be examined in future work.

This study has several limitations. First, the sample size is small (N<100). However, since ASL CBF in AD is a relatively novel predictor type for this application in predictive modeling, this study demonstrates the potential of ASL predictors for further study. To reduce the impacts of the resultant small effect sizes, the predictors evaluated in this work can be combined with other data from other domains, such as other neuroimaging, demographics, genetics, clinical or other measures. Combining several predictors could improve accuracy of predictions.

ASL data fundamentally differs from fMRI data in that ASL yields a quantitative measure of cerebral blood flow whereas fMRI provides a proxy for neural activity. ASL data are typically acquired in the "resting-state," as was the case here. Since this is a novel application of ASL data where fMRI data have typically been used, resting-state ASL data are a good starting point. Furthermore, task-free acquisitions are beneficial for subjects with difficulties completing tasks. However, task-free acquisitions exclude the potential additional information from a task-based acquisition. Studies have demonstrated that ecologically-relevant tasks can provide a stress test for networks of interest, boosting signal in those regions [68, 180] as compared to resting-state fMRI. Similar to BOLD fMRI, ASL is sensitive to changes in task conditions [39], and can elucidate relationships between changes in cerebral blood flow and task demands. This sensitivity indicates that task-based ASL could be informative as a predictor in VPM. Task-based ASL as a predictor for brain-behavior modeling remains a recommended

focus for future work.

As described in earlier chapters, there are many options for predictive models, and different predictors may necessitate different modeling approaches. Overall, the novel application of ASL-derived CBF measures to predictive modeling demonstrated in this work has many opportunities for future extension and study.

3.5 Conclusion

Arterial spin labeling provides a noninvasive, nonionizing measurement of cerebral blood flow. This work demonstrates the utility of ASL-based perfusion measurement as a predictor for external measures of cognitive and memory status in patients with varying degrees of AD. Novel ASL acquisitions such as ASL fingerprinting also provide the potential for simultaneous estimation of other vascular parameters, including bolus arrival time, T1 relaxation, and blood volume. These additional parameters could also be used in the framework demonstrated here, along with other data types. Other opportunities for multimodal data approaches are further discussed in Chapter VI: Future Work.

CHAPTER IV

Representation Learning of Subjects Along the Spectrum of Alzheimer's Disease Using a Surface-based Variational Autoencoder Model

4.1 Introduction

Resting-state functional MRI (rsfMRI) has demonstrated value in evaluating behavioral or disease states, such as mild cognitive impairment (MCI) and dementia due to Alzheimer's disease [98, 175]. Functional MRI studies often seek to determine how brain activity is represented in the measured signal. However, the fMRI signal contains many sources of activity or fluctuation (including neurophysiology, cognition, head motion, physiological artifacts, etc.). Common analysis approaches use general linear models or data-driven approaches, such as ICA, to separate stimulus or other fMRI signals of interest from noise [14, 52]. However, these approaches are limited to detecting linear relationships within the data. Furthermore, since fMRI data are often high-dimensional in both space and time, specialized spatial or temporal dimensionality reduction techniques, such as functional connectivity, are implemented to infer brain network interactions and their relation to neurological or psychiatric disease states [50, 120].

Recent years have demonstrated increased interest in applications of machine

learning to medical images, including fMRI. Deep learning is a promising approach to analyze large datasets, such as fMRI, with nonlinear relationships. Representation learning is a type of machine learning focused on generating latent representations of input data. Kim, et al. recently demonstrated that these latent representations are successfully able to identify individuals using a variational autoencoder (VAE) model with resting-state fMRI [101]. The VAE model is of particular interest because it learns a latent representation that corresponds to disentangled fMRI sources and it is then also able to reconstruct or synthesize fMRI data. Essentially, the VAE model provides a nonlinear technique to reduce large fMRI data to identify a mixture of latent representations that may be able to encode between-subjects or other signal effects.

In a recent study, a variational autoencoder has been designed to encode high-dimensional rsfMRI activity patterns as low-dimensional (256-D) latent representations, and to use latent representations to generate or reconstruct rsfMRI patterns [101]. This VAE model is nonlinear, learnable from fMRI data alone and thus unsupervised or independent of any task or subject groups, and able to identify healthy subjects from their rsfMRI representations.

In this work, we ask whether the 2D VAE model trained with rsfMRI data from healthy volunteers can be readily generalizable to patients across the spectrum of Alzheimer's disease. For this purpose, the VAE model is applied to a cohort of cognitively normal older adults (CN), individuals with amnestic mild cognitive impairment (MCI), and individuals with dementia of the Alzheimer's type (DAT). We explore whether the VAE-derived latent representations of rsfMRI activity can separate these individual subjects, despite the model having no knowledge of disease states, and also how well it can perform classification of subtypes.

4.2 Methods

4.2.1 Data

Structural T1w MRI and resting-state fMRI data were obtained for 193 older adults (107 CN, 57 amnestic MCI, and 29 DAT) enrolled at the Michigan Alzheimer's Disease Research Center. T1w scan parameters included an image size of 256x256x208 with 1 mm^3 resolution. Functional scans were acquired on a 3T MR750 GE scanner with a 32 channel Nova Medical coil using multiband EPI (MB factor = 6), TR/TE = 0.8 s/30 ms, flip angle = 52, 2.4 mm isotropic resolution, 570 timepoints, and 60 slices. Participants were instructed to focus on a fixation cross.

4.2.2 Preprocessing

Results included in this manuscript come from preprocessing performed using *fMRIPrep* 20.2.0 ([44]; [43]; Research Resource Identifier (RRID): SCR_016216), which is based on *Nipype* 1.5.1 ([65]; [66]; RRID:SCR_002502).

4.2.2.1 fMRIPrep: Anatomical data preprocessing

The T1-weighted (T1w) image was corrected for intensity non-uniformity (INU) with `N4BiasFieldCorrection` [166], distributed with ANTs 2.3.3 [7, RRID:SCR_004757], and used as T1w-reference throughout the workflow. The T1w-reference was then skull-stripped with a *Nipype* implementation of the `antsBrainExtraction.sh` workflow (from ANTs), using OASIS30ANTs as target template. Brain tissue segmentation of cerebrospinal fluid (CSF), white-matter (WM) and gray-matter (GM) was performed on the brain-extracted T1w using `fast` [FSL 5.0.9, RRID:SCR_002823, 184]. Brain surfaces were reconstructed using `recon-all` [FreeSurfer 6.0.1, RRID:SCR_001847, 33], and the brain mask estimated previously was refined with a custom variation of the method to reconcile ANTs-derived and FreeSurfer-derived segmentations of the

cortical gray-matter of Mindboggle [RRID:SCR_002438, 104]. Volume-based spatial normalization to two standard spaces (MNI152NLin6Asym, MNI152NLin2009cAsym) was performed through nonlinear registration with `antsRegistration` (ANTs 2.3.3), using brain-extracted versions of both T1w reference and the T1w template. The following templates were selected for spatial normalization: *FSL's MNI ICBM 152 non-linear 6th Generation Asymmetric Average Brain Stereotaxic Registration Model* [[45], RRID:SCR_002823; TemplateFlow ID: MNI152NLin6Asym], *ICBM 152 Non-linear Asymmetrical template version 2009c* [[49], RRID:SCR_008796; TemplateFlow ID: MNI152NLin2009cAsym],

4.2.2.2 fMRIPrep Functional data preprocessing

For each of the BOLD runs per subject, the following preprocessing was performed. First, a reference volume and its skull-stripped version were generated using a custom methodology of *fMRIPrep*. A B0-nonuniformity map (or *fieldmap*) was estimated based on two (or more) echo-planar imaging (EPI) references with opposing phase-encoding directions, with `3dQwarp` [29] (AFNI 20160207). Based on the estimated susceptibility distortion, a corrected EPI (echo-planar imaging) reference was calculated for a more accurate co-registration with the anatomical reference. The BOLD reference was then co-registered to the T1w reference using `bbregister` (FreeSurfer) which implements boundary-based registration [72]. Co-registration was configured with six degrees of freedom. Head-motion parameters with respect to the BOLD reference (transformation matrices, and six corresponding rotation and translation parameters) are estimated before any spatiotemporal filtering using `mcflirt` [FSL 5.0.9, 92]. BOLD runs were slice-time corrected using `3dTshift` from AFNI 20160207 [29, RRID:SCR_005927]. The BOLD time-series were resampled onto the following surfaces (FreeSurfer reconstruction nomenclature): *fsaverage*. The BOLD time-series (including slice-timing correction when applied) were resampled onto their original,

native space by applying the transforms to correct for head-motion. These resampled BOLD time-series will be referred to as *preprocessed BOLD in original space*, or just *preprocessed BOLD*. The BOLD time-series were resampled into standard space, generating a *preprocessed BOLD run in MNI152NLin6Asym space*. First, a reference volume and its skull-stripped version were generated using a custom methodology of *fMRIPrep*. *Grayordinates* files [62] containing 91k samples were also generated using the highest-resolution `fsaverage` as intermediate standardized surface space. Several confounding time-series were calculated based on the *preprocessed BOLD*: framewise displacement (FD), DVARS and three region-wise global signals. FD was computed using two formulations following Power (absolute sum of relative motions, [138]) and Jenkinson (relative root mean square displacement between affines, [92]). FD and DVARS are calculated for each functional run, both using their implementations in *Nipype* [following the definitions by 138]. The three global signals are extracted within the CSF, the WM, and the whole-brain masks. Additionally, a set of physiological regressors were extracted to allow for component-based noise correction [*CompCor*, 15]. Principal components are estimated after high-pass filtering the *preprocessed BOLD* time-series (using a discrete cosine filter with 128s cut-off) for the two *CompCor* variants: temporal (tCompCor) and anatomical (aCompCor). tCompCor components are then calculated from the top 2% variable voxels within the brain mask. For aCompCor, three probabilistic masks (CSF, WM and combined CSF+WM) are generated in anatomical space. The implementation differs from that of Behzadi et al. in that instead of eroding the masks by 2 pixels on BOLD space, the aCompCor masks are subtracted pixels that likely contain a volume fraction of GM. This mask is obtained by dilating a GM mask extracted from the FreeSurfer's *aseg* segmentation, and it ensures components are not extracted from voxels containing a minimal fraction of GM. Finally, these masks are resampled into BOLD space and binarized by thresholding at 0.99 (as in the original implementation). Components are also calculated

separately within the WM and CSF masks. For each CompCor decomposition, the k components with the largest singular values are retained, such that the retained components' time series are sufficient to explain 50 percent of variance across the nuisance mask (CSF, WM, combined, or temporal). The remaining components are dropped from consideration. The head-motion estimates calculated in the correction step were also placed within the corresponding confounds file. The confound time series derived from head motion estimates and global signals were expanded with the inclusion of temporal derivatives and quadratic terms for each [154]. Frames that exceeded a threshold of 0.5 mm FD or 1.5 standardised DVARS were annotated as motion outliers. All resamplings can be performed with *a single interpolation step* by composing all the pertinent transformations (i.e. head-motion transform matrices, susceptibility distortion correction when available, and co-registrations to anatomical and output spaces). Gridded (volumetric) resamplings were performed using `antsApplyTransforms` (ANTs), configured with Lanczos interpolation to minimize the smoothing effects of other kernels [111]. Non-gridded (surface) resamplings were performed using `mri_vol2surf` (FreeSurfer).

Many internal operations of *fMRIPrep* use *Nilearn* 0.6.2 [1, RRID:SCR_001362], mostly within the functional processing workflow. For more details of the pipeline, see the section corresponding to workflows in *fMRIPrep*'s documentation.

The above boilerplate text was automatically generated by fMRIPrep with the express intention that users should copy and paste this text into their manuscripts *unchanged*. It is released under the CC0 license.

4.2.2.3 Geometric reformatting and additional preprocessing

The rsfMRI data were geometrically reformatted using the same methods as published in [101]. The Freesurfer-based spherical coordinates were sampled to a 192x192 grid for each hemisphere. Voxel-wise 3rd-order polynomial regression, 0.01-0.1 Hz

bandpass filtering [27], and normalization to 0 mean and 1 standard deviation were then applied.

4.2.3 Variational autoencoder

The pre-trained VAE model (Figure 4.1) consists of encoder and decoder portions, each containing 5 convolutional layers, as in [101]. The model, with β=9, encoded geometrically reformatted cortical surface-based rsfMRI data into a 256-D latent space and then decoded back to cortical space. The model used rsfMRI data from the Human Connectome Project (WU-Minn HCP Quarter 2) [168] for 100, 50, and 500 healthy subjects in the training, validation, and testing portion, respectively. Each subject's scan acquired 1,200 time frames at a repetition time (TR) of 0.72 s. The pre-trained VAE was applied directly to rsfMRI data from every time point in every subject across the three groups (CN, MCI, DAT). The pre-trained model encoded this novel data set into low-dimensional (256-D) latent variables, and then decoded the latent variables into the original geometrically-reformatted fMRI space.

4.2.4 Visualization

The latent variable time courses for 30 subjects were visualized in a 2-dimensional space using t-Distributed Stochastic Neighbor Embedding (t-SNE) with cosine distance and a perplexity of 30, implemented in Matlab 2020a. The latent representations were then decoded to reconstruct the original rsfMRI data. Reconstruction performance was assessed by converting decoded outputs to original cortical space and computing correlation with smoothed cortical inputs using a 6 mm FWHM Gaussian kernel.

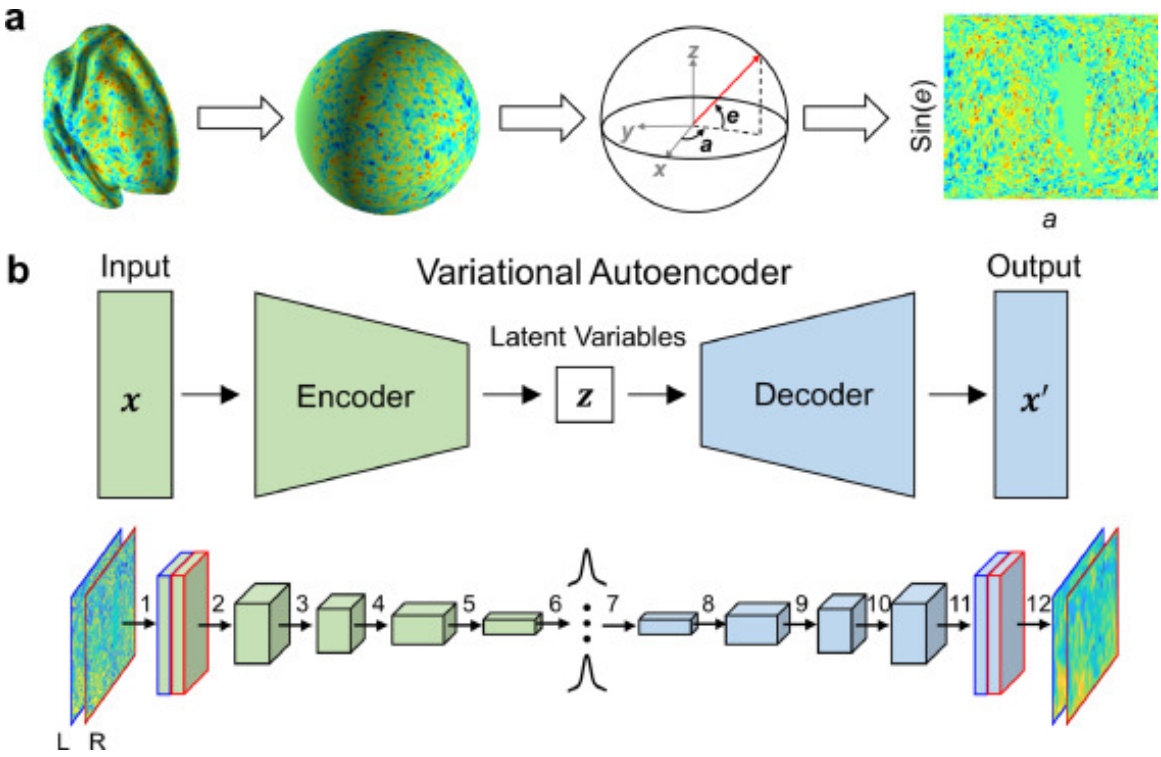

Figure 4.1: Schematic of the surface-based VAE model architecture, reprinted from [101] under Creative Commons-BY-NC-ND 4.0 license (https://creativecommons.org/licenses/by-nc-nd/4.0/).

4.2.5 Classification

In addition, the classification performance of latent variables was evaluated with two separate methods: (1) support vector machine (SVM) and (2) fully connected network classification. For the first approach, the mean latent variable μ values were used as input to an SVM classifier with a linear kernel and a box constraint (C) of 1 to classify both binary (CN vs. MCI, MCI vs. DAT) and multiclass (CN vs. MCI vs. DAT) groups. This was performed in a leave-one-out cross-validation framework. The fully connected network is shown in Figure 4.2. It was implemented as a separate module that takes the latent variable μ values as input and consisted of two fully connected layers and used cross entropy loss with class weights determined by class size to classify both binary (CN vs. MCI, MCI vs. DAT) and multiclass (CN vs. MCI vs. DAT) groups. The model was implemented in PyTorch 1.7.0 and trained for 10 epochs. Several hyperparameters were tested, including learning rate (1e-5, 1e-4, 1e-3) and number of hidden layers (100, 150, 200).

Several other approaches were initially investigated, including: support vector machine classification using k-means cluster centroids of latent variable means, Euclidean distance of latent variables across subjects, and latent variables' "functional connectivity" (i.e., pairwise correlations between different latent variables) as input to predictive modeling with external measures of memory and cognition. However, these approaches were not analyzed further due to poor initial performance on multiclass distinctions.

4.3 Results

Figure 4.3 shows the reconstruction performance of the encoded and decoded data. Across all three groups, the average correlation was approximately 0.8, which is comparable to the results in healthy subjects [101].

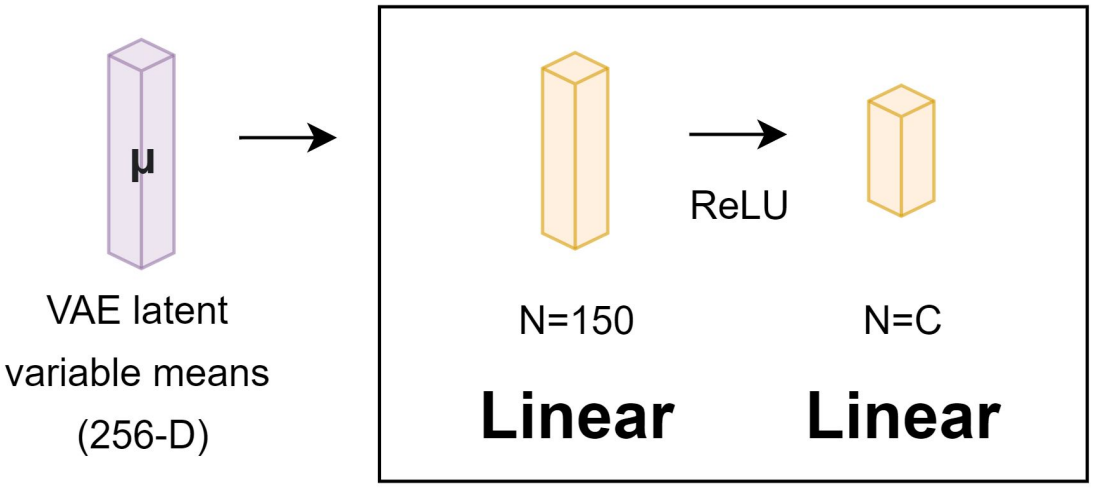

Figure 4.2: Architecture for fully connected neural network classification module. The latent variable means (256-D) from the pretrained VAE encoder are input to two linear layers with a ReLU activation between each layer. The first linear layer outputs a predetermined number of samples (100, 150, or 200 were tested). The second linear layer outputs C samples, where C is the number of classes used as input. For binary classification (CN vs. MCI, MCI vs. DAT), C=2 and for multiclass classification (CN vs. MCI vs. DAT), C=3.

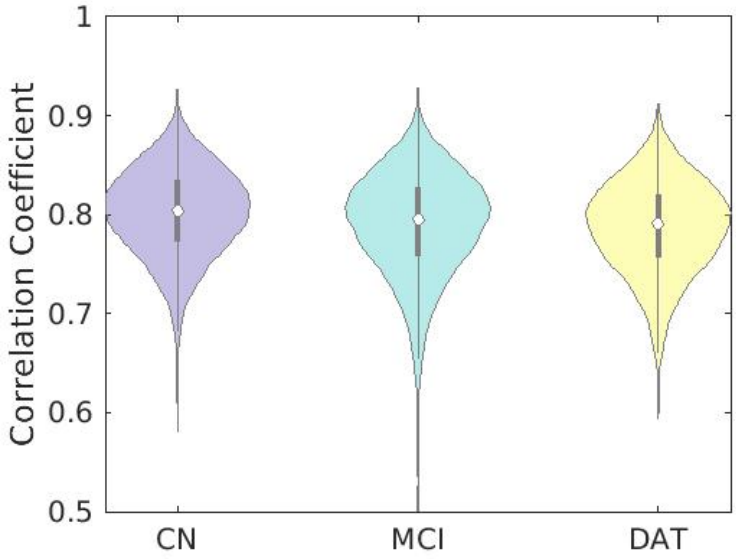

Figure 4.3: Reconstruction performance, assessed by correlation of VAE model input (smoothed, 6mm FWHM) and output in cortical space for each of the three groups (CN, MCI, DAT).

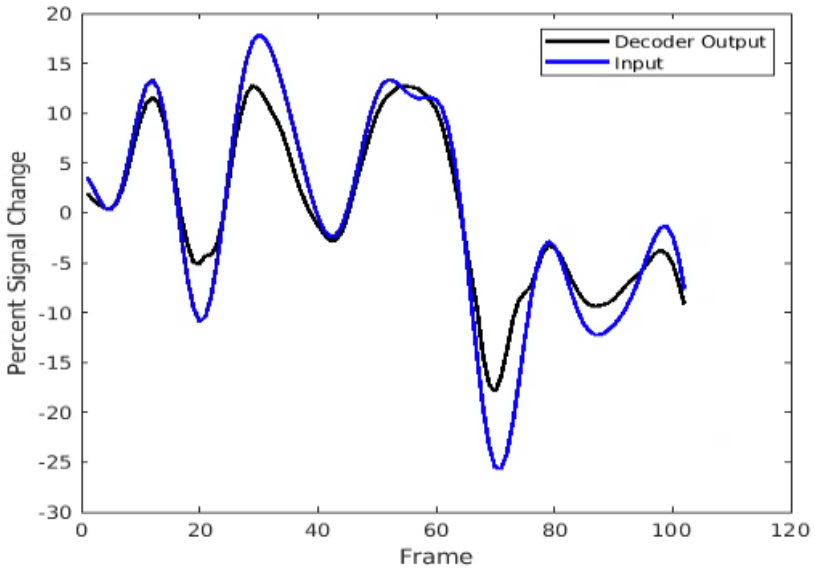

Figure 4.4: Timecourses of cortical input data and output in cortical space for a representative subject and brain region.

Figures 4.4 and 4.5 show representative timecourses from cortical input data and decoder output data for a representative subject and two representative brain regions. The mean correlation coefficient between input and output timecourses across brain regions was r=0.92. Temporal alignment was demonstrated with the input and decoded output.

The t-SNE visualization for subject-wise distinctions is demonstrated in Figure 4.6, which displays latent variable timecourses for 30 representative subjects. Figure 4.7 shows the same subjects' latent representations in a 2D t-SNE visualization, instead delineated by group. Figure 4.8 contains the 2D t-SNE visualization for all 193 subjects.

The classification results using SVM on time-averaged latent variable means are tabulated in Table 4.1 and achieved a maximum accuracy of 75% on binary classification between cognitively normal and dementia of the Alzheimer's type (DAT). The classification results using the full connected neural network on latent variable means are tabulated in Table 4.2 and achieved a maximum accuracy of 75% on binary

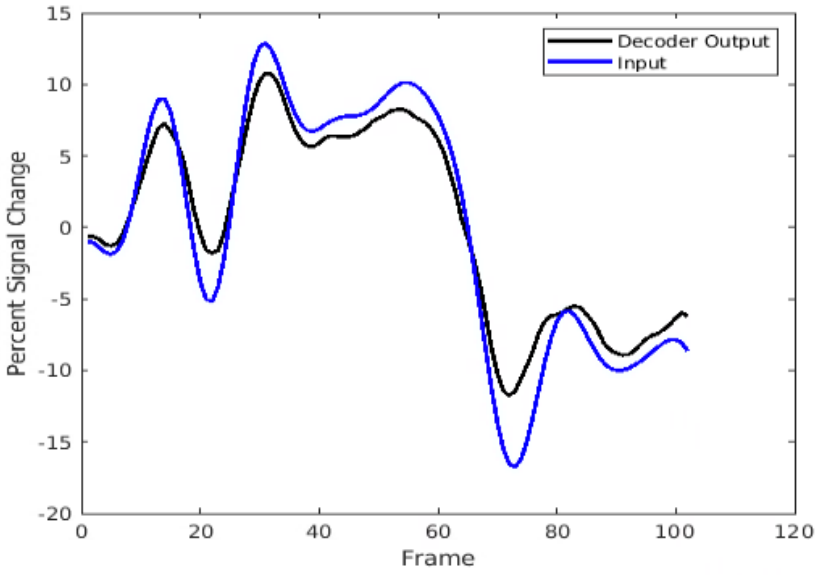

Figure 4.5: Timecourses of cortical input data and output in cortical space for a representative subject and brain region.

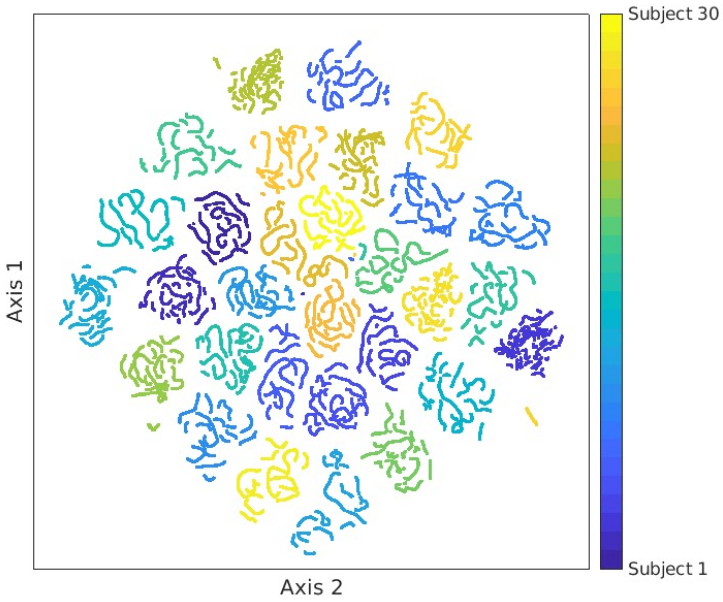

Figure 4.6: 2D t-distributed stochastic neighbor embedding (t-SNE) visualization of latent representations for 30 representative subjects.

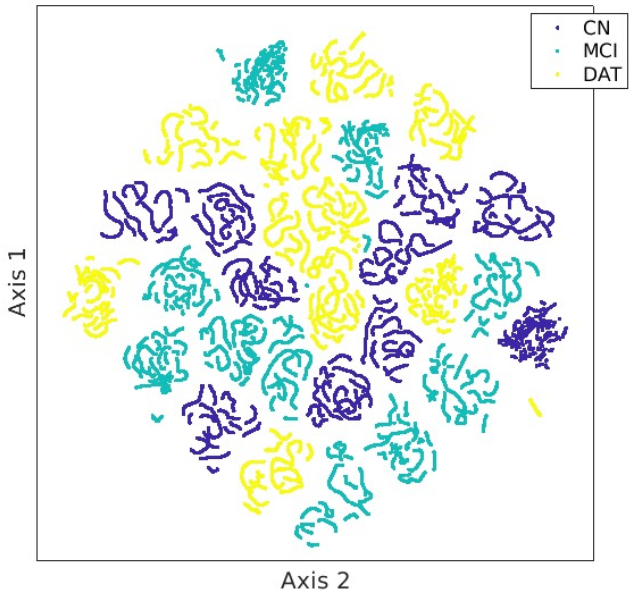

Figure 4.7: 2D t-distributed stochastic neighbor embedding (t-SNE) visualization of latent representations for 30 representative subjects.

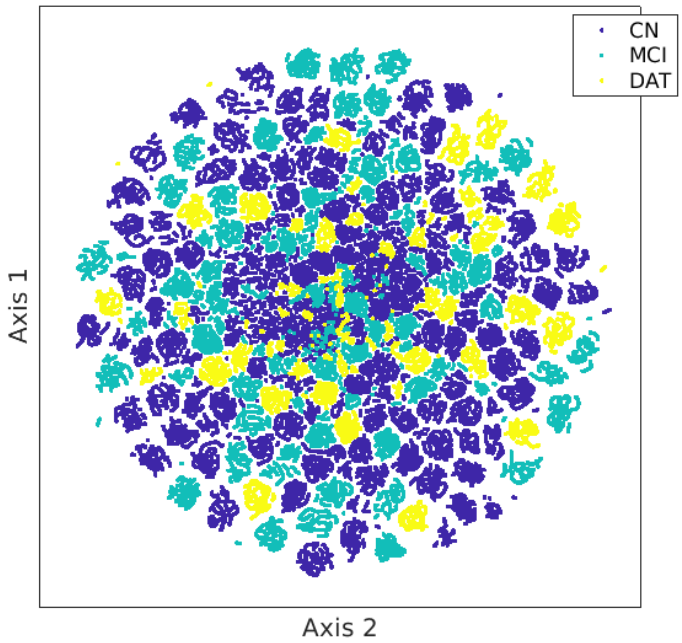

Figure 4.8: 2D t-distributed stochastic neighbor embedding (t-SNE) visualization of latent representations for all 193 subjects.

Table 4.1: SVM Classification Performance with 2D VAE Latent Variables. Classes consisted of either the original full sample (unbalanced) or were undersampled to achieve balanced groups. For multiclass classification, sensitivity and specificity for each group is listed in the order shown in the first column.

	Balanced (Yes/No)	**Accuracy** (%)	**Sensitivity** (%)	**Specificity** (%)
Binary (CN/DAT)	No	75	86	34
Binary (CN/MCI)	No	67	72	58
Multiclass (CN/MCI/DAT)	No	51	45	64
			65	42
			84	17
Binary (CN/DAT)	Yes	63	62	62
Binary (CN/MCI)	Yes	62	63	61
Multiclass (CN/MCI/DAT)	Yes	40	61	52
			59	38
			54	31

Table 4.2: Fully Connected Neural Network Classification Performance with 2D VAE Latent Variables. The model used a learning rate of 1e-5 and 150 samples for the first layer. Classes consisted of the original full sample (unbalanced groups) since class weights were used in the loss function. For multiclass classification, sensitivity and specificity for each group is listed in the order shown in the first column.

	Balanced (Yes/No)	**Accuracy** (%)	**Sensitivity** (%)	**Specificity** (%)
Binary (CN/DAT)	No	75	88	21
Binary (CN/MCI)	No	60	64	41
Multiclass (CN/MCI/DAT)	No	47	57	52
			37	64
			14	91

classification between CN and DAT.

4.4 Discussion

Our results indicate that the approach used here maintains individual separation when the model is applied to cortical surface fMRI data from participants with amnestic MCI or DAT as well as healthy controls, with low reconstruction error. This establishes that the VAE model is generalizable across subject populations despite differences in age and disease conditions. This was achievable even though the model was trained on healthy participants with no exposure to disease states such as amnestic MCI or DAT. However, the 2-D visualization using t-SNE does not yield group-wise distinctions, perhaps due to its lack of information about disease states. In addition, t-SNE is only one method for visualizing output from the VAE model to assess individual subject separation and alternative visualization approaches may not yield the same results.

While individual separation performs well, group-wise classification using latent variable means does not perform to the same degree as other classification works, such as those using structural MRI to achieve high sensitivity and specificity of near or over 90% [32], or those using functional MRI network analysis that achieve sensitivity and specificity of 85% and 80%, respectively [25]. This may be because the model is only trained to reconstruct outputs that are similar to the input while maintaining latent variables close to an independent and standard normal distribution. This model setup is only based on rsfMRI input data and does not include labels containing information about disease states. Another potential cause of lower than desired classification accuracy may be due to individual subjects that defy typical disease profiles, despite diagnosis. In other words, phenotype classification models may learn a disease profile that is actually comprised of several factors, including neurocognitive, clinical, and/or sociodemographic contributors, among others, and model failure is common

because this multitude of factors does not always generalize to all individuals [69]. Future work may investigate embedded or separate supervised classification modules in combination with the unsupervised VAE to improve classification performance.

The results shown here indicate that the VAE model is a promising technique for the study of brain activity in both healthy cohorts as well as those with neurological and psychiatric diseases. The VAE model can therefore be reasonably extended to populations in other areas in need of further study (e.g., Parkinson's disease, depression, attention-deficit hyperactive disorder (ADHD), and autism spectrum disorder). Studies in other patient populations could illuminate different low-dimensional representations indicating disease affects or other significant characteristics.

Future work could also investigate running this pre-trained VAE model on task data to evaluate generalization. Task-based fMRI can serve as a stress test to emphasize networks relevant to disease being studied. Memory or cognition tasks relevant to Alzheimer's disease may emphasize sources of brain activity relevant to Alzheimer's disease. Classification with latent variables as well as temporal dynamics are also of interest for further study.

Additionally, combining the insights discovered in this work with alternate biomarkers for Alzheimer's disease could elucidate further subtypes. For example, the amyloid, tau, or APOE status of the 193 subjects studied in this work could be added to the classification or low-dimensional embedding approaches to determine if those biomarkers have bearing on misclassified or misclustered samples.

As discussed in [101], the 2D surface-based model narrowly focuses on geometrically reformatted cortical brain activity since it is considered the center of human cognitive capabilities [144] and to promote ease of implementation via major reductions in computational burden. However, this introduces limitations by neglecting subcortical brain regions that could contain additional important information for clinical and cognitive science applications. In Chapter V, a volumetric model for

fMRI is considered.

4.5 Conclusion

Overall, the VAE model provides a mode of analysis of fMRI that may disentangle sources of brain activity. As an alternative to data dimensionality reduction techniques such as temporal correlation (i.e., in the context of fMRI, functional connectivity collapses the time dimension), the VAE latent networks can provide information about whole-brain and nonlinear relationships in the brain. Future work is needed to further investigate volumetric VAE models and classification.

CHAPTER V

Representation Learning of Resting-state Functional MRI Using a Volumetric Variational Autoencoder Model

5.1 Introduction

As demonstrated in [101] and Chapter IV, the surface-based variational autoencoder (VAE) model is capable of learning low-dimensional representations (256-D) of high-dimensional fMRI data in both healthy cohorts and subjects in the population spectrum of AD. This compression of rsfMRI data to a low-dimensional latent space has been shown to provide adequate encoding to perform individual identification [101], with great potential for other applications, including brain-behavior prediction and classification of disease states. As a generative model, the VAE also allows for the generation of fMRI samples from the low-dimensional space via the model's decoding portion.

In this work, we consider whether a similar VAE model trained with volumetric fMRI data (rather than a cortical subset of the data) is capable of encoding fMRI into low-dimensional representations, decoding these representations back into volumetric fMRI space, and also generating new fMRI patterns from the latent space. We hypothesize that the volumetric model will be advantageous for other applications that

may require the additional subcortical data, such as in studies of certain brain networks. For example, the subcortical component of the default mode network (DMN) has been understudied [4] and may provide additional information about brain activity. Altered DMN connectivity has been established as a hallmark difference between cognitively intact and mild cognitive impairment or dementia due to Alzheimer's disease [2, 18, 148, 173] or other neurological and psychiatric diseases. However, DMN activity is impacted in a nonspecific fashion; changes in the DMN are observed in many disorders, including depression [155], autism [97], schizophrenia [20], and post-traumatic stress disorder [112]. Since the VAE latent variables aim to represent sources of brain activity (and thereby, networks), this low-dimensional encoding could provide a novel representation or biomarker for different disorders, including Alzheimer's disease.

Since fMRI measurements may be a result of many potential sources (e.g., neural activity, motion, cardiac and/or respiratory, scanner noise), a remaining challenge is to identify how signals of interest (e.g., related to neural activity or stimuli) are encoded in the fMRI data. We hypothesize that a VAE model using volumetric fMRI may aid in the disentanglement of signal sources in future applications. We also hypothesize that using volumetric fMRI that is similar to the acquired format of the data (i.e., minimally preprocessed), improvements in ease of interpretation and implementation will be made. By eliminating the surface-based preprocessing and geometric reformatting as in [101], the computational burden of preprocessing is reduced. This provides for the potential of the volumetric VAE model to be incorporated into the initial fMRI reconstruction and analysis pipeline.

Existing studies of VAE models trained on fMRI data are focused on either cortical surface data and/or a subcortical subset of the volumetric data [57, 58, 100, 101, 177]. In this work, the variational autoencoder model aims to successfully categorize both whole-brain spatial and temporal patterns in volumetric resting-state fMRI.

This work aims to lay the groundwork for future integration of the VAE model into reconstruction and other fMRI analysis pipelines.

5.2 Methods

5.2.1 Data

For model training, validation, and testing, volumetric resting-state fMRI data from 400 healthy subjects was retrieved from the Human Connectome Project minimally preprocessed pipeline [168]. Each scan consists of 1,200 time frames sampled at a repetition time (TR) of 0.72 seconds, with 2 mm isotropic resolution covering the whole brain. The model was trained on 300 subjects' fMRI timecourses and validated on 100 subjects' fMRI timecourses. The first 10 frames were included to limit the data size for computation.

5.2.2 Preprocessing

In addition to the minimal preprocessing implemented in the HCP dataset, spatial smoothing with a FWHM of 6 mm was performed in Statistical Parametric Mapping software version 12 (SPM12; Wellcome Department of Human Neuroimaging, London, England). This was done to enable the model to learn from smoother spatial patterns, comparable to the smooth cortical data resulting from surface sampling and geometric reformatting in [101]. Next, voxel-wise 3rd-order polynomial regression, 0.01-0.1 Hz bandpass filtering [27], and normalization to 0 mean and 1 standard deviation were applied.

5.2.3 Variational autoencoder

We designed and implemented a 3D β-VAE [83] in a similar manner to the cortical surface-based β-VAE for fMRI [101] in order to learn low-dimensional representations

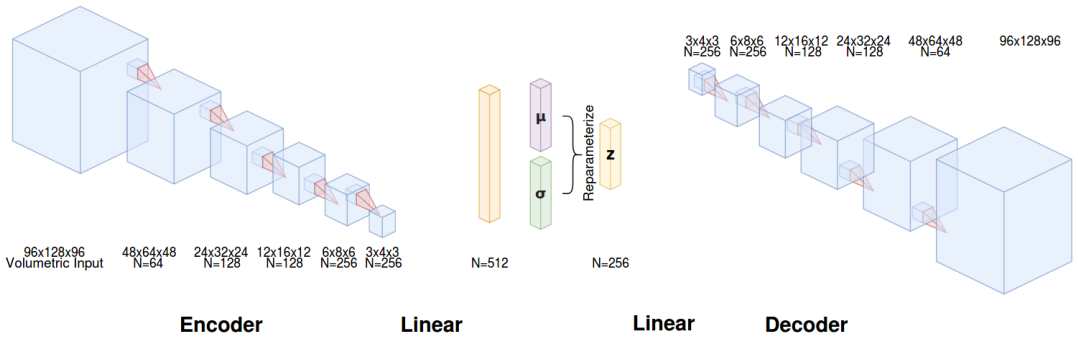

Figure 5.1: Schematic of the volumetric fMRI VAE model architecture. First, in the encoder portion of the model, volumetric inputs of size (96, 128, 96) go through 5 convolutional layers, each consisting of 3D convolution, 3D batch normalization, and ReLU activation. Each convolution uses a kernel size of (4, 4, 4), stride of (2, 2, 2), and padding of (1, 1, 1). The resultant feature map of dimensions (3, 4, 3) is then reshaped and input to a linear layer, which produces a vector of 256 latent variable distribution means. The means and log variance are reparameterized to yield a final z vector. This vector is input to another linear layer. On the decoder side, there are 5 blocks consisting of 3D transpose convolutions, 3D batch normalization and ReLU activation, all with the same hyperparameters as the encoder. The final output is a (96, 128, 96) dimensional volumetric dataset.

of the spatial features of volumetric fMRI. The VAE model is based on original work by [103]. The 3D VAE designed here is comprised of encoder and decoder portions that takes each volume of 3D fMRI data (96x128x96) as input. The encoder contained five 3D convolutional layers, including 3D batch normalization and leaky rectified nonlinearity. The linear layer used the resultant 3x4x3 feature map as input and yielded each latent variable distribution mean and standard deviation. The decoder followed a similar process to map the latent variables back to the volumetric fMRI space. The model was implemented in PyTorch 1.7.0 and the architecture is depicted in Figure 5.1.

$$L(\phi, \theta|x) = ||x - x'||_2^2 + \beta \cdot D_{KL}[N(\mu_z, \sigma_z)||N(0, I)] \quad [5.1]$$

Equation 5.1 is the loss function for the 3D model that is minimized during training through the optimization of encoding and decoding parameters (ϕ and θ, respectively). Similar to the surface-based (2D) VAE model [101], it consists of a reconstruction term assessed via mean squared error (MSE) and a regularization term using Kullback-Leibler divergence (KLD). The regularization term constrains the distribution of every latent variable to be close to an independent and standard normal distribution. The β parameter balances the trade-off of reconstruction performance and regularization. Figure 5.2 shows the model training curves for 100 epochs. The model was trained with stochastic gradient descent and the Adam optimizer [102], with a starting learning rate of 1e-5 and a batch size of 32. After evaluating model performance with and without learning rate decay, the learning rate was chosen to decay every 20 epochs by a factor of 10. Figure 5.3 shows the model training curves for 100 epochs without learning rate decay. Without learning rate decay, the reconstruction loss and KLD values were higher. An initial parameter sweep (β=0.1, 1, 10, 100) indicated that the optimal range for β was around 10 based on the final epoch training and validation loss and NRMSE of input and output rsfMRI data. A further parameter sweep, shown in Figure 5.4, showed that the optimal trade-off between MSE and KL divergence was around β=7$\sim$11. β=7 was chosen for further analysis.

5.2.4 Evaluation

Reconstruction performance was assessed using normalized root mean squared error (NRMSE) between the input data and decoded output. The normalized root mean squared error (NRMSE) between input and output was assessed with the following equation: NRMSE=$||x_{out} - x||_2/||x||_2$. Temporal alignment was assessed using correlation within a gray matter mask.

To evaluate the capability of the trained VAE model to disentangle fMRI sources, the latent variables from a novel subject's timecourse were clustered temporally with

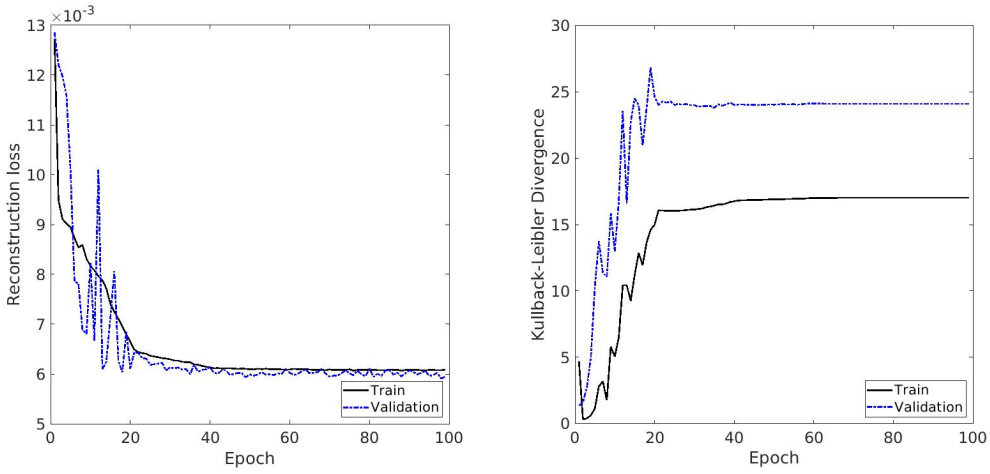

Figure 5.2: Plot of the MSE loss and Kullback-Leibler divergence for training and validation process over 100 epochs, with learning rate decay (by a factor of 10) every 20 epochs.

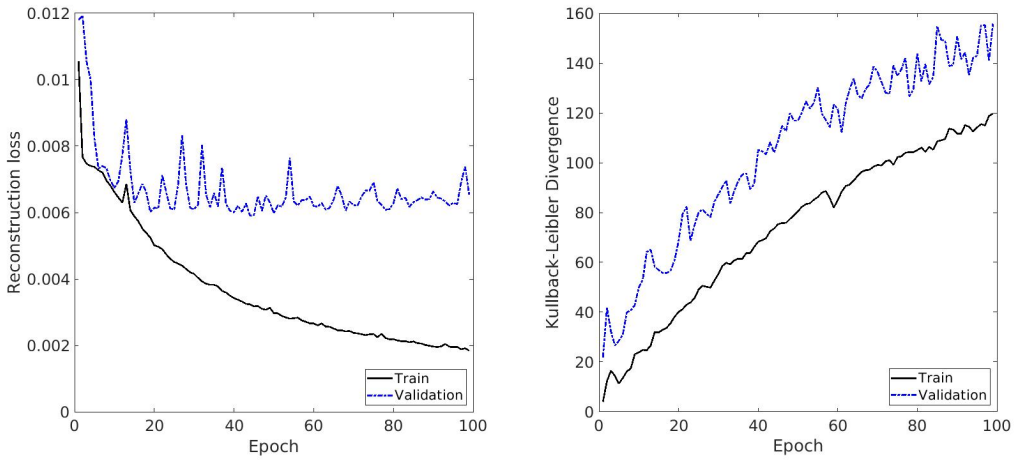

Figure 5.3: Plot of the MSE loss and Kullback-Leibler divergence for training and validation process over 100 epochs, without learning rate decay.

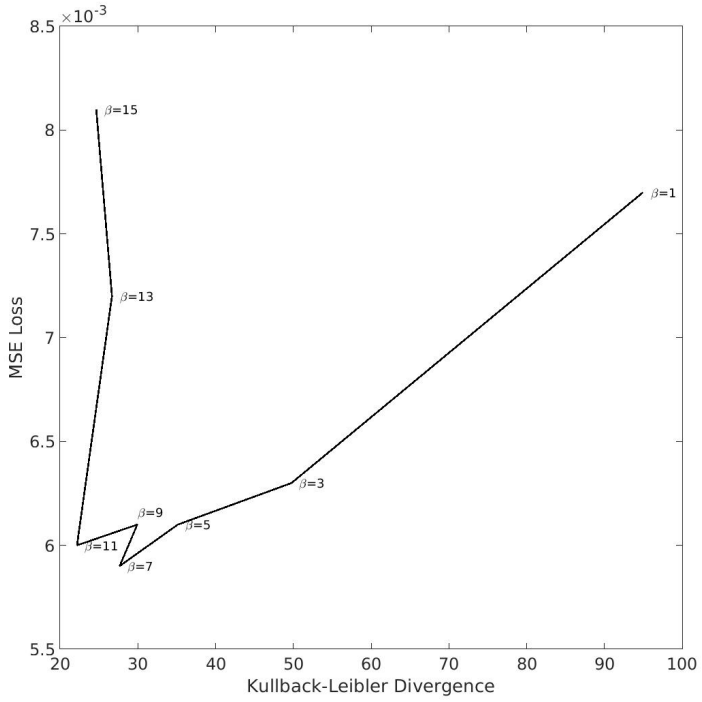

Figure 5.4: Plot of the trade-off between MSE loss and Kullback-Leibler divergence for varying values of β.

k-means clustering and k=8 clusters. Then, the clustered latent variables were decoded to volumetric space. The Dice coefficient was computed between decoded clusters and each of the Beckmann resting-state networks, thresholded at 2σ to allow for a binary mask to measure overlap.

To investigate whether the 3D VAE model learns low-dimensional representations of fMRI patterns and is also able to decode those representations into the original fMRI space, we synthesized fMRI data using the trained network. Samples from the prior distribution (i.e., standard normal distribution) were used to generate a timecourse containing 1,000 frames of fMRI patterns with the trained VAE decoder. These fMRI patterns were input to a temporal ICA with 23 components using the scikit-learn FastICA toolbox in Python 3.7.9. These were then compared to ICA maps from measured fMRI (1,000 frames) from a subject from the HCP dataset, as well as each of the Beckmann resting-state networks, also generated through ICA using 200 fMRI volumes from 10 subjects with 23 components [13]. This comparison was done using the Dice coefficient. First, the absolute values of the images were thresholded at the corresponding $\mu+2\sigma$ value. Then the Dice coefficient was computed with the thresholded binary images between each Beckmann RSN and each of the measured and synthesized ICA maps.

$$DSC = \frac{2|X \cap Y|}{|X| + |Y|} \qquad [5.2]$$

The Dice coefficient was computed using Equation 5.2, where X and Y are the binarized measured or synthesized ICA maps and the Beckmann RSNs, respectively. The highest Dice coefficient of the measured and synthesized ICA maps with each RSN is displayed in the Results. Finally, the correlation of the measured or synthesized ICA maps with each RSN was used to determine if sign-flipping was required for the measured and synthesized ICA maps. If the correlation was negative, the measured or synthesized ICA maps were negated to match the RSN ICA maps.

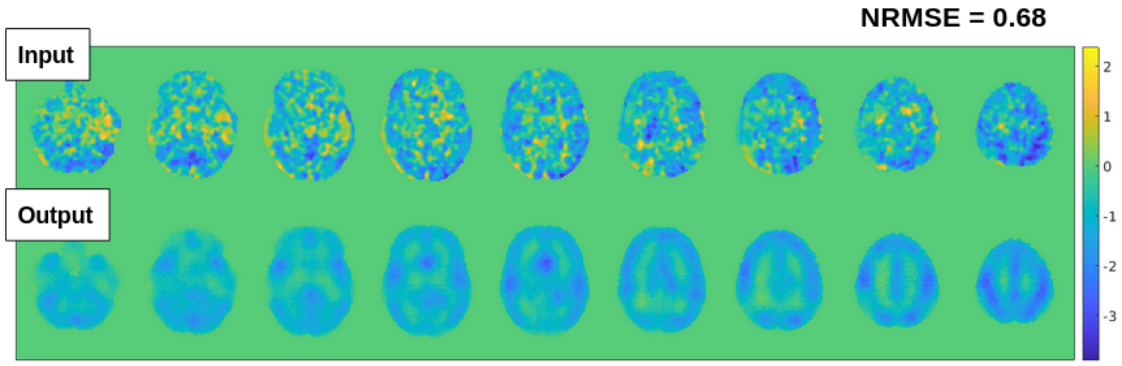

Figure 5.5: Spatial patterns from the volumetric VAE input (top row) and decoder output (bottom row).

5.3 Results

This work implemented a VAE model that aims to compress volumetric fMRI data to a 256-D latent space and then decode latent representations back to volumetric fMRI space. Figure 5.5 shows that the 3D VAE appears to reconstruct spatial patterns in a similar manner to the surface-based (2D) model, where it effectively results in output that is a smoothed version of the input, corresponding to smoothing of around 6mm FWHM. The NRMSE between input and decoder output for spatial patterns was approximately 0.68. The VAE model also preserves temporal patterns between average timecourses from the gray matter for both the input and decoder output. Figure 5.6 demonstrates good alignment, with a correlation of approximately 0.8.

To investigate whether the 3D VAE model is able to encode low-dimensional representations of fMRI data and synthesize fMRI patterns from this latent space, we analyzed clustered latent variables as well as decoded samples from the prior distribution using the trained model. Figure 5.7 shows the results from temporally k-means clustered latent variables. Visual inspection may indicate that brain networks are reflected in the resultant clusters, but further analysis is needed. Figures 5.8-5.15 show the comparisons of synthesized and measured fMRI temporal ICA maps with

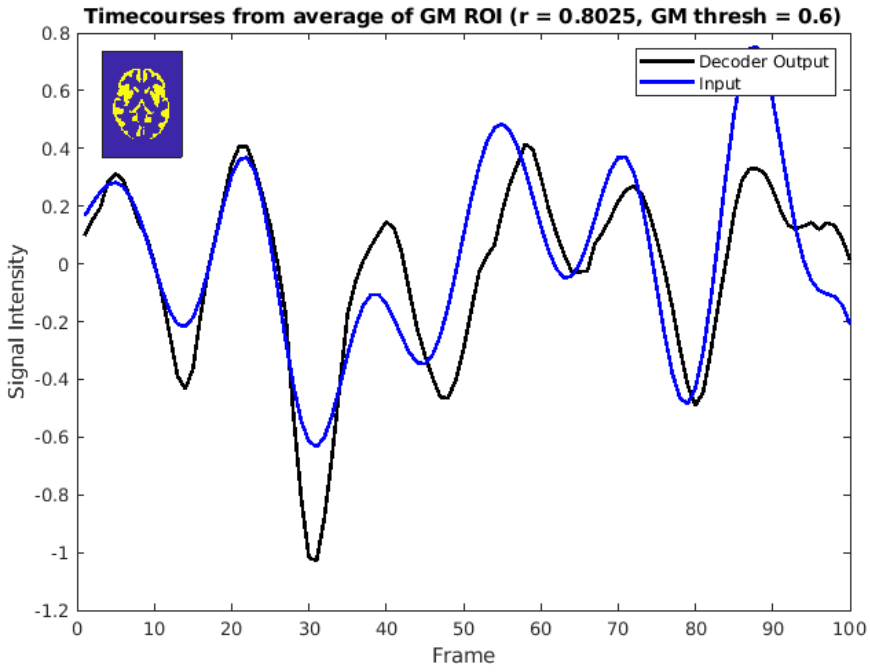

Figure 5.6: Timecourses from the average timecourses within the gray matter regions of the input and decoder output.

the Beckmann resting state networks. The highest corresponding ICA maps (Dice coefficient) are displayed here; however, visual inspection indicates that better correspondence between measured/synthesized and/or RSN may be achieved with ICA maps that do not yield the greatest Dice coefficient. For example, the visuo-spatial system is well represented in synthesized ICA maps (Figure 5.12), but not as well for measured ICA maps. However, the measured ICA map most highly corresponding to executive control (Figure 5.13) appears to align well with the visuo-spatial system regions.

5.4 Discussion

Here, we present a volumetric VAE model that learns low-dimensional representations of 3D fMRI data. The results demonstrate that the volumetric VAE model performs in a similar manner to the 2D surface-based model [101]. It successfully re-

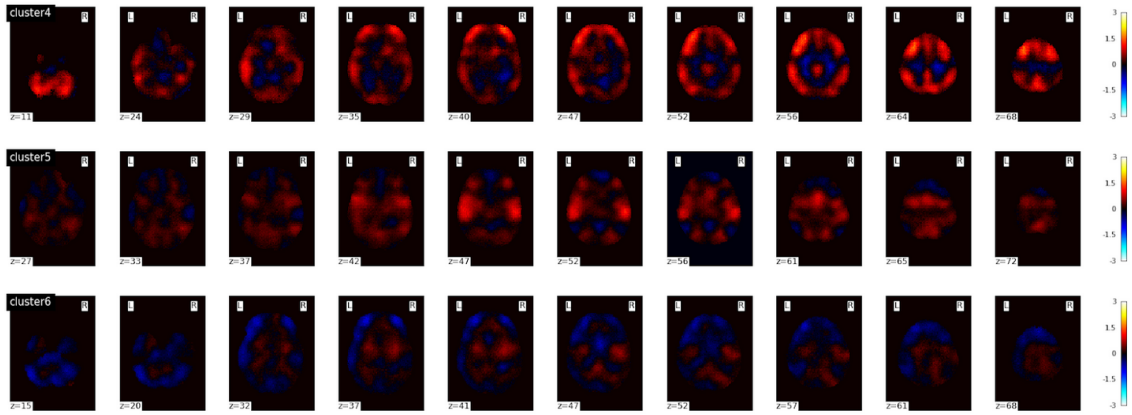

Figure 5.7: Decoded clustered latent representations for cluster 4, 5, 6.

constructs spatial and temporal patterns, and reveals network-like patterns in latent variable timecourses. The VAE model developed here provides a nonlinear modeling approach for volumetric fMRI data that may be advantageous for broader applications, such as those in the intersection of neuroscience and machine learning.

There are many possible future directions for this work. The synthesized fMRI may enable other areas of study, such as deep learning applications that require significant training data. The Dice coefficient analysis to identify potential network patterns in the synthesized and measured decoded data could be altered to more accurately align functional brain regions. Measures of spatial frequency or correlation may be well suited for this application [51]. Other measures of similarity, such as the Jaccard index, may also be informative [121].

Future work can examine integration of a volumetric VAE model into reconstruction and preprocessing pipelines to identify sources of neural activity in fMRI data. It is hypothesized that the 3D VAE model presented here will generalize to different data types, including task and other scan conditions as well as other subject populations. For example, the pre-trained surface-based model has successfully generalized to movie-watching fMRI without the need for retraining or fine-tuning the model [99]. This is expected to also hold true in the 3D case, but this remains for future

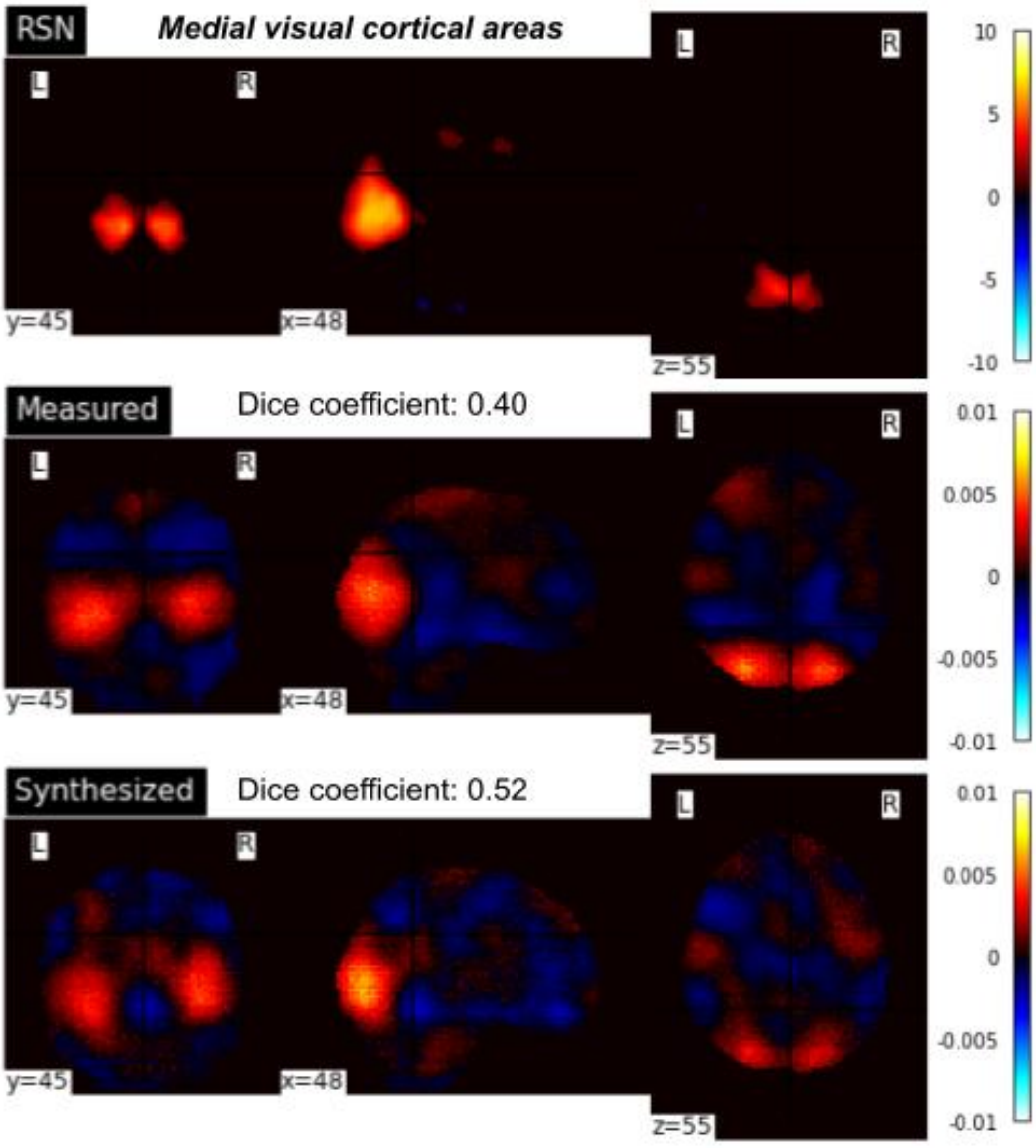

Figure 5.8: ICA maps for the medial visual cortical areas RSN (top) and the measured (middle) and synthesized (bottom) ICA maps with the highest corresponding Dice coefficient.

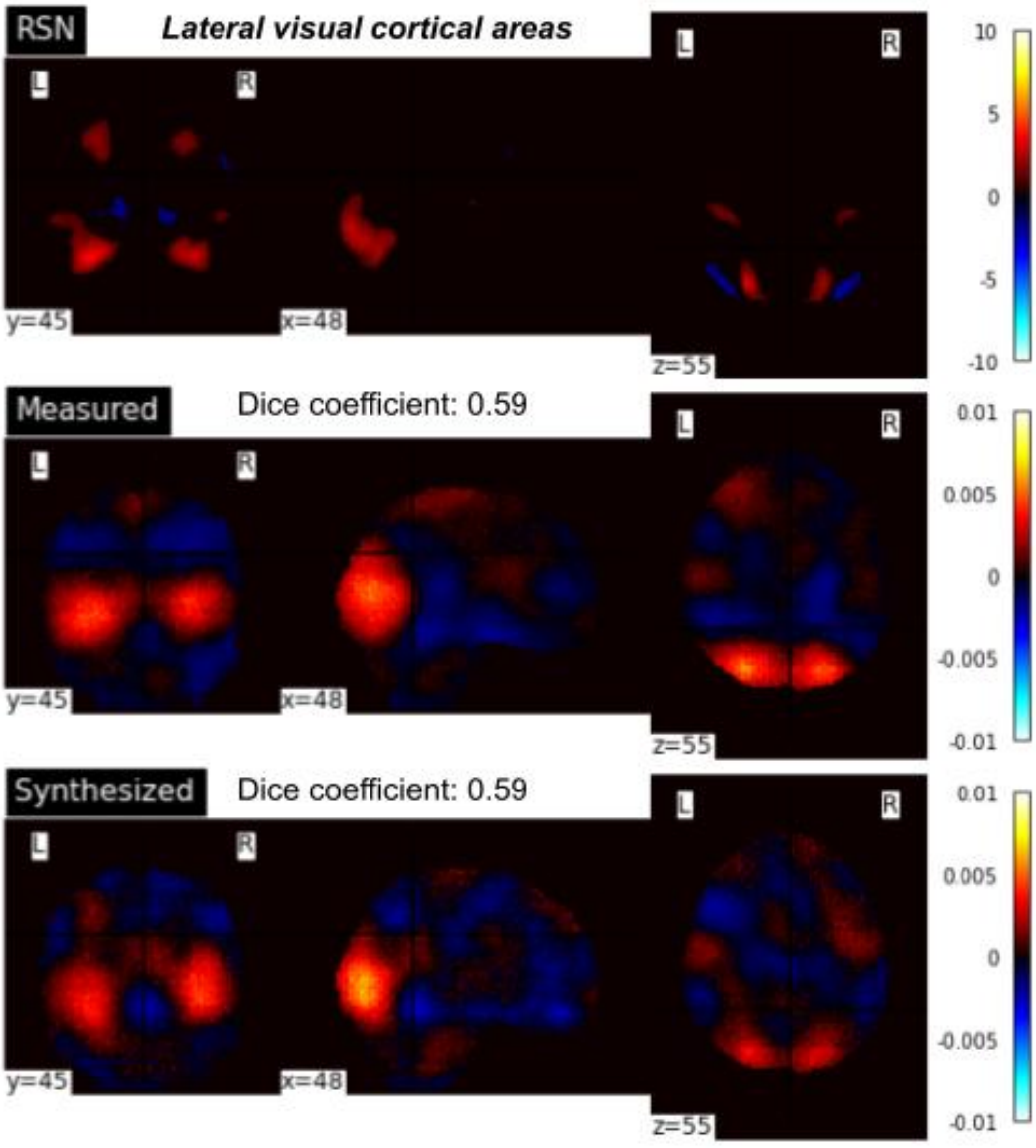

Figure 5.9: ICA maps for the lateral visual cortical areas RSN (top) and the measured (middle) and synthesized (bottom) ICA maps with the highest corresponding Dice coefficient.

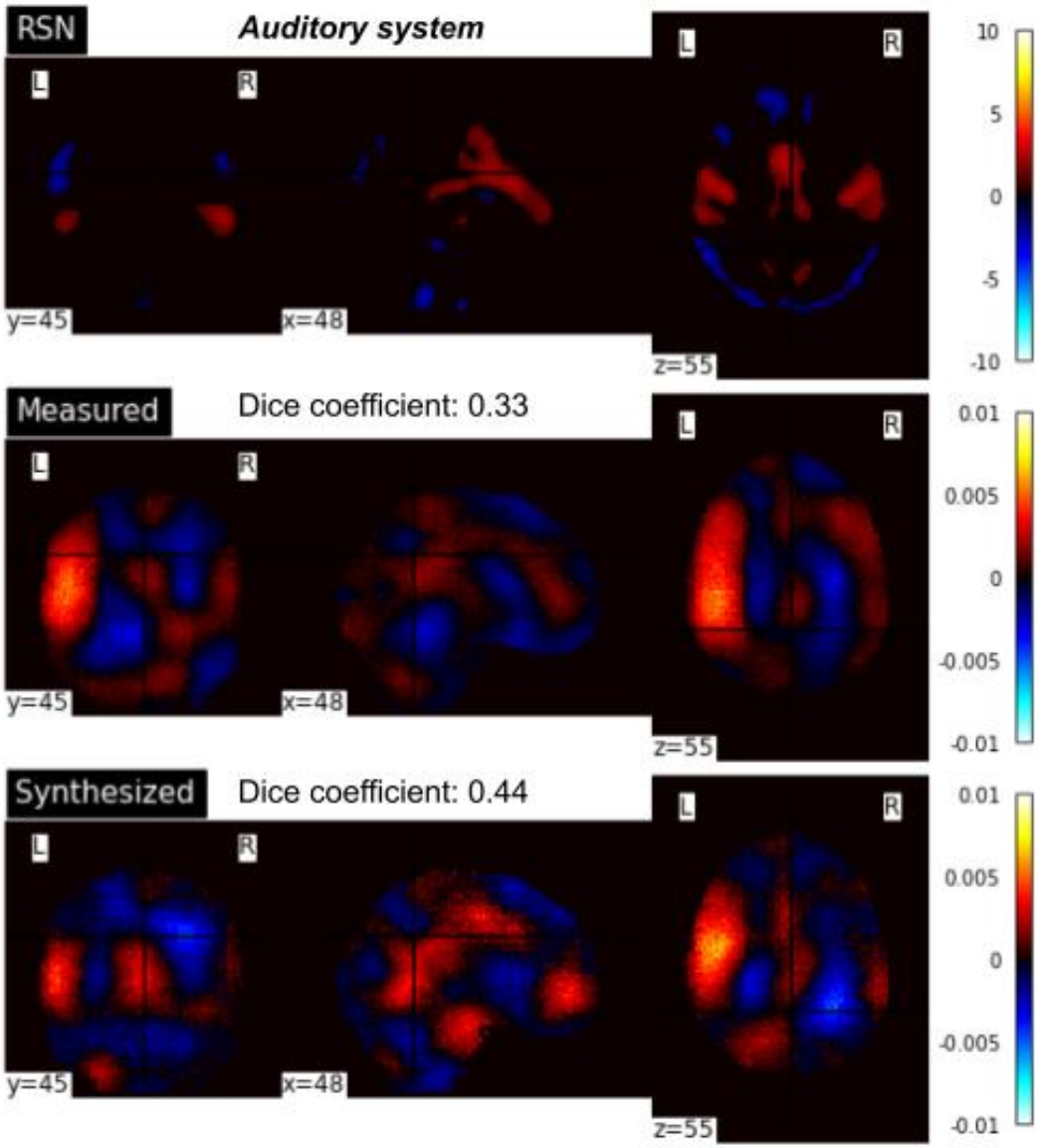

Figure 5.10: ICA maps for the auditory system RSN (top) and the measured (middle) and synthesized (bottom) ICA maps with the highest corresponding Dice coefficient.

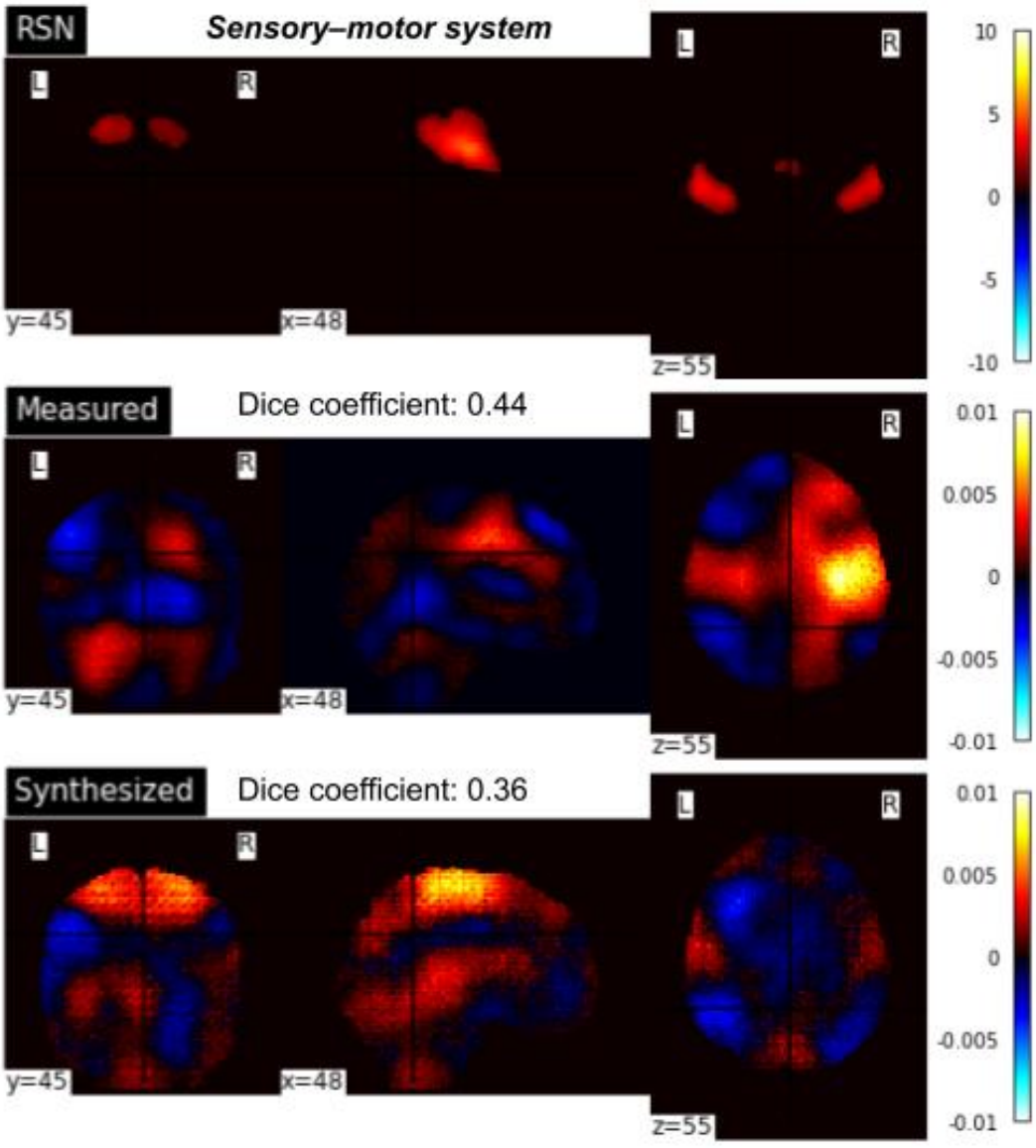

Figure 5.11: ICA maps for the sensory-motor system RSN (top) and the measured (middle) and synthesized (bottom) ICA maps with the highest corresponding Dice coefficient.

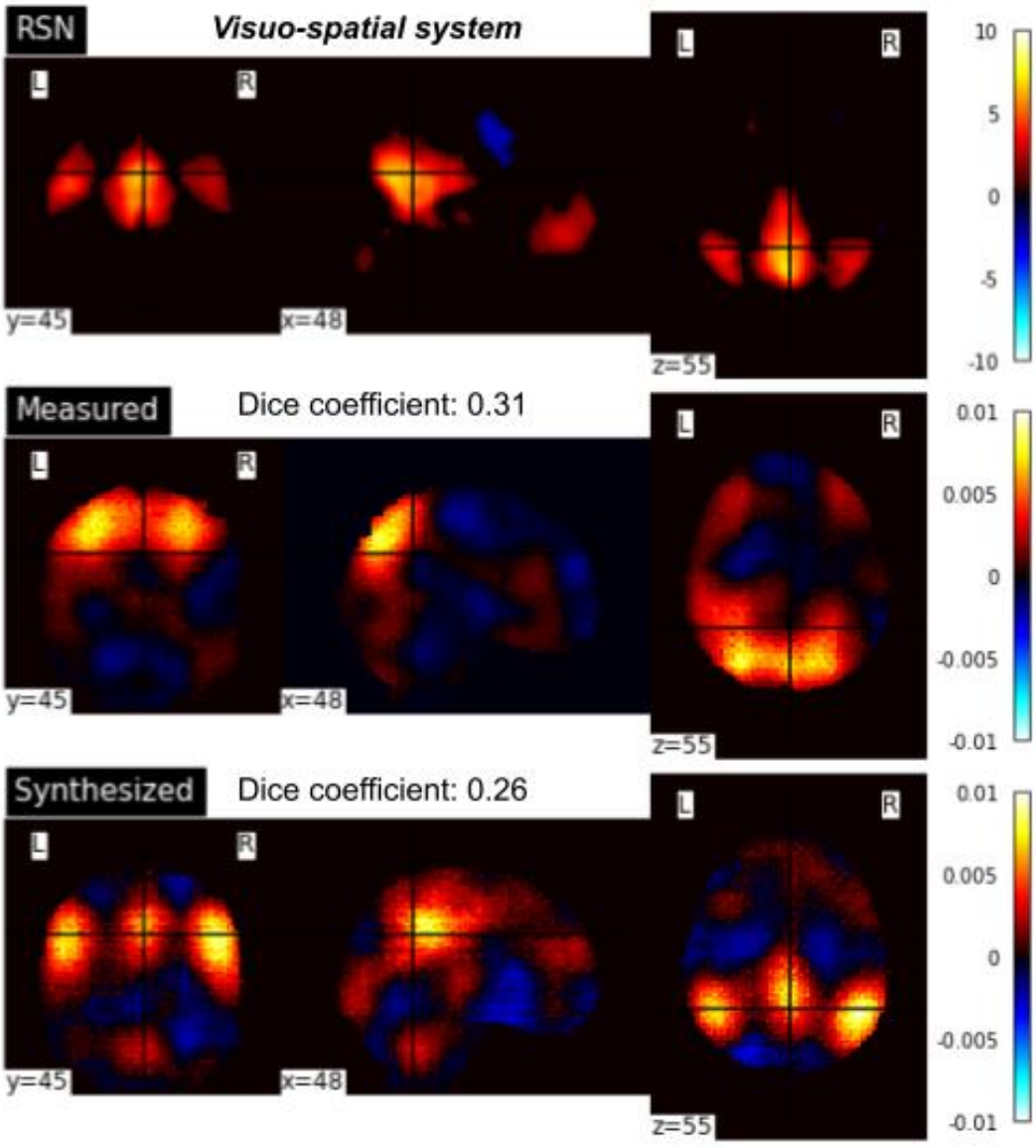

Figure 5.12: ICA maps for the visuo-spatial system RSN (top) and the measured (middle) and synthesized (bottom) ICA maps with the highest corresponding Dice coefficient.

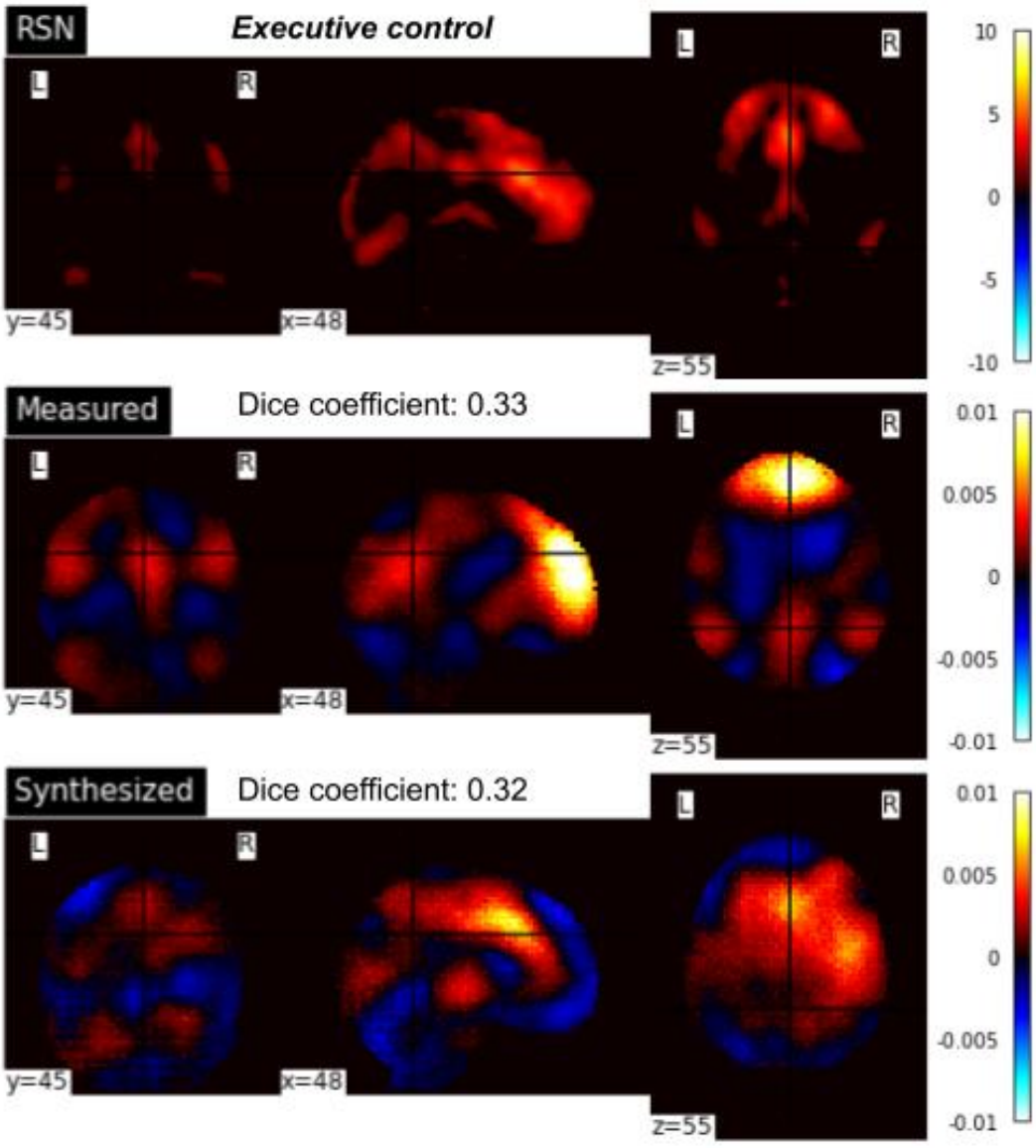

Figure 5.13: ICA maps for the executive control RSN (top) and the measured (middle) and synthesized (bottom) ICA maps with the highest corresponding Dice coefficient.

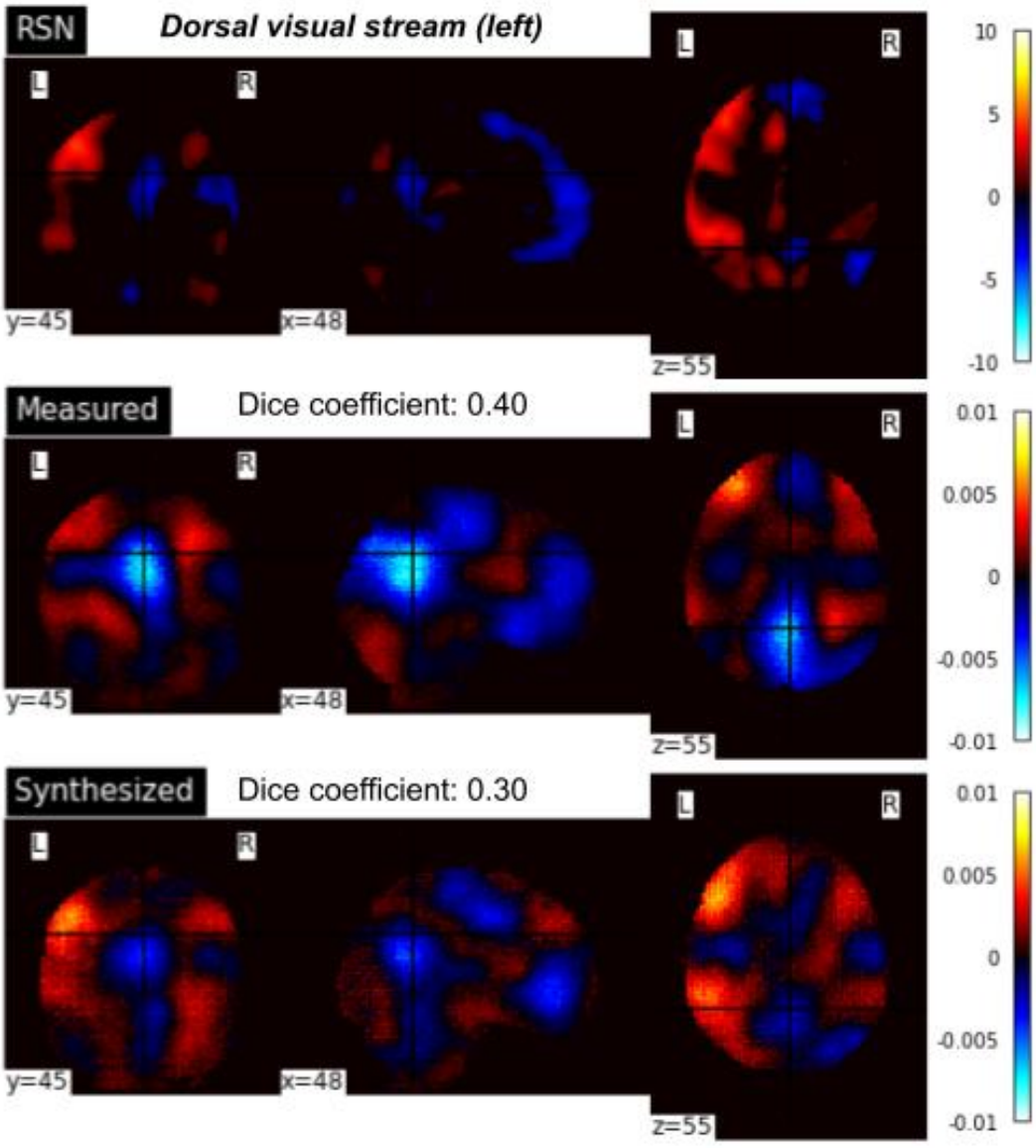

Figure 5.14: ICA maps for the dorsal visual stream (left) RSN (top) and the measured (middle) and synthesized (bottom) ICA maps with the highest corresponding Dice coefficient.

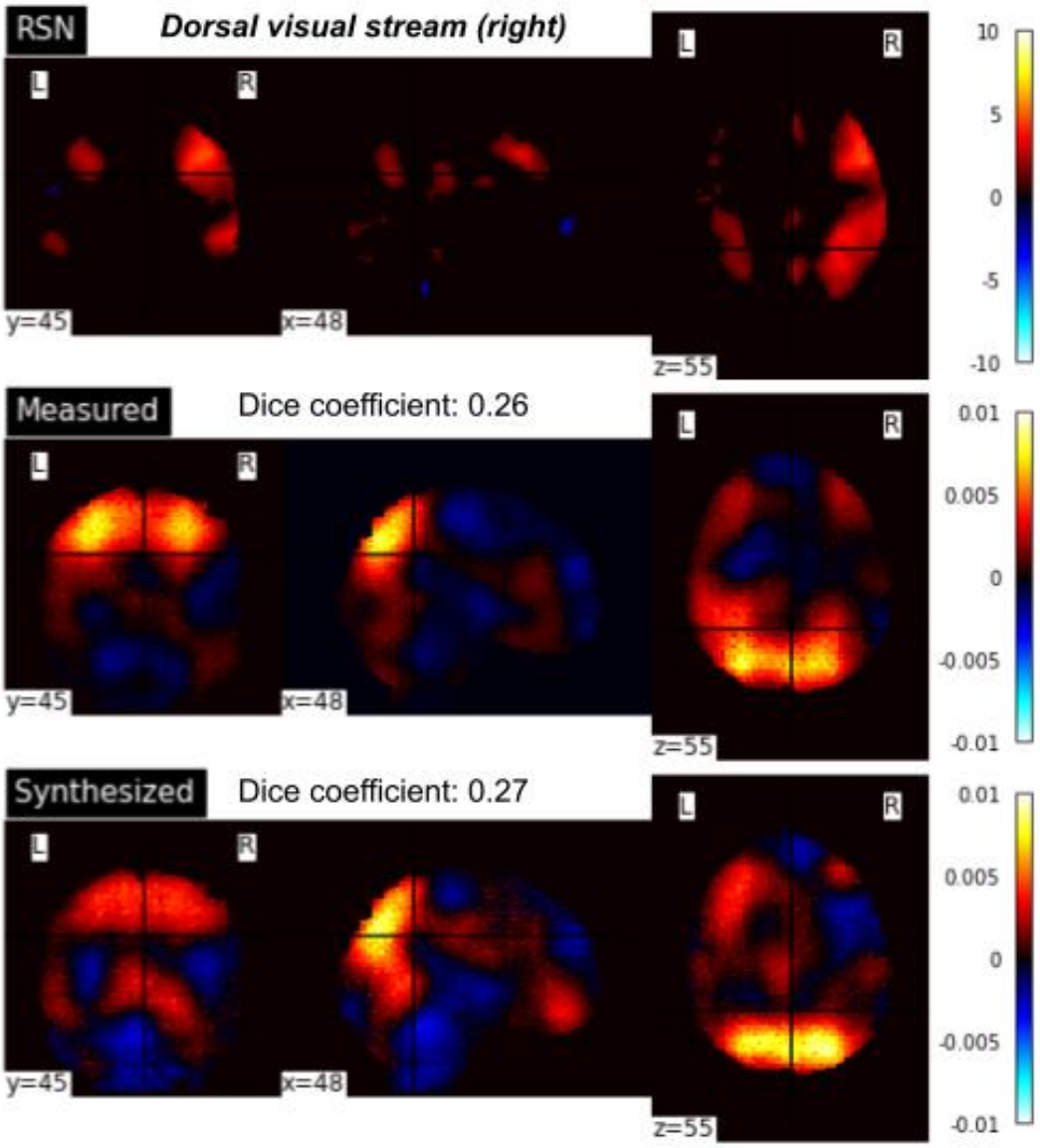

Figure 5.15: ICA maps for the dorsal visual stream (right) RSN (top) and the measured (middle) and synthesized (bottom) ICA maps with the highest corresponding Dice coefficient.

investigation.

The VAE model used in this work consists solely of spatial relationships; it treats each time point independently. The combination of a self-attention mechanism with the VAE model is promising for capturing long-range temporal relationships in the fMRI data. This transformer could be implemented in the encoder portion of the model to remember temporal dynamics, similar to functional connectivity. Other deep learning approaches to examine temporal dynamics in fMRI data would also be interesting to investigate.

In future work, we plan to apply the volumetric model to rsfMRI from subjects with dementia of the Alzheimer's type. We hypothesize that this extension of the VAE model will generalize to data from subjects along the continuum of Alzheimer's disease, as in Chapter IV. Additionally, identifying low dimensional features in the VAE latent space associated with certain aspects of healthy or disordered brain activity (e.g., memory, cognition, attention, etc.) could provide pivotal access to extract meaningful activity from measured fMRI or other brain monitoring data. This implicates many further areas of study, including other clinical and cognitive science applications across disease populations and brain imaging modalities. As mentioned in Chapter IV, the VAE model can be readily extended to task-based fMRI, through using the rs-fMRI pre-trained VAE model or by re-training on task data. Task-based data may offer unique insights in clinical applications due to its ability to attenuate or strengthen network activity in irrelevant or relevant brain regions.

5.5 Conclusion

In summary, the volumetric VAE model provides information from subcortical regions and captures nonlinear relationships neglected in other analysis approaches. This holds promise for clinical applications, especially in cases of dementia, which can arise from many potential causes. The high rate of comorbidities seen in dementia

and other neurological and psychiatric diseases emphasizes the need for analysis approaches that can be applied transdiagnostically to disentangle and distinguish each cause. Advanced modeling approaches such as the VAE are expected to be particularly influential in these future areas of research.

CHAPTER VI

Future Work

In the previous chapters, we have proposed novel combinations of modeling and neuroimaging data from subjects along the spectrum of Alzheimer's disease. However, no one data modality captures the full picture of a neurological or psychiatric disease and combining multiple modalities can fortify and augment our findings. Several options for future work integrating multimodal data in the context of AD are discussed in the following chapter. The modeling techniques developed in this dissertation may also provide utility in identifying specific brain regions to target for potential therapeutic interventions such as neurostimulation. Overall, much remains to be learned about Alzheimer's disease; this section discusses a few potential areas in which to extend the work in this dissertation.

6.1 Combinations of Multimodal Data

One promising extension of this work is to combine multimodal data in the aforementioned prediction and modeling approaches. This has already been investigated in studies of classification related to Alzheimer's disease, such as combinations of structural MRI and PET [182], or structural MRI and DTI [117]. Multimodal predictors have also proved useful in regression capacities; for example, a combination of structural MRI, FDG-PET, and cerebrospinal fluid (CSF) improved performance

over models using individual modalities [181]. Predictive modeling and deep learning techniques can utilize multimodal data through simple concatenation in the input/predictors or through a combined modeling approach such as the multiple-kernel method.

One avenue to pursue multimodality is through DTI-based measures. White matter microstructures, as measured by DTI, undergo significant changes through a lifespan [113]. Changes in DTI measures are also apparent in disease states, including Alzheimer's disease [78, 79, 150]. A more advanced version of DTI that may provide unique information on tissue microstructures is neurite orientation dispersion and density imaging (NODDI). NODDI has shown promise in representing aspects of pathology that occur in AD [26, 172]. Other data types include MRI-based measures of myelin water fraction that can provide insights about demyelination and white matter changes that occur in neurodegenerative conditions such as AD [118]. As evidenced through existing studies on the role of APOE and other gene status in Alzheimer's disease, there is increasing interest in the genetic component of AD. There is also growing opportunity to use imaging measures in combination with genetics data, such as genome-wide association studies (GWAS).

Other future studies could investigate combinations of potential therapeutics with predictive modeling to model longitudinal outcomes. This approach also has the option for multimodal data combinations. The search for therapeutics for AD has been ongoing for decades. Existing therapeutic medications (i.e., aducunab) are limited to clearing Alzheimer's disease proteins but have negligible effects on overall functioning, especially when administered in advanced disease stages.

6.2 Targeting for Neurostimulation and Neuromodulation

Neurostimulation and neuromodulation techniques are direct and noninvasive and may provide utility in the characterization and treatment of Alzheimer's disease.

However, further study is needed to evaluate the proper dosage application and safety of these approaches. Transcranial Direct Current Stimulation (TCDS) uses currents from an anode to target and stimulate specific areas of the brain, and a cathode receives current out of the brain. This approach has been shown to improve memory performance in subjects with DAT [46], although further studies are needed. Trancranial magnetic stimulation (TMS) uses an electric field generated in copper coils to discharge the resulting magnetic field into the brain. This has been found to induce stimulation of motor and visual cortex brain activity, and has been successfully used to reduce depression symptoms [59, 106]. Future work could study the effects of such techniques on brain networks using the modeling approaches presented in this dissertation with the ultimate goal of identifying the optimal brain regions to target.

TMS could be promising for characterization of Alzheimer's disease states and the associated changes in neuroplasticity or excitability [96] and potentially treatment. Existing studies have found improved cognitive function with TMS in subjects with MCI or DAT [28, 140]. Some studies also implement cognitive training. Working memory training in older adults has been shown to improve plasticity [86]; future work could examine predictive modeling effects of different types of cognitive and memory training in subjects along the continuum of AD. Predictive modeling before and after training may be able to illuminate altered brain networks or predict the best brain regions in which to apply TMS.

6.3 Conclusion

There are many ongoing advancements in neuroimaging, AD therapeutics, deep learning and predictive modeling. Novel combinations of image/data acquisition and analysis have enormous potential to increase understanding, detection, prediction, and treatment of neurological and psychiatric disorders such as AD. Several research areas of interest pertain to the main work and future directions discussed in this

dissertation: (1) relationships between multimodal data and metrics of behavior relevant to Alzheimer's disease, (2) differences in brain-behavior relationships for subjects with MCI or DAT after completing cognitive rehabilitation tasks and/or undergoing non-invasive brain stimulation, and (3) representation learning of multimodal or longitudinal data. Ultimately, studying brain changes and modeling approaches applied to AD remains an interesting yet challenging problem.

APPENDICES

APPENDIX A

Additional Connectome Predictive Modeling Results

A.1 Connectome Predictive Modeling (CPM) Figures

In addition to the PLS-BETA results discussed in Chapter II, analogous figures for the CPM results are included in this Appendix. As described before, significant model connections were visualized with the Yale BioImage Suite Connectivity Viewer (bioimagesuiteweb.github.io/webapp/), to evaluate node connections and display important nodes (defined by degree). The MNI coordinates and node labels for the top five highest degree nodes are tabulated in Table 2.5. Further discussion of these results is included in Chapter II.

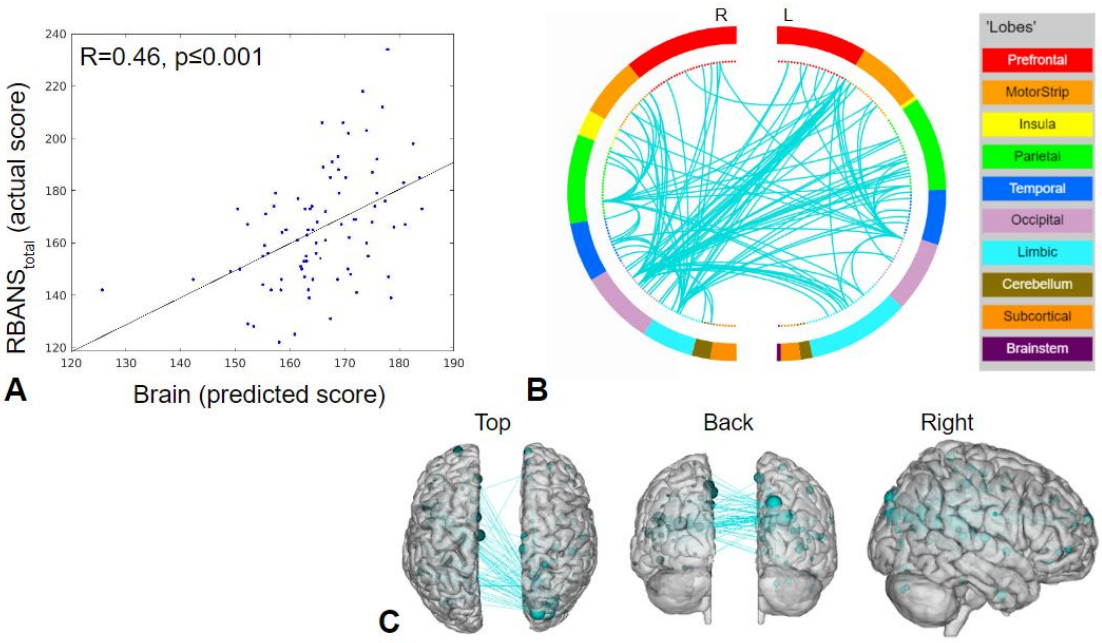

Figure A.1: RBANS$_{\text{total}}$ CPM results for face-name task data (negative edges). A) Plot of predicted versus actual RBANS$_{\text{total}}$ values. B) Circle plot of significant connections between brain areas (using node degree threshold of 18). C) Glass brain plot of significant nodes and connections.

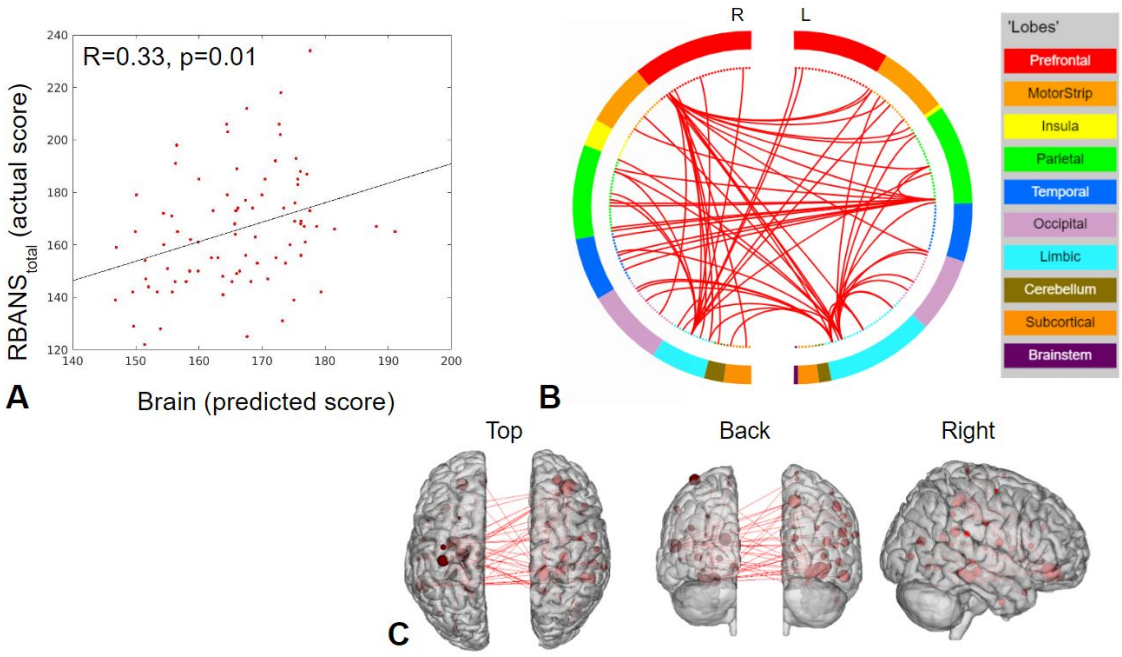

Figure A.2: RBANS$_{\text{total}}$ CPM results for object-location task data (positive edges). A) Plot of predicted versus actual RBANS$_{\text{total}}$ values. B) Circle plot of significant connections between brain areas (using node degree threshold of 12). C) Glass brain plot of significant nodes and connections.

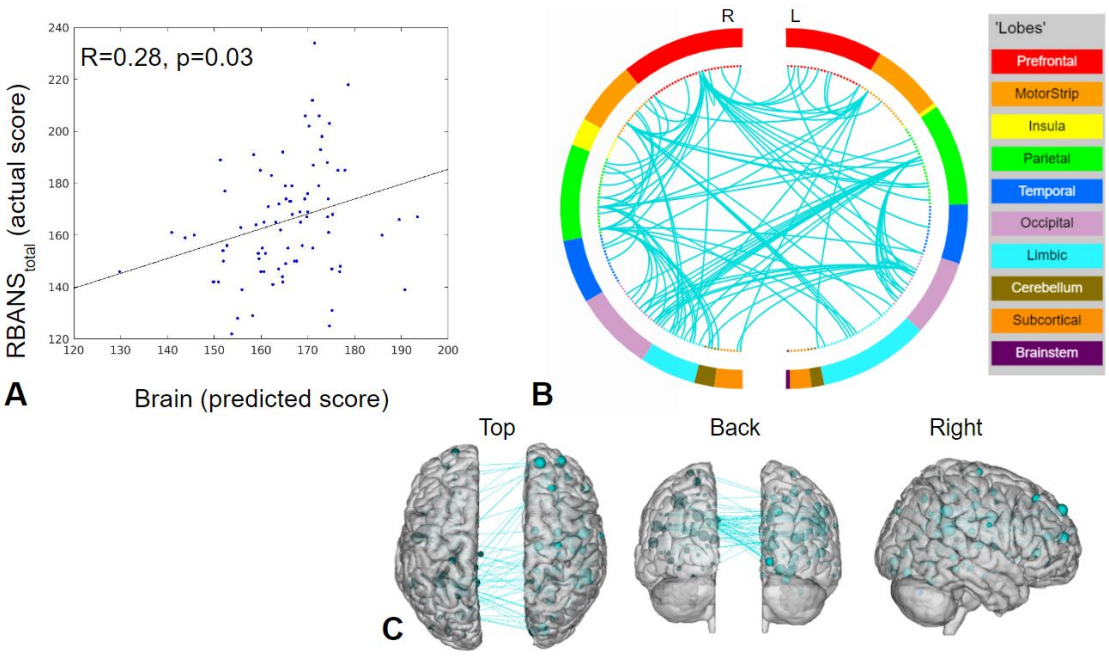

Figure A.3: RBANS$_{\text{total}}$ CPM results for object-location task data (negative edges). A) Plot of predicted versus actual RBANS$_{\text{total}}$ values. B) Circle plot of significant connections between brain areas (using node degree threshold of 11). C) Glass brain plot of significant nodes and connections.

APPENDIX B

Guide to the Great Lakes High Performance Compute Cluster for fMRI Preprocessing

B.1 High Performance Computing at University of Michigan

The Great Lakes High Performance Compute (HPC) cluster at University of Michigan (UM) is incredibly valuable in handling large datasets, such as those encountered with fMRI. In addition to excellent documentation provided by the University of Michigan Advanced Research Computing division of Information and Technology Services (https://arc.umich.edu/greatlakes/), resources are plentiful on various other sites as many of the required procedures and codes are standard across HPC clusters. For example, Great Lakes uses widespread Slurm scheduling (https://slurm.schedmd.com/), and batch scripting is common in many applications. This Appendix aims to provide a how-to guide for researchers desiring to use a HPC cluster for preprocessing of fMRI data. It is impossible to summarize all the potential variations of this approach; readers can modify portions of this guide for their own application and software setup as needed. The full code is published (https://doi.org/10.5281/zenodo.7047041) [126]. This work was completed via

Linux; hence, some of the following directions will need to be adjusted for those on Windows.

B.1.1 Accessing Great Lakes

There are two important components needed to use Great Lakes: a login account (which provides access to the cluster) and a Slurm account (which pays for cluster usage). Using your login account via login nodes does not generally incur charges for tasks, such as editing job scripts, compiling software, or transferring data. Job submission via a Slurm account does incur charges, and current rates are available on the Great Lakes webpage. Once you have a Great Lakes login account, you can access it on campus or via UM VPN with your Level-1 password using `ssh`. Next, it is important to determine which Great Lakes Slurm account should be associated with your usage. If you do not have funding of your own, your college or department (e.g., Michigan Engineering) at UM may provide a shared Slurm account for small projects, but large-scale research or courses should have dedicated Slurm accounts. At the time of writing, UM was providing a 'base allocation' to all faculty and some post-doctoral fellows. Furthermore, UM's Rackham Graduate School or national funding agencies (e.g., NSF) may be able to provide funding that can be used to pay for usage on Great Lakes. Once connected, you can navigate to the Slurm account `/scratch/` directory that provides large amounts of storage to work on your own data and scripts.

On the Great Lakes server, you can use the command `my_accounts` or `id \$USER` to obtain more information about Slurm accounts through which you have access to compute resources. If you don't have access, you'll need the Slurm account owner to request for you to have access.

B.1.2 Data transfer to Great Lakes

When working with many subjects or many files of data, it is helpful to set up SSH keys from the local server containing the data to Great Lakes to avoid requiring authentication for each file transfer. On Linux and Mac, keys are located in files; in Windows, they are stored in a registry entry. Those on Windows can refer to the following for help generating an SSH key: https://www.ssh.com/academy/ssh/putty/windows/puttygen. On the local server, obtain the existing key file and copy the contents of the public key to the Great Lakes key file. On Great Lakes, make this key file one of your authorized keys: `cat /path/to/local/key/file/id_rsa.pub >> ~/.ssh/authorized_keys`. On your local server, you can now easily copy data to Great Lakes via a transfer node (`greatlakes-xfer.arc-ts.umich.edu`) using `scp` or `rsync`. Note that the `--files-from` flag for `rsync` can be a helpful alternative for this last step as well by allowing you to copy directories or files listed in a text file. Note that fMRI data should be in BIDS format for fMRIPrep.

B.1.3 Running fMRIPrep in Batches

Preprocessing with fMRIPrep (https://fmriprep.org/en/stable/) can be a long process, especially if processing a large number of subjects and/or including the FreeSurfer (https://surfer.nmr.mgh.harvard.edu/) components. With FreeSurfer, a single subject's fMRIPrep processing can range from 8-13 hours. Great Lakes can help with this by allowing you to submit many jobs at once that can run concurrently. Here, this is accomplished using a list of subjects and submitting each subject's processing as a separate job, which will then be queued in the order submitted. This way, each subject will run separately and, if there is an error, it won't disrupt the processing for other subjects. It is highly recommended to test your job scripts with a handful of subjects first before submitting all of them.

B.1.3.1 Creating a batch file for fMRIPrep

First, set up a batch file (e.g., `fmriprep_job_script.sbat`) that runs your process (e.g., fMRIPrep) for a single subject and copies the output files to the desired server. At this point, it is helpful to copy the SSH key from Great Lakes to the server where you want output files to go. This eliminates the need for authentication when each job script copies output files from Great Lakes to the local server.

The batch file is comprised of directives, loading modules, and user scripts. The directives first specify that we will use the bash shell and then contain information for the Slurm scheduler about how to allocate resources and other specifications for each job. Below is an example of the directives for an fMRIPrep job.

In the next component of the batch file, the required software can be loaded. The Great Lakes HPC uses Singularity containers for fMRIPrep, so that is all that is needed. We can also specify to print information about the job to the output file, which is recommended for debugging.

Finally, any job-specific code can be added to the batch file. For fMRIPrep, this most likely includes creating directories, pointing to software licenses, the actual call to fMRIPrep, copying files to the local server (if desired), and removing unneeded intermediate files. For the call to fMRIPrep, many options are available and some flags are self-explanatory. The `--cifti-output` fMRIPrep flag is needed for output data in Human Connectome Project (HCP) grayordinates. In this work, fMRIPrep 20.2.5 CIFTI outputs (91k) are the chosen dimensionality of CIFTI outputs to match HCP 1200 CIFTI data. The flag `--output-spaces` sets the standard spaces to which we would like to map the fMRI data. Further documentation of fMRIPrep is available here: https://fmriprep.org/en/stable/. It is recommended to test the job script with a small number of subjects for debugging purposes.

B.1.3.2 Creating a wrapper submission script

Next, create a wrapper bash script (e.g., `submit_fmriprep_subject.sh`) that copies the batch script and replaces the subject ID using a text file that contains the list of subject IDs for which you wish to run fMRIPrep. Tips for creating this text file will be discussed in Appendix B.1.3.3. For each subject in the text file, this bash script will submit a separate job via `sbatch` using the batch file renamed for each subject. This is useful to pinpoint any subject-specific errors in the output logs.

B.1.3.3 Generating a list of subject files

The following codes can be run from the data directory to append subject IDs to the correct text file. Note that you can select a subset or all of the subjects by modifying these commands.

```
for d in ./*; do [[ -d "$d" ]] && echo "${d##./}" >> sublist.txt; done
# copy desired subject IDs (edit as needed)
head -5 sublist.txt > my_subjects.txt
tail -n 107 sublist.txt > my_subjects.txt
```

B.1.3.4 Submitting, Monitoring, and Quality Checks for fMRIPrep jobs

Finally, you can run the wrapper function (`sh submit_fmriprep_subject.sh`) to submit your jobs. Again, it is highly recommended to test this with a subset of subjects to debug any issues before submitting them all.

After submitting a job, check on progress or cancel jobs with the following options:

```
# Check if jobs are queued
sq
# Check if jobs are running
sacct -u $USER | grep RUNNING
```

```
# Check if jobs are complete
sacct -u $USER | grep COMPLETE
# Cancel jobs
scancel [jobID]
```

After your fMRIPrep job is complete, you can perform QA checks using the fMRIPrep output HTML file. A useful demonstration for this is found in Andy's Brain Book: https://andysbrainbook.readthedocs.io/en/latest/OpenScience/OS/fMRIPrep_Demo_3_ExaminingPreprocData.html.

BIBLIOGRAPHY

[1] Alexandre Abraham, Fabian Pedregosa, Michael Eickenberg, Philippe Gervais, Andreas Mueller, Jean Kossaifi, Alexandre Gramfort, Bertrand Thirion, and Gael Varoquaux. Machine learning for neuroimaging with scikit-learn. *Frontiers in Neuroinformatics*, 8, 2014.

[2] Federica Agosta, Michela Pievani, Cristina Geroldi, Massimiliano Copetti, Giovanni B Frisoni, and Massimo Filippi. Resting state fmri in alzheimer's disease: beyond the default mode network. *Neurobiology of aging*, 33(8):1564–1578, 2012.

[3] Marilyn S Albert, Steven T DeKosky, Dennis Dickson, Bruno Dubois, Howard H Feldman, Nick C Fox, Anthony Gamst, David M Holtzman, William J Jagust, Ronald C Petersen, et al. The diagnosis of mild cognitive impairment due to alzheimer's disease: recommendations from the national institute on aging-alzheimer's association workgroups on diagnostic guidelines for alzheimer's disease. *Alzheimer's & dementia*, 7(3):270–279, 2011.

[4] Pedro Nascimento Alves, Chris Foulon, Vyacheslav Karolis, Danilo Bzdok, Daniel S Margulies, Emmanuelle Volle, and Michel Thiebaut de Schotten. An improved neuroanatomical model of the default-mode network reconciles previous neuroimaging and neuropathological findings. *Communications biology*, 2(1):1–14, 2019.

[5] Alfredo Ardila, Feggy Ostrosky-Solís, and Byron Bernal. Cognitive testing toward the future: The example of semantic verbal fluency (animals). *International Journal of Psychology*, 41(5):324–332, 2006.

[6] John Ashburner. Spm: a history. *Neuroimage*, 62(2):791–800, 2012.

[7] B.B. Avants, C.L. Epstein, M. Grossman, and J.C. Gee. Symmetric diffeomorphic image registration with cross-correlation: Evaluating automated labeling of elderly and neurodegenerative brain. *Medical Image Analysis*, 12(1):26–41, 2008.

[8] Feng Bai, David R Watson, Yongmei Shi, Yi Wang, Chunxian Yue, Di Wu, Yonggui Yuan, and Zhijun Zhang. Specifically progressive deficits of brain functional marker in amnestic type mild cognitive impairment. *PloS one*, 6(9):e24271, 2011.

[9] Feng Bai, Chunming Xie, David R Watson, Yongmei Shi, Yonggui Yuan, Yi Wang, Chunxian Yue, Yuhuan Teng, Di Wu, and Zhijun Zhang. Aberrant hippocampal subregion networks associated with the classifications of amci subjects: a longitudinal resting-state study. *PloS one*, 6(12):e29288, 2011.

[10] Silvia Basaia, Federica Agosta, Luca Wagner, Elisa Canu, Giuseppe Magnani, Roberto Santangelo, Massimo Filippi, Alzheimer's Disease Neuroimaging Initiative, et al. Automated classification of alzheimer's disease and mild cognitive impairment using a single mri and deep neural networks. *NeuroImage: Clinical*, 21:101645, 2019.

[11] Peter J Basser, James Mattiello, and Denis LeBihan. Estimation of the effective self-diffusion tensor from the nmr spin echo. *Journal of Magnetic Resonance, Series B*, 103(3):247–254, 1994.

[12] Peter J Basser, James Mattiello, and Denis LeBihan. Mr diffusion tensor spectroscopy and imaging. *Biophysical journal*, 66(1):259–267, 1994.

[13] Christian F Beckmann, Marilena DeLuca, Joseph T Devlin, and Stephen M Smith. Investigations into resting-state connectivity using independent component analysis. *Philosophical Transactions of the Royal Society B: Biological Sciences*, 360(1457):1001–1013, 2005.

[14] Christian F Beckmann and Stephen M Smith. Probabilistic independent component analysis for functional magnetic resonance imaging. *IEEE transactions on medical imaging*, 23(2):137–152, 2004.

[15] Yashar Behzadi, Khaled Restom, Joy Liau, and Thomas T. Liu. A component based noise correction method (CompCor) for BOLD and perfusion based fmri. *NeuroImage*, 37(1):90–101, 2007.

[16] Céline Bellenguez, Fahri Küçükali, Iris E Jansen, Luca Kleineidam, Sonia Moreno-Grau, Najaf Amin, Adam C Naj, Rafael Campos-Martin, Benjamin Grenier-Boley, Victor Andrade, et al. New insights into the genetic etiology of alzheimer's disease and related dementias. *Nature genetics*, 54(4):412–436, 2022.

[17] Marije R Benedictus, Annebet E Leeuwis, Maja AA Binnewijzend, Joost Kuijer, Philip Scheltens, Frederik Barkhof, Wiesje M van der Flier, and Niels D Prins. Lower cerebral blood flow is associated with faster cognitive decline in alzheimer's disease. *European radiology*, 27(3):1169–1175, 2017.

[18] Maja AA Binnewijzend, Menno M Schoonheim, Ernesto Sanz-Arigita, Alle Meije Wink, Wiesje M van der Flier, Nelleke Tolboom, Sofie M Adriaanse, Jessica S Damoiseaux, Philip Scheltens, Bart NM van Berckel, et al. Resting-state fmri changes in alzheimer's disease and mild cognitive impairment. *Neurobiology of aging*, 33(9):2018–2028, 2012.

[19] Bharat Biswal, F Zerrin Yetkin, Victor M Haughton, and James S Hyde. Functional connectivity in the motor cortex of resting human brain using echo-planar mri. *Magnetic resonance in medicine*, 34(4):537–541, 1995.

[20] Robyn L Bluhm, Jodi Miller, Ruth A Lanius, Elizabeth A Osuch, Kristine Boksman, RWJ Neufeld, Jean Théberge, Betsy Schaefer, and Peter Williamson. Spontaneous low-frequency fluctuations in the bold signal in schizophrenic patients: anomalies in the default network. *Schizophrenia bulletin*, 33(4):1004–1012, 2007.

[21] Heiko Braak and Eva Braak. Staging of alzheimer's disease-related neurofibrillary changes. *Neurobiology of aging*, 16(3):271–278, 1995.

[22] Jason Brandt. The hopkins verbal learning test: Development of a new memory test with six equivalent forms. *The clinical neuropsychologist*, 5(2):125–142, 1991.

[23] Erica L Busch, Lukas Slipski, Ma Feilong, J Swaroop Guntupalli, Matteo Visconti di Oleggio Castello, Jeremy F Huckins, Samuel A Nastase, M Ida Gobbini, Tor D Wager, and James V Haxby. Hybrid hyperalignment: A single high-dimensional model of shared information embedded in cortical patterns of response and functional connectivity. *NeuroImage*, 233:117975, 2021.

[24] Linda L Chao, Shannon T Buckley, John Kornak, Norbert Schuff, Catherine Madison, Kristine Yaffe, Bruce L Miller, Joel H Kramer, and Michael W Weiner. Asl perfusion mri predicts cognitive decline and conversion from mci to dementia. *Alzheimer disease and associated disorders*, 24(1):19, 2010.

[25] Gang Chen, B Douglas Ward, Chunming Xie, Wenjun Li, Zhilin Wu, Jennifer L Jones, Malgorzata Franczak, Piero Antuono, and Shi-Jiang Li. Classification of alzheimer disease, mild cognitive impairment, and normal cognitive status with large-scale network analysis based on resting-state functional mr imaging. *Radiology*, 259(1):213, 2011.

[26] Niall Colgan, Bernard Siow, James M O'Callaghan, Ian F Harrison, Jack A Wells, Holly E Holmes, Ozama Ismail, S Richardson, Daniel C Alexander, Emily C Collins, et al. Application of neurite orientation dispersion and density imaging (noddi) to a tau pathology model of alzheimer's disease. *Neuroimage*, 125:739–744, 2016.

[27] Dietmar Cordes, Victor M Haughton, Konstantinos Arfanakis, Gary J Wendt, Patrick A Turski, Chad H Moritz, Michelle A Quigley, and M Elizabeth Meyerand. Mapping functionally related regions of brain with functional connectivity mr imaging. *American journal of neuroradiology*, 21(9):1636–1644, 2000.

[28] Maria Cotelli, Marco Calabria, Rosa Manenti, Sandra Rosini, Claudio Maioli, Orazio Zanetti, and Carlo Miniussi. Brain stimulation improves associative

memory in an individual with amnestic mild cognitive impairment. *Neurocase*, 18(3):217–223, 2012.

[29] Robert W. Cox and James S. Hyde. Software tools for analysis and visualization of fmri data. *NMR in Biomedicine*, 10(4-5):171–178, 1997.

[30] Suzanne Craft, John Newcomer, Stephen Kanne, Samuel Dagogo-Jack, Philip Cryer, Yvette Sheline, Joan Luby, Agbani Dagogo-Jack, and Amy Alderson. Memory improvement following induced hyperinsulinemia in alzheimer's disease. *Neurobiology of aging*, 17(1):123–130, 1996.

[31] Paul K Crane, Adam Carle, Laura E Gibbons, Philip Insel, R Scott Mackin, Alden Gross, Richard N Jones, Shubhabrata Mukherjee, S McKay Curtis, Danielle Harvey, et al. Development and assessment of a composite score for memory in the alzheimer's disease neuroimaging initiative (adni). *Brain imaging and behavior*, 6(4):502–516, 2012.

[32] Rémi Cuingnet, Emilie Gerardin, Jérôme Tessieras, Guillaume Auzias, Stéphane Lehéricy, Marie-Odile Habert, Marie Chupin, Habib Benali, Olivier Colliot, Alzheimer's Disease Neuroimaging Initiative, et al. Automatic classification of patients with alzheimer's disease from structural mri: a comparison of ten methods using the adni database. *neuroimage*, 56(2):766–781, 2011.

[33] Anders M. Dale, Bruce Fischl, and Martin I. Sereno. Cortical surface-based analysis: I. segmentation and surface reconstruction. *NeuroImage*, 9(2):179–194, 1999.

[34] Caroline Machado Dartora, Michel Koole, and Ana Maria Marques da Silva. Glucose metabolism changes in cerebellar tonsils as an early predictor of cognitive decline. *Alzheimer's & Dementia*, 17:e054007, 2021.

[35] Sander M Daselaar, Steven E Prince, and Roberto Cabeza. When less means more: deactivations during encoding that predict subsequent memory. *Neuroimage*, 23(3):921–927, 2004.

[36] MJ De Leon, A Convit, OT Wolf, CY Tarshish, S DeSanti, H Rusinek, W Tsui, E Kandil, AJ Scherer, A Roche, et al. Prediction of cognitive decline in normal elderly subjects with 2-[18f] fluoro-2-deoxy-d-glucose/positron-emission tomography (fdg/pet). *Proceedings of the National Academy of Sciences*, 98(19):10966–10971, 2001.

[37] Alexandra De Sitter, Martijn D Steenwijk, Aurélie Ruet, Adriaan Versteeg, Yaou Liu, Ronald A Van Schijndel, Petra JW Pouwels, Iris D Kilsdonk, Keith S Cover, Bob W Van Dijk, et al. Performance of five research-domain automated wm lesion segmentation methods in a multi-center ms study. *Neuroimage*, 163:106–114, 2017.

[38] Didem Sener Dede, Bunyamin Yavuz, Burcu Balam Yavuz, Mustafa Cankurtaran, Meltem Halil, Zekeriya Ulger, Eylem Sahin Cankurtaran, Kudret Aytemir, Giray Kabakci, and Servet Ariogul. Assessment of endothelial function in alzheimer's disease: is alzheimer's disease a vascular disease? *Journal of the American Geriatrics Society*, 55(10):1613–1617, 2007.

[39] Elise Demeter, Luis Hernandez-Garcia, Martin Sarter, and Cindy Lustig. Challenges to attention: a continuous arterial spin labeling (asl) study of the effects of distraction on sustained attention. *Neuroimage*, 54(2):1518–1529, 2011.

[40] Bradford C Dickerson and Reisa A Sperling. Functional abnormalities of the medial temporal lobe memory system in mild cognitive impairment and alzheimer's disease: insights from functional mri studies. *Neuropsychologia*, 46(6):1624–1635, 2008.

[41] Julien Dubois, Paola Galdi, Lynn K Paul, and Ralph Adolphs. A distributed brain network predicts general intelligence from resting-state human neuroimaging data. *Philosophical Transactions of the Royal Society B: Biological Sciences*, 373(1756):20170284, 2018.

[42] SB Dunnett and HC Fibiger. Role of forebrain cholinergic systems in learning and memory: relevance to the cognitive deficits of aging and alzheimer's dementia. *Progress in brain research*, 98:413–420, 1993.

[43] Oscar Esteban, Ross Blair, Christopher J. Markiewicz, Shoshana L. Berleant, Craig Moodie, Feilong Ma, Ayse Ilkay Isik, Asier Erramuzpe, Mathias Kent, James D. andGoncalves, Elizabeth DuPre, Kevin R. Sitek, Daniel E. P. Gomez, Daniel J. Lurie, Zhifang Ye, Russell A. Poldrack, and Krzysztof J. Gorgolewski. fmriprep. *Software*, 2018.

[44] Oscar Esteban, Christopher Markiewicz, Ross W Blair, Craig Moodie, Ayse Ilkay Isik, Asier Erramuzpe Aliaga, James Kent, Mathias Goncalves, Elizabeth DuPre, Madeleine Snyder, Hiroyuki Oya, Satrajit Ghosh, Jessey Wright, Joke Durnez, Russell Poldrack, and Krzysztof Jacek Gorgolewski. fMRIPrep: a robust preprocessing pipeline for functional MRI. *Nature Methods*, 2018.

[45] AC Evans, AL Janke, DL Collins, and S Baillet. Brain templates and atlases. *NeuroImage*, 62(2):911–922, 2012.

[46] Roberta Ferrucci, F Mameli, I Guidi, S Mrakic-Sposta, M Vergari, SEEA Marceglia, F Cogiamanian, S Barbieri, E Scarpini, and A Priori. Transcranial direct current stimulation improves recognition memory in alzheimer disease. *Neurology*, 71(7):493–498, 2008.

[47] Emily S Finn, Xilin Shen, Dustin Scheinost, Monica D Rosenberg, Jessica Huang, Marvin M Chun, Xenophon Papademetris, and R Todd Constable. Functional connectome fingerprinting: identifying individuals using patterns of brain connectivity. *Nature neuroscience*, 18(11):1664–1671, 2015.

[48] G. Flandin and K. J. Friston. Statistical parametric mapping (SPM). *Scholarpedia*, 3(4):6232, 2008. revision #129667.

[49] VS Fonov, AC Evans, RC McKinstry, CR Almli, and DL Collins. Unbiased nonlinear average age-appropriate brain templates from birth to adulthood. *NeuroImage*, 47, Supplement 1:S102, 2009.

[50] Michael D Fox, Randy L Buckner, Hesheng Liu, M Mallar Chakravarty, Andres M Lozano, and Alvaro Pascual-Leone. Resting-state networks link invasive and noninvasive brain stimulation across diverse psychiatric and neurological diseases. *Proceedings of the National Academy of Sciences*, 111(41):E4367–E4375, 2014.

[51] Nicolai Franzmeier, Jens Göttler, Timo Grimmer, Alexander Drzezga, Miguel A Áraque-Caballero, Lee Simon-Vermot, Alexander NW Taylor, Katharina Bürger, Cihan Catak, Daniel Janowitz, et al. Resting-state connectivity of the left frontal cortex to the default mode and dorsal attention network supports reserve in mild cognitive impairment. *Frontiers in aging neuroscience*, 9:264, 2017.

[52] Karl J Friston, Andrew P Holmes, Keith J Worsley, J-P Poline, Chris D Frith, and Richard SJ Frackowiak. Statistical parametric maps in functional imaging: a general linear approach. *Human brain mapping*, 2(4):189–210, 1994.

[53] Shachar Gal, Niv Tik, Michal Bernstein-Eliav, and Ido Tavor. Predicting individual traits from unperformed tasks. *NeuroImage*, 249:118920, 2022.

[54] Siyuan Gao, Abigail S Greene, R Todd Constable, and Dustin Scheinost. Combining multiple connectomes improves predictive modeling of phenotypic measures. *Neuroimage*, 201:116038, 2019.

[55] Hugh Garavan, Dan Kelley, Allyson Rosen, Steve M Rao, and Elliot A Stein. Practice-related functional activation changes in a working memory task. *Microscopy research and technique*, 51(1):54–63, 2000.

[56] C Gaser. Partial volume segmentation with adaptive maximum a posteriori (map) approach. *NeuroImage*, (47):S121, 2009.

[57] Eloy Geenjaar, Amrit Kashyap, Noah Lewis, Robyn Miller, and Vince Calhoun. Spatio-temporally separable non-linear latent factor learning: an application to somatomotor cortex fmri data. *arXiv preprint arXiv:2205.13640*, 2022.

[58] Eloy Geenjaar, Tonya White, and Vince Calhoun. Variational voxelwise rs-fmri representation learning: Evaluation of sex, age, and neuropsychiatric signatures. In *2021 IEEE International Conference on Bioinformatics and Biomedicine (BIBM)*, pages 1733–1740. IEEE, 2021.

[59] Mark S George, Ziad Nahas, Monica Molloy, Andrew M Speer, Nicholas C Oliver, Xing-Bao Li, George W Arana, S Craig Risch, and James C Ballenger. A controlled trial of daily left prefrontal cortex tms for treating depression. *Biological psychiatry*, 48(10):962–970, 2000.

[60] Laura E Gibbons, Adam C Carle, R Scott Mackin, Danielle Harvey, Shubhabrata Mukherjee, Philip Insel, S McKay Curtis, Dan Mungas, and Paul K Crane. A composite score for executive functioning, validated in alzheimer's disease neuroimaging initiative (adni) participants with baseline mild cognitive impairment. *Brain imaging and behavior*, 6(4):517–527, 2012.

[61] Ariela Gigi, Reuven Babai, Avichen Penker, Talma Hendler, and Amos D Korczyn. Prefrontal compensatory mechanism may enable normal semantic memory performance in mild cognitive impairment (mci). *Journal of Neuroimaging*, 20(2):163–168, 2010.

[62] Matthew F. Glasser, Stamatios N. Sotiropoulos, J. Anthony Wilson, Timothy S. Coalson, Bruce Fischl, Jesper L. Andersson, Junqian Xu, Saad Jbabdi, Matthew Webster, Jonathan R. Polimeni, David C. Van Essen, and Mark Jenkinson. The minimal preprocessing pipelines for the human connectome project. *NeuroImage*, 80:105–124, 2013.

[63] Gary H Glover, Tie-Qiang Li, and David Ress. Image-based method for retrospective correction of physiological motion effects in fmri: Retroicor. *Magnetic Resonance in Medicine: An Official Journal of the International Society for Magnetic Resonance in Medicine*, 44(1):162–167, 2000.

[64] Alexandra Golby, Gerald Silverberg, Elizabeth Race, Susan Gabrieli, James O'Shea, Kyle Knierim, Glenn Stebbins, and John Gabrieli. Memory encoding in alzheimer's disease: an fmri study of explicit and implicit memory. *Brain*, 128(4):773–787, 2005.

[65] K. Gorgolewski, C. D. Burns, C. Madison, D. Clark, Y. O. Halchenko, M. L. Waskom, and S. Ghosh. Nipype: a flexible, lightweight and extensible neuroimaging data processing framework in python. *Frontiers in Neuroinformatics*, 5:13, 2011.

[66] Krzysztof J. Gorgolewski, Oscar Esteban, Christopher J. Markiewicz, Erik Ziegler, David Gage Ellis, Michael Philipp Notter, Dorota Jarecka, Hans Johnson, Christopher Burns, Alexandre Manhães-Savio, Carlo Hamalainen, Benjamin Yvernault, Taylor Salo, Kesshi Jordan, Mathias Goncalves, Michael Waskom, Daniel Clark, Jason Wong, Fred Loney, Marc Modat, Blake E Dewey, Cindee Madison, Matteo Visconti di Oleggio Castello, Michael G. Clark, Michael Dayan, Dav Clark, Anisha Keshavan, Basile Pinsard, Alexandre Gramfort, Shoshana Berleant, Dylan M. Nielson, Salma Bougacha, Gael Varoquaux, Ben Cipollini, Ross Markello, Ariel Rokem, Brendan Moloney, Yaroslav O.

Halchenko, Demian Wassermann, Michael Hanke, Christian Horea, Jakub Kaczmarzyk, Gilles de Hollander, Elizabeth DuPre, Ashley Gillman, David Mordom, Colin Buchanan, Rosalia Tungaraza, Wolfgang M. Pauli, Shariq Iqbal, Sharad Sikka, Matteo Mancini, Yannick Schwartz, Ian B. Malone, Mathieu Dubois, Caroline Frohlich, David Welch, Jessica Forbes, James Kent, Aimi Watanabe, Chad Cumba, Julia M. Huntenburg, Erik Kastman, B. Nolan Nichols, Arman Eshaghi, Daniel Ginsburg, Alexander Schaefer, Benjamin Acland, Steven Giavasis, Jens Kleesiek, Drew Erickson, René Küttner, Christian Haselgrove, Carlos Correa, Ali Ghayoor, Franz Liem, Jarrod Millman, Daniel Haehn, Jeff Lai, Dale Zhou, Ross Blair, Tristan Glatard, Mandy Renfro, Siqi Liu, Ari E. Kahn, Fernando Pérez-García, William Triplett, Leonie Lampe, Jörg Stadler, Xiang-Zhen Kong, Michael Hallquist, Andrey Chetverikov, John Salvatore, Anne Park, Russell Poldrack, R. Cameron Craddock, Souheil Inati, Oliver Hinds, Gavin Cooper, L. Nathan Perkins, Ana Marina, Aaron Mattfeld, Maxime Noel, Lukas Snoek, K Matsubara, Brian Cheung, Simon Rothmei, Sebastian Urchs, Joke Durnez, Fred Mertz, Daniel Geisler, Andrew Floren, Stephan Gerhard, Paul Sharp, Miguel Molina-Romero, Alejandro Weinstein, William Broderick, Victor Saase, Sami Kristian Andberg, Robbert Harms, Kai Schlamp, Jaime Arias, Dimitri Papadopoulos Orfanos, Claire Tarbert, Arielle Tambini, Alejandro De La Vega, Thomas Nickson, Matthew Brett, Marcel Falkiewicz, Kornelius Podranski, Janosch Linkersdörfer, Guillaume Flandin, Eduard Ort, Dmitry Shachnev, Daniel McNamee, Andrew Davison, Jan Varada, Isaac Schwabacher, John Pellman, Martin Perez-Guevara, Ranjeet Khanuja, Nicolas Pannetier, Conor McDermottroe, and Satrajit Ghosh. Nipype. *Software*, 2018.

[67] Cheryl L Grady, Anthony R McIntosh, Sania Beig, Michelle L Keightley, Hana Burian, and Sandra E Black. Evidence from functional neuroimaging of a compensatory prefrontal network in alzheimer's disease. *Journal of Neuroscience*, 23(3):986–993, 2003.

[68] Abigail S Greene, Siyuan Gao, Dustin Scheinost, and R Todd Constable. Task-induced brain state manipulation improves prediction of individual traits. *Nature communications*, 9(1):1–13, 2018.

[69] Abigail S Greene, Xilin Shen, Stephanie Noble, Corey Horien, C Alice Hahn, Jagriti Arora, Fuyuze Tokoglu, Marisa N Spann, Carmen I Carrión, Daniel S Barron, et al. Brain–phenotype models fail for individuals who defy sample stereotypes. *Nature*, pages 1–10, 2022.

[70] Michael D Greicius, Ben Krasnow, Allan L Reiss, and Vinod Menon. Functional connectivity in the resting brain: a network analysis of the default mode hypothesis. *Proceedings of the National Academy of Sciences*, 100(1):253–258, 2003.

[71] Michael D Greicius, Gaurav Srivastava, Allan L Reiss, and Vinod Menon. Default-mode network activity distinguishes alzheimer's disease from healthy

aging: evidence from functional mri. *Proceedings of the National Academy of Sciences*, 101(13):4637–4642, 2004.

[72] Douglas N Greve and Bruce Fischl. Accurate and robust brain image alignment using boundary-based registration. *NeuroImage*, 48(1):63–72, 2009.

[73] Michelle Hampson, Bradley S Peterson, Pawel Skudlarski, James C Gatenby, and John C Gore. Detection of functional connectivity using temporal correlations in mr images. *Human brain mapping*, 15(4):247–262, 2002.

[74] Benjamin M Hampstead, Krishnankutty Sathian, Marom Bikson, and Anthony Y Stringer. Combined mnemonic strategy training and high-definition transcranial direct current stimulation for memory deficits in mild cognitive impairment. *Alzheimer's & Dementia: Translational Research & Clinical Interventions*, 3(3):459–470, 2017.

[75] Benjamin M Hampstead, Anthony Y Stringer, Randall F Stilla, Akshay Amaraneni, and K Sathian. Where did i put that? patients with amnestic mild cognitive impairment demonstrate widespread reductions in activity during the encoding of ecologically relevant object-location associations. *Neuropsychologia*, 49(9):2349–2361, 2011.

[76] Benjamin M Hampstead, Anthony Y Stringer, Randall F Stilla, Gopikrishna Deshpande, Xiaoping Hu, Anna Bacon Moore, and K Sathian. Activation and effective connectivity changes following explicit-memory training for face–name pairs in patients with mild cognitive impairment: a pilot study. *Neurorehabilitation and neural repair*, 25(3):210–222, 2011.

[77] Kuan Han, Haiguang Wen, Junxing Shi, Kun-Han Lu, Yizhen Zhang, Di Fu, and Zhongming Liu. Variational autoencoder: An unsupervised model for encoding and decoding fmri activity in visual cortex. *NeuroImage*, 198:125–136, 2019.

[78] Haruo Hanyu, Tetsuichi Asano, Hirofumi Sakurai, Yukari Imon, Toshihiko Iwamoto, Masaru Takasaki, Hiroaki Shindo, and Kimihiko Abe. Diffusion-weighted and magnetization transfer imaging of the corpus callosum in alzheimer's disease. *Journal of the neurological sciences*, 167(1):37–44, 1999.

[79] Haruo Hanyu, Hirofumi Sakurai, Toshihiko Iwamoto, Masaru Takasaki, Hiroaki Shindo, and Kimihiko Abe. Diffusion-weighted mr imaging of the hippocampus and temporal white matter in alzheimer's disease. *Journal of the neurological sciences*, 156(2):195–200, 1998.

[80] John Harrison, Dorene M Rentz, Trent McLaughlin, Timothy Niecko, Keith M Gregg, Ronald S Black, Jacqui Buchanan, Enchi Liu, Michael Grundman, and ELN-AIP-901 Study Investigator Group. Cognition in mci and alzheimer's disease: baseline data from a longitudinal study of the ntb. *The Clinical Neuropsychologist*, 28(2):252–268, 2014.

[81] Yong He, Liang Wang, Yufeng Zang, Lixia Tian, Xinqing Zhang, Kuncheng Li, and Tianzi Jiang. Regional coherence changes in the early stages of alzheimer's disease: a combined structural and resting-state functional mri study. *Neuroimage*, 35(2):488–500, 2007.

[82] Reinhard Heun, Katrin Freymann, Michael Erb, Dirk T Leube, Frank Jessen, Tilo T Kircher, and Wolfgang Grodd. Mild cognitive impairment (mci) and actual retrieval performance affect cerebral activation in the elderly. *Neurobiology of Aging*, 28(3):404–413, 2007.

[83] Irina Higgins, Loic Matthey, Arka Pal, Christopher Burgess, Xavier Glorot, Matthew Botvinick, Shakir Mohamed, and Alexander Lerchner. beta-vae: Learning basic visual concepts with a constrained variational framework. 2016.

[84] John R Hodges and Karalyn Patterson. Is semantic memory consistently impaired early in the course of alzheimer's disease? neuroanatomical and diagnostic implications. *Neuropsychologia*, 33(4):441–459, 1995.

[85] Milos D Ikonomovic, William E Klunk, Eric E Abrahamson, Chester A Mathis, Julie C Price, Nicholas D Tsopelas, Brian J Lopresti, Scott Ziolko, Wenzhu Bi, William R Paljug, et al. Post-mortem correlates of in vivo pib-pet amyloid imaging in a typical case of alzheimer's disease. *Brain*, 131(6):1630–1645, 2008.

[86] Alexandru D Iordan, Katherine A Cooke, Kyle D Moored, Benjamin Katz, Martin Buschkuehl, Susanne M Jaeggi, John Jonides, Scott J Peltier, Thad A Polk, and Patricia A Reuter-Lorenz. Aging and network properties: Stability over time and links with learning during working memory training. *Frontiers in aging neuroscience*, 9:419, 2018.

[87] Iva Ivanova, David P Salmon, and Tamar H Gollan. The multilingual naming test in alzheimer's disease: clues to the origin of naming impairments. *Journal of the International neuropsychological Society*, 19(3):272–283, 2013.

[88] Clifford R Jack, David A Bennett, Kaj Blennow, Maria C Carrillo, Howard H Feldman, Giovanni B Frisoni, Harald Hampel, William J Jagust, Keith A Johnson, David S Knopman, et al. A/t/n: an unbiased descriptive classification scheme for alzheimer disease biomarkers. *Neurology*, 87(5):539–547, 2016.

[89] Clifford R Jack Jr, David A Bennett, Kaj Blennow, Maria C Carrillo, Billy Dunn, Samantha Budd Haeberlein, David M Holtzman, William Jagust, Frank Jessen, Jason Karlawish, et al. Nia-aa research framework: toward a biological definition of alzheimer's disease. *Alzheimer's & Dementia*, 14(4):535–562, 2018.

[90] Clifford R Jack Jr, David S Knopman, Stephen D Weigand, Heather J Wiste, Prashanthi Vemuri, Val Lowe, Kejal Kantarci, Jeffrey L Gunter, Matthew L Senjem, Robert J Ivnik, et al. An operational approach to national institute on aging–alzheimer's association criteria for preclinical alzheimer disease. *Annals of neurology*, 71(6):765–775, 2012.

[91] Mark Jenkinson, Peter Bannister, Michael Brady, and Stephen Smith. Improved optimization for the robust and accurate linear registration and motion correction of brain images. *Neuroimage*, 17(2):825–841, 2002.

[92] Mark Jenkinson, Peter Bannister, Michael Brady, and Stephen Smith. Improved optimization for the robust and accurate linear registration and motion correction of brain images. *NeuroImage*, 17(2):825–841, 2002.

[93] Rongtao Jiang, Nianming Zuo, Judith M Ford, Shile Qi, Dongmei Zhi, Chuanjun Zhuo, Yong Xu, Zening Fu, Juan Bustillo, Jessica A Turner, et al. Task-induced brain connectivity promotes the detection of individual differences in brain-behavior relationships. *NeuroImage*, 207:116370, 2020.

[94] Julene K Johnson, Alden L Gross, Judy Pa, Donald G McLaren, Lovingly Quitania Park, and Jennifer J Manly. Longitudinal change in neuropsychological performance using latent growth models: a study of mild cognitive impairment. *Brain imaging and behavior*, 6(4):540–550, 2012.

[95] Nathan A Johnson, Geon-Ho Jahng, Michael W Weiner, Bruce L Miller, Helena C Chui, William J Jagust, Maria L Gorno-Tempini, and Norbert Schuff. Pattern of cerebral hypoperfusion in alzheimer's disease and mild cognitive impairment measured with arterial spin-labeling mr imaging: Initial experience. In *International Congress Series*, volume 1290, pages 108–122. Elsevier, 2006.

[96] Petro Julkunen, Anne M Jauhiainen, Susanna Westerén-Punnonen, Eriikka Pirinen, Hilkka Soininen, Mervi Könönen, Ari Pääkkönen, Sara Määttä, and Jari Karhu. Navigated tms combined with eeg in mild cognitive impairment and alzheimer's disease: a pilot study. *Journal of Neuroscience Methods*, 172(2):270–276, 2008.

[97] Daniel P Kennedy, Elizabeth Redcay, and Eric Courchesne. Failing to deactivate: resting functional abnormalities in autism. *Proceedings of the National Academy of Sciences*, 103(21):8275–8280, 2006.

[98] Ali Khazaee, Ata Ebrahimzadeh, Abbas Babajani-Feremi, Alzheimer's Disease Neuroimaging Initiative, et al. Classification of patients with mci and ad from healthy controls using directed graph measures of resting-state fmri. *Behavioural brain research*, 322:339–350, 2017.

[99] Jung-Hoon Kim. *Representation Learning of fMRI Data using Variational Autoencoder*. PhD thesis, Purdue University Graduate School, 2021.

[100] Jung-Hoon Kim, Josepheen De Asis-Cruz, Dhineshvikram Krishnamurthy, and Catherine Limperopoulos. Towards a more informative representation of the fetal-neonatal brain connectome using variational autoencoder. *bioRxiv*, 2022.

[101] Jung-Hoon Kim, Yizhen Zhang, Kuan Han, Zheyu Wen, Minkyu Choi, and Zhongming Liu. Representation learning of resting state fmri with variational autoencoder. *NeuroImage*, 241:118423, 2021.

[102] Diederik P Kingma and Jimmy Ba. Adam: A method for stochastic optimization. *arXiv preprint arXiv:1412.6980*, 2014.

[103] Diederik P Kingma and Max Welling. Auto-encoding variational bayes. *arXiv preprint arXiv:1312.6114*, 2013.

[104] Arno Klein, Satrajit S. Ghosh, Forrest S. Bao, Joachim Giard, Yrjö Häme, Eliezer Stavsky, Noah Lee, Brian Rossa, Martin Reuter, Elias Chaibub Neto, and Anisha Keshavan. Mindboggling morphometry of human brains. *PLOS Computational Biology*, 13(2):e1005350, 2017.

[105] Daiji Kogure, Hiroshi Matsuda, Takashi Ohnishi, Takashi Asada, Masatake Uno, Toshiyuki Kunihiro, Seigo Nakano, and Masaru Takasaki. Longitudinal evaluation of early alzheimer's disease using brain perfusion spect. *Journal of nuclear medicine*, 41(7):1155–1162, 2000.

[106] Hans Martin Kolbinger, Gereon Höflich, Andreas Hufnagel, Hans-Jürgen Müller, and Siegfried Kasper. Transcranial magnetic stimulation (tms) in the treatment of major depression—a pilot study. *Human Psychopharmacology: Clinical and Experimental*, 10(4):305–310, 1995.

[107] Anjali Krishnan, Lynne J Williams, Anthony Randal McIntosh, and Hervé Abdi. Partial least squares (pls) methods for neuroimaging: a tutorial and review. *Neuroimage*, 56(2):455–475, 2011.

[108] Evelyn MR Lake, Emily S Finn, Stephanie M Noble, Tamara Vanderwal, Xilin Shen, Monica D Rosenberg, Marisa N Spann, Marvin M Chun, Dustin Scheinost, and R Todd Constable. The functional brain organization of an individual allows prediction of measures of social abilities transdiagnostically in autism and attention-deficit/hyperactivity disorder. *Biological psychiatry*, 86(4):315–326, 2019.

[109] Jean-Charles Lambert, Simon Heath, Gael Even, Dominique Campion, Kristel Sleegers, Mikko Hiltunen, Onofre Combarros, Diana Zelenika, Maria J Bullido, Béatrice Tavernier, et al. Genome-wide association study identifies variants at clu and cr1 associated with alzheimer's disease. *Nature genetics*, 41(10):1094–1099, 2009.

[110] Jack L Lancaster, Marty G Woldorff, Lawrence M Parsons, Mario Liotti, Catarina S Freitas, Lacy Rainey, Peter V Kochunov, Dan Nickerson, Shawn A Mikiten, and Peter T Fox. Automated talairach atlas labels for functional brain mapping. *Human brain mapping*, 10(3):120–131, 2000.

[111] C. Lanczos. Evaluation of noisy data. *Journal of the Society for Industrial and Applied Mathematics Series B Numerical Analysis*, 1(1):76–85, 1964.

[112] RA Lanius, RL Bluhm, NJ Coupland, KM Hegadoren, B Rowe, J Theberge, RWJ Neufeld, PC Williamson, and M Brimson. Default mode network connectivity as a predictor of post-traumatic stress disorder symptom severity in acutely traumatized subjects. *Acta Psychiatrica Scandinavica*, 121(1):33–40, 2010.

[113] Catherine Lebel, Myrlene Gee, Richard Camicioli, Marguerite Wieler, Wayne Martin, and Christian Beaulieu. Diffusion tensor imaging of white matter tract evolution over the lifespan. *Neuroimage*, 60(1):340–352, 2012.

[114] Anna E Leeuwis, Marije R Benedictus, Joost PA Kuijer, Maja AA Binnewijzend, Astrid M Hooghiemstra, Sander CJ Verfaillie, Teddy Koene, Philip Scheltens, Frederik Barkhof, Niels D Prins, et al. Lower cerebral blood flow is associated with impairment in multiple cognitive domains in alzheimer's disease. *Alzheimer's & Dementia*, 13(5):531–540, 2017.

[115] Manja Lehmann, Jonathan D Rohrer, Matthew J Clarkson, Gerard R Ridgway, Rachael I Scahill, Marc Modat, Jason D Warren, Sebastien Ourselin, Josephine Barnes, Martin N Rossor, et al. Reduced cortical thickness in the posterior cingulate gyrus is characteristic of both typical and atypical alzheimer's disease. *Journal of Alzheimer's Disease*, 20(2):587–598, 2010.

[116] Runzhi Li, Yanling Zhang, Zhizheng Zhuo, Yanli Wang, Ziyan Jia, Mengfan Sun, Yuan Zhang, Wenyi Li, Yunyun Duan, Zeshan Yao, et al. Altered cerebral blood flow in alzheimer's disease with depression. *Frontiers in psychiatry*, 12, 2021.

[117] Mesrob Lilia, Sarazin Marie, Hahn-Barma Valerie, Dubois Bruno, Gallinari Patrick, Kinkingnéhun Serge, et al. Dti and structural mri classification in alzheimer's disease. *Advances in molecular imaging*, 2012, 2012.

[118] Seung-Hyun Lim, Jiyoon Lee, Sumin Jung, Bokyung Kim, Hak Young Rhee, Se-Hong Oh, Soonchan Park, Ah Rang Cho, Chang-Woo Ryu, and Geon-Ho Jahng. Myelin-weighted imaging presents reduced apparent myelin water in patients with alzheimer's disease. *Diagnostics*, 12(2):446, 2022.

[119] Qi Lin, Monica D Rosenberg, Kwangsun Yoo, Tiffany W Hsu, Thomas P O'Connell, and Marvin M Chun. Resting-state functional connectivity predicts cognitive impairment related to alzheimer's disease. *Frontiers in aging neuroscience*, 10:94, 2018.

[120] Shih-Yen Lin, Chen-Pei Lin, Tsung-Jen Hsieh, Chung-Fen Lin, Sih-Huei Chen, Yi-Ping Chao, Yong-Sheng Chen, Chih-Cheng Hsu, and Li-Wei Kuo. Multiparametric graph theoretical analysis reveals altered structural and functional network topology in alzheimer's disease. *NeuroImage: Clinical*, 22:101680, 2019.

[121] Ranjan Maitra. A re-defined and generalized percent-overlap-of-activation measure for studies of fmri reproducibility and its use in identifying outlier activation maps. *Neuroimage*, 50(1):124–135, 2010.

[122] Joseph A Maldjian, Paul J Laurienti, Robert A Kraft, and Jonathan H Burdette. An automated method for neuroanatomic and cytoarchitectonic atlas-based interrogation of fmri data sets. *Neuroimage*, 19(3):1233–1239, 2003.

[123] Tahir Mehmood, Kristian Hovde Liland, Lars Snipen, and Solve Sæbø. A review of variable selection methods in partial least squares regression. *Chemometrics and intelligent laboratory systems*, 118:62–69, 2012.

[124] Djalel-Eddine Meskaldji, Maria Giulia Preti, Thomas AW Bolton, Marie-Louise Montandon, Cristelle Rodriguez, Stephan Morgenthaler, Panteleimon Giannakopoulos, Sven Haller, and Dimitri Van De Ville. Prediction of long-term memory scores in mci based on resting-state fmri. *NeuroImage: Clinical*, 12:785–795, 2016.

[125] Saul L Miller, Kim Celone, Kristina DePeau, Eli Diamond, Bradford C Dickerson, Dorene Rentz, Maija Pihlajamäki, and Reisa A Sperling. Age-related memory impairment associated with loss of parietal deactivation but preserved hippocampal activation. *Proceedings of the National Academy of Sciences*, 105(6):2181–2186, 2008.

[126] mkarker. mkarker/great-lakes-fmriprep: v1.0.1, September 2022.

[127] Lisa Mosconi, Rachel Mistur, Remigiusz Switalski, Wai Hon Tsui, Lidia Glodzik, Yi Li, Elizabeth Pirraglia, Susan De Santi, Barry Reisberg, Thomas Wisniewski, et al. Fdg-pet changes in brain glucose metabolism from normal cognition to pathologically verified alzheimer's disease. *European journal of nuclear medicine and molecular imaging*, 36(5):811–822, 2009.

[128] Lisa Mosconi, Alberto Pupi, and Mony J De Leon. Brain glucose hypometabolism and oxidative stress in preclinical alzheimer's disease. *Annals of the New York Academy of Sciences*, 1147(1):180–195, 2008.

[129] Henk JMM Mutsaerts, Jan Petr, Paul Groot, Pieter Vandemaele, Silvia Ingala, Andrew D Robertson, Lena Václavů, Inge Groote, Hugo Kuijf, Fernando Zelaya, et al. Exploreasl: an image processing pipeline for multi-center asl perfusion mri studies. *Neuroimage*, 219:117031, 2020.

[130] Ziad S Nasreddine, Natalie A Phillips, Valérie Bédirian, Simon Charbonneau, Victor Whitehead, Isabelle Collin, Jeffrey L Cummings, and Howard Chertkow. The montreal cognitive assessment, moca: a brief screening tool for mild cognitive impairment. *Journal of the American Geriatrics Society*, 53(4):695–699, 2005.

[131] Robert D Nebes. Semantic memory in alzheimer's disease. *Psychological bulletin*, 106(3):377, 1989.

[132] Hideyuki Okano, Tomoo Hirano, and Evan Balaban. Learning and memory. *Proceedings of the National Academy of Sciences*, 97(23):12403–12404, 2000.

[133] Pernille J Olesen, Helena Westerberg, and Torkel Klingberg. Increased prefrontal and parietal activity after training of working memory. *Nature neuroscience*, 7(1):75–79, 2004.

[134] Scott J Peltier and Yash Shah. Biophysical modulations of functional connectivity. *Brain connectivity*, 1(4):267–277, 2011.

[135] Judes Poirier, P Bertrand, S Kogan, S Gauthier, J Davignon, and D Bouthillier. Apolipoprotein e polymorphism and alzheimer's disease. *The Lancet*, 342(8873):697–699, 1993.

[136] Katherine L Possin, Victor R Laluz, Oscar Z Alcantar, Bruce L Miller, and Joel H Kramer. Distinct neuroanatomical substrates and cognitive mechanisms of figure copy performance in alzheimer's disease and behavioral variant frontotemporal dementia. *Neuropsychologia*, 49(1):43–48, 2011.

[137] Jonathan D Power, Alexander L Cohen, Steven M Nelson, Gagan S Wig, Kelly Anne Barnes, Jessica A Church, Alecia C Vogel, Timothy O Laumann, Fran M Miezin, Bradley L Schlaggar, et al. Functional network organization of the human brain. *Neuron*, 72(4):665–678, 2011.

[138] Jonathan D. Power, Anish Mitra, Timothy O. Laumann, Abraham Z. Snyder, Bradley L. Schlaggar, and Steven E. Petersen. Methods to detect, characterize, and remove motion artifact in resting state fmri. *NeuroImage*, 84(Supplement C):320–341, 2014.

[139] Zhigang Qi, Xia Wu, Zhiqun Wang, Nang Zhang, Huiqing Dong, Li Yao, and Kuncheng Li. Impairment and compensation coexist in amnestic mci default mode network. *Neuroimage*, 50(1):48–55, 2010.

[140] Jose M Rabey, Evgenia Dobronevsky, Sergio Aichenbaum, Ofer Gonen, Revital Gendelman Marton, and Michael Khaigrekht. Repetitive transcranial magnetic stimulation combined with cognitive training is a safe and effective modality for the treatment of alzheimer's disease: a randomized, double-blind study. *Journal of Neural Transmission*, 120(5):813–819, 2013.

[141] Gil D Rabinovici, Maria C Carrillo, Mark Forman, Susan DeSanti, David S Miller, Nicholas Kozauer, Ronald C Petersen, Christopher Randolph, David S Knopman, Eric E Smith, et al. Multiple comorbid neuropathologies in the setting of alzheimer's disease neuropathology and implications for drug development. *Alzheimer's & Dementia: Translational Research & Clinical Interventions*, 3(1):83–91, 2017.

[142] Marcus E Raichle, Ann Mary MacLeod, Abraham Z Snyder, William J Powers, Debra A Gusnard, and Gordon L Shulman. A default mode of brain function. *Proceedings of the National Academy of Sciences*, 98(2):676–682, 2001.

[143] Kumar B Rajan, Jennifer Weuve, Lisa L Barnes, Elizabeth A McAninch, Robert S Wilson, and Denis A Evans. Population estimate of people with clinical alzheimer's disease and mild cognitive impairment in the united states (2020–2060). *Alzheimer's & Dementia*, 17(12):1966–1975, 2021.

[144] Pasko Rakic. Evolution of the neocortex: a perspective from developmental biology. *Nature Reviews Neuroscience*, 10(10):724–735, 2009.

[145] Christopher Randolph, Michael C Tierney, Erich Mohr, and Thomas N Chase. The repeatable battery for the assessment of neuropsychological status (rbans): preliminary clinical validity. *Journal of clinical and experimental neuropsychology*, 20(3):310–319, 1998.

[146] Javier Rasero, Amy Isabella Sentis, Fang-Cheng Yeh, and Timothy Verstynen. Integrating across neuroimaging modalities boosts prediction accuracy of cognitive ability. *PLoS computational biology*, 17(3):e1008347, 2021.

[147] Guido Rodriguez, Paolo Vitali, Piero Calvini, Chiara Bordoni, Nicola Girtler, Gioconda Taddei, Giuliano Mariani, and Flavio Nobili. Hippocampal perfusion in mild alzheimer's disease. *Psychiatry Research: Neuroimaging*, 100(2):65–74, 2000.

[148] Serge ARB Rombouts, Frederik Barkhof, Rutger Goekoop, Cornelis J Stam, and Philip Scheltens. Altered resting state networks in mild cognitive impairment and mild alzheimer's disease: an fmri study. *Human brain mapping*, 26(4):231–239, 2005.

[149] Caterina Rosano, Howard J Aizenstein, Jennifer L Cochran, Judith A Saxton, Steven T De Kosky, Anne B Newman, Lewis H Kuller, Oscar L Lopez, and Cameron S Carter. Event-related functional magnetic resonance imaging investigation of executive control in very old individuals with mild cognitive impairment. *Biological psychiatry*, 57(7):761–767, 2005.

[150] Stephen E Rose, Fang Chen, Jonathan B Chalk, Fernando O Zelaya, Wendy E Strugnell, Mark Benson, James Semple, and David M Doddrell. Loss of connectivity in alzheimer's disease: an evaluation of white matter tract integrity with colour coded mr diffusion tensor imaging. *Journal of Neurology, Neurosurgery & Psychiatry*, 69(4):528–530, 2000.

[151] Monica D Rosenberg, Emily S Finn, Dustin Scheinost, Xenophon Papademetris, Xilin Shen, R Todd Constable, and Marvin M Chun. A neuromarker of sustained attention from whole-brain functional connectivity. *Nature neuroscience*, 19(1):165–171, 2016.

[152] Mikail Rubinov and Olaf Sporns. Complex network measures of brain connectivity: uses and interpretations. *Neuroimage*, 52(3):1059–1069, 2010.

[153] RM Ruff, RH Light, SB Parker, and HS Levin. Benton controlled oral word association test: reliability and updated norms. *Archives of clinical neuropsychology*, 11(4):329–338, 1996.

[154] Theodore D. Satterthwaite, Mark A. Elliott, Raphael T. Gerraty, Kosha Ruparel, James Loughead, Monica E. Calkins, Simon B. Eickhoff, Hakon Hakonarson, Ruben C. Gur, Raquel E. Gur, and Daniel H. Wolf. An improved framework for confound regression and filtering for control of motion artifact in the preprocessing of resting-state functional connectivity data. *NeuroImage*, 64(1):240–256, 2013.

[155] Andrea Scalabrini, Benedetta Vai, Sara Poletti, Stefano Damiani, Clara Mucci, Cristina Colombo, Raffaella Zanardi, Francesco Benedetti, and Georg Northoff. All roads lead to the default-mode network—global source of dmn abnormalities in major depressive disorder. *Neuropsychopharmacology*, 45(12):2058–2069, 2020.

[156] Stephen W Scheff, Douglas A Price, Mubeen A Ansari, Kelly N Roberts, Frederick A Schmitt, Milos D Ikonomovic, and Elliott J Mufson. Synaptic change in the posterior cingulate gyrus in the progression of alzheimer's disease. *Journal of Alzheimer's Disease*, 43(3):1073–1090, 2015.

[157] Paul Schmidt and Lucie Wink. Lst: A lesion segmentation tool for spm. *Manual/Documentation for version*, 2:15, 2017.

[158] Sudha Seshadri, Annette L Fitzpatrick, M Arfan Ikram, Anita L DeStefano, Vilmundur Gudnason, Merce Boada, Joshua C Bis, Albert V Smith, Minerva M Carrasquillo, Jean Charles Lambert, et al. Genome-wide analysis of genetic loci associated with alzheimer disease. *Jama*, 303(18):1832–1840, 2010.

[159] Xilin Shen, Emily S Finn, Dustin Scheinost, Monica D Rosenberg, Marvin M Chun, Xenophon Papademetris, and R Todd Constable. Using connectome-based predictive modeling to predict individual behavior from brain connectivity. *nature protocols*, 12(3):506–518, 2017.

[160] Reisa A Sperling, Paul S Aisen, Laurel A Beckett, David A Bennett, Suzanne Craft, Anne M Fagan, Takeshi Iwatsubo, Clifford R Jack Jr, Jeffrey Kaye, Thomas J Montine, et al. Toward defining the preclinical stages of alzheimer's disease: Recommendations from the national institute on aging-alzheimer's association workgroups on diagnostic guidelines for alzheimer's disease. *Alzheimer's & dementia*, 7(3):280–292, 2011.

[161] Reisa A Sperling, JF Bates, EF Chua, AJ Cocchiarella, DM Rentz, BR Rosen, DL Schacter, and MS1738201 Albert. fmri studies of associative encoding in

young and elderly controls and mild alzheimer's disease. *Journal of Neurology, Neurosurgery & Psychiatry*, 74(1):44–50, 2003.

[162] Chandra Sripada, Mike Angstadt, Saige Rutherford, Daniel Kessler, Yura Kim, Mike Yee, and Elizaveta Levina. Basic units of inter-individual variation in resting state connectomes. *Scientific reports*, 9(1):1–12, 2019.

[163] Chandra Sripada, Saige Rutherford, Mike Angstadt, Wesley K Thompson, Monica Luciana, Alexander Weigard, Luke H Hyde, and Mary Heitzeg. Prediction of neurocognition in youth from resting state fmri. *Molecular psychiatry*, 25(12):3413–3421, 2020.

[164] Kayla R Suhrie, Dustin B Hammers, Sariah M Porter, Ava M Dixon, Jace B King, Jeffrey S Anderson, Kevin Duff, and John M Hoffman. Predicting biomarkers in intact older adults and those with amnestic mild cognitive impairment, and mild alzheimer's disease using the repeatable battery for the assessment of neuropsychological status. *Journal of Clinical and Experimental Neuropsychology*, 43(9):861–878, 2021.

[165] Manuela Tondelli, Gordon K Wilcock, Paolo Nichelli, Celeste A De Jager, Mark Jenkinson, and Giovanna Zamboni. Structural mri changes detectable up to ten years before clinical alzheimer's disease. *Neurobiology of aging*, 33(4):825–e25, 2012.

[166] N. J. Tustison, B. B. Avants, P. A. Cook, Y. Zheng, A. Egan, P. A. Yushkevich, and J. C. Gee. N4itk: Improved n3 bias correction. *IEEE Transactions on Medical Imaging*, 29(6):1310–1320, 2010.

[167] Nathalie Tzourio-Mazoyer, Brigitte Landeau, Dimitri Papathanassiou, Fabrice Crivello, Octave Etard, Nicolas Delcroix, Bernard Mazoyer, and Marc Joliot. Automated anatomical labeling of activations in spm using a macroscopic anatomical parcellation of the mni mri single-subject brain. *Neuroimage*, 15(1):273–289, 2002.

[168] David C Van Essen, Stephen M Smith, Deanna M Barch, Timothy EJ Behrens, Essa Yacoub, Kamil Ugurbil, Wu-Minn HCP Consortium, et al. The wu-minn human connectome project: an overview. *Neuroimage*, 80:62–79, 2013.

[169] Prashanthi Vemuri and Clifford R Jack. Role of structural mri in alzheimer's disease. *Alzheimer's research & therapy*, 2(4):1–10, 2010.

[170] Sander CJ Verfaillie, Sofie M Adriaanse, Maja AA Binnewijzend, Marije R Benedictus, Rik Ossenkoppele, Mike P Wattjes, Yolande AL Pijnenburg, Wiesje M van der Flier, Adriaan A Lammertsma, Joost Kuijer, et al. Cerebral perfusion and glucose metabolism in alzheimer's disease and frontotemporal dementia: two sides of the same coin? *European radiology*, 25(10):3050–3059, 2015.

[171] PJ Visser, FRJ Verhey, PAM Hofman, P Scheltens, and J Jolles. Medial temporal lobe atrophy predicts alzheimer's disease in patients with minor cognitive impairment. *Journal of Neurology, Neurosurgery & Psychiatry*, 72(4):491–497, 2002.

[172] Nicholas M Vogt, Jack F Hunt, Nagesh Adluru, Douglas C Dean III, Sterling C Johnson, Sanjay Asthana, John-Paul J Yu, Andrew L Alexander, and Barbara B Bendlin. Cortical microstructural alterations in mild cognitive impairment and alzheimer's disease dementia. *Cerebral cortex*, 30(5):2948–2960, 2020.

[173] Kun Wang, Meng Liang, Liang Wang, Lixia Tian, Xinqing Zhang, Kuncheng Li, and Tianzi Jiang. Altered functional connectivity in early alzheimer's disease: A resting-state fmri study. *Human brain mapping*, 28(10):967–978, 2007.

[174] Ze Wang, Sandhitsu R Das, Sharon X Xie, Steven E Arnold, John A Detre, David A Wolk, Alzheimer's Disease Neuroimaging Initiative, et al. Arterial spin labeled mri in prodromal alzheimer's disease: a multi-site study. *NeuroImage: Clinical*, 2:630–636, 2013.

[175] Zhiqun Wang, Peipeng Liang, Xiuqin Jia, Zhigang Qi, Lei Yu, Yanhui Yang, Weidong Zhou, Jie Lu, and Kuncheng Li. Baseline and longitudinal patterns of hippocampal connectivity in mild cognitive impairment: evidence from resting state fmri. *Journal of the neurological sciences*, 309(1-2):79–85, 2011.

[176] Sang Wook Yoo, Cheol E Han, Joseph S Shin, Sang Won Seo, Duk L Na, Marcus Kaiser, Yong Jeong, and Joon-Kyung Seong. A network flow-based analysis of cognitive reserve in normal ageing and alzheimer's disease. *Scientific reports*, 5(1):1–14, 2015.

[177] Yunan Wu, Pierre Besson, Emanuel A Azcona, S Kathleen Bandt, Todd B Parrish, and Aggelos K Katsaggelos. Reconstruction of resting state fmri using lstm variational auto-encoder on subcortical surface to detect epilepsy. In *2022 IEEE 19th International Symposium on Biomedical Imaging (ISBI)*, pages 1–5. IEEE, 2022.

[178] Jinhu Xiong, Lawrence M Parsons, Jia-Hong Gao, and Peter T Fox. Interregional connectivity to primary motor cortex revealed using mri resting state images. *Human brain mapping*, 8(2-3):151–156, 1999.

[179] F Zerrin Yetkin, Roger N Rosenberg, Myron F Weiner, Phillip D Purdy, and C Munro Cullum. Fmri of working memory in patients with mild cognitive impairment and probable alzheimer's disease. *European radiology*, 16(1):193–206, 2006.

[180] Kwangsun Yoo, Monica D Rosenberg, Wei-Ting Hsu, Sheng Zhang, Chiang-Shan R Li, Dustin Scheinost, R Todd Constable, and Marvin M Chun.

Connectome-based predictive modeling of attention: Comparing different functional connectivity features and prediction methods across datasets. *Neuroimage*, 167:11–22, 2018.

[181] Daoqiang Zhang, Dinggang Shen, Alzheimer's Disease Neuroimaging Initiative, et al. Multi-modal multi-task learning for joint prediction of multiple regression and classification variables in alzheimer's disease. *NeuroImage*, 59(2):895–907, 2012.

[182] Daoqiang Zhang, Yaping Wang, Luping Zhou, Hong Yuan, Dinggang Shen, Alzheimer's Disease Neuroimaging Initiative, et al. Multimodal classification of alzheimer's disease and mild cognitive impairment. *Neuroimage*, 55(3):856–867, 2011.

[183] Han Zhang, Shuji Hao, Annie Lee, Simon B Eickhoff, Diliana Pecheva, Shirong Cai, Michael Meaney, Yap-Seng Chong, Birit FP Broekman, Marielle V Fortier, et al. Do intrinsic brain functional networks predict working memory from childhood to adulthood? *Human brain mapping*, 41(16):4574–4586, 2020.

[184] Y. Zhang, M. Brady, and S. Smith. Segmentation of brain MR images through a hidden markov random field model and the expectation-maximization algorithm. *IEEE Transactions on Medical Imaging*, 20(1):45–57, 2001.

[185] Weimin Zheng, Bin Cui, Ying Han, Haiqing Song, Kuncheng Li, Yong He, and Zhiqun Wang. Disrupted regional cerebral blood flow, functional activity and connectivity in alzheimer's disease: a combined asl perfusion and resting state fmri study. *Frontiers in Neuroscience*, 13:738, 2019.